
Electronic Thesis and Dissertation Repository

10-31-2017 11:00 AM

A Longitudinal Study of Tumour Metabolism Using Hyperpolarized Carbon-13 Magnetic Resonance Spectroscopic Imaging in a Preclinical Model of Glioma

Heeseung Lim, *The University of Western Ontario*

Supervisor: Timothy J. Scholl, *The University of Western Ontario*

A thesis submitted in partial fulfillment of the requirements for the Doctor of Philosophy degree in Medical Biophysics

© Heeseung Lim 2017

Follow this and additional works at: <https://ir.lib.uwo.ca/etd>



Part of the [Medical Biophysics Commons](#)

Recommended Citation

Lim, Heeseung, "A Longitudinal Study of Tumour Metabolism Using Hyperpolarized Carbon-13 Magnetic Resonance Spectroscopic Imaging in a Preclinical Model of Glioma" (2017). *Electronic Thesis and Dissertation Repository*. 5086.

<https://ir.lib.uwo.ca/etd/5086>

This Dissertation/Thesis is brought to you for free and open access by Scholarship@Western. It has been accepted for inclusion in Electronic Thesis and Dissertation Repository by an authorized administrator of Scholarship@Western. For more information, please contact wlsadmin@uwo.ca.

Abstract

Glioma is the most common and aggressive primary malignant brain tumour. Glioma is typically treated with surgery followed by radio/chemotherapy. Even with aggressive treatment, median survival time is expected to be ~12 to 15 months. Reoccurrence of glioma is almost inevitable, further threatening the well-being of patients who have already endured rigorous treatment. Therefore, it is paramount to choose the most effective therapy and to accurately determine outcome as early as possible to provide optimum end-of-life care. Tumours alter their metabolism in response to increasing energy demands, mainly through increased glycolysis and accompanying lactate production. This increases production of other acids and alters intracellular and extracellular pH. Hyperpolarized ^{13}C magnetic resonance spectroscopic imaging, is capable of measuring *in vivo* metabolism. Increased lactate production in tumours can be probed by imaging the metabolism of hyperpolarized [1- ^{13}C]pyruvate after injection. Similarly, extracellular pH can be mapped after measuring the concentrations of $\text{H}^{13}\text{CO}_3^-$ and $^{13}\text{CO}_2$ after injection of hyperpolarized ^{13}C bicarbonate. The objective of this thesis is to investigate molecular changes in lactate production and pH gradient in a rat glioma model. To accomplish this objective, three related projects have been undertaken. For first project, a custom-made switch-tunable radiofrequency coil was designed and constructed. This radiofrequency coil facilitated imaging ^1H and ^{13}C nuclei without any registration issues producing high signal-to-noise ratio imaging data. In the second project, C6 glioma was implanted into brains of rats, which were imaged with hyperpolarized [1- ^{13}C]pyruvate at days 7, 12, 15, 18, 21 and 24 after implantation. Between days 10 and 15, rats received one of three therapies: radiotherapy, chemotherapy, combined therapy or none. Significant early therapeutic response, measured as a reduction in the lactate-to-pyruvate ratio, was observed for effective therapy. In the final project, the same tumour model was used to study cellular pH gradient in tumours. Animals were monitored at days 8, 12 and 15 after implantation using hyperpolarized ^{13}C bicarbonate to measure intracellular pH and a chemical exchange saturation transfer method to measure intracellular pH. Measured pH gradient in tumours showed a higher intracellular pH than extracellular pH, which was the opposite of healthy brain tissue. These studies have demonstrated the potential of hyperpolarized ^{13}C probes to promptly measure changes in tumour metabolism.

Early response assessment is important for identifying effective therapies and eliminating the toxic effects of ineffective ones. This can potentially reduce treatment costs for expensive and ineffective therapies and improve the quality of life for patients.

Keywords

hyperpolarization, carbon-13, ^{13}C pyruvate, ^{13}C lactate, ^{13}C bicarbonate, RF coil design, switch-tuned RF coil, magnetic resonance spectroscopic imaging, molecular imaging, pH imaging, tumour metabolism, glioma, radiotherapy, chemotherapy, therapeutic response

Co-Authorship Statement

Chapter 2: “Construction and Evaluation of a Switch-Tuned ^{13}C - ^1H Birdcage Radiofrequency Coil for Imaging the Metabolism of Hyperpolarized ^{13}C -Enriched Compounds”, Heeseung Lim, Kundan Thind, Francisco M. Martinez-Santesteban, and Timothy J. Scholl (September 2013, Journal of Magnetic Resonance Imaging – DOI 10.1002/jmri.24458):

Heeseung Lim was responsible for construction of a switch-tuned ^{13}C - ^1H RF coil in addition to the experimental design, animal preparation and handling, data acquisition and analysis. Heeseung Lim performed experiments with assistance of Drs. Kundan Thind and Francisco M. Martinez-Santesteban. Dr. Timothy J. Scholl supervised the project. This work has been published in Journal of Magnetic Resonance Imaging.

Chapter 3: “Monitoring early changes in tumour metabolism in response to therapy using hyperpolarized ^{13}C MRSI in a preclinical model of glioma”, Heeseung Lim, Francisco Martinez-Santesteban, Michael D. Jensen, Albert Chen, Eugene Wong and Timothy J. Scholl (In resubmission at Scientific Reports)

Heeseung Lim was responsible for experimental design, animal handling and surgeries as well as data analysis. This includes development of custom MATLAB code for analysis of the ^{13}C MRSI data. Heeseung Lim performed the imaging experiments with the assistance of Dr. Francisco M. Martinez-Santesteban and Michael D. Jensen, and with advice of Dr. Albert Chen. Drs. Eugene Wong and Timothy J. Scholl supervised the project. This manuscript was authored by Heeseung Lim and edited by his co-authors. It has been resubmitted to Scientific Reports for further evaluation.

Chapter 4: “Longitudinal Measurement of Intra- and Extracellular pH in a Rat Model of Glioma”, Heeseung Lim, Mohammed Albatany, Francisco Martínez-Santesteban, Robert Bartha and Timothy J. Scholl (Manuscript prepared for submission to Tomography)

Heeseung Lim was responsible for experimental design, animal handling and surgeries. The imaging experiments and subsequent data analyses were performed by

Heeseung Lim and Mohammed Albatany with the assistance of Dr. Francisco M. Martinez-Santesteban. Drs. Robert Bartha and Timothy J. Scholl supervised the project. This manuscript was authored by Heeseung Lim and edited by his co-authors. This work is intended for submission to Tomography.

Acknowledgments

I would like to thank the sources of funding that supported these studies as well as the following people, who made this research possible.

First, I would like to thank my supervisor Dr. Timothy J. Scholl whom, over the years, has guided, supported and encouraged me to accomplish this body of research. I am very grateful for his mentorship.

I also would like to thank my advisory committee; Drs. Paula Foster, Charles McKenzie and David Palma, for their advice and mentorship throughout my thesis.

Dr. Francisco M. Martínez-Santesteban has helped me with almost all of these projects. Without his help, I could not have completed much of this research.

I would like to thank all my past and present laboratory mates; Yonathan Araya, Justin Peterson, Adam Le, Nolan Broeke, Nivin Nyström and Dr. Alireza Akbari. They have been great colleagues and I have enjoyed working alongside them.

Drs. Andrew Alejski, Kyle Gilbert, and Jian-xiong Wang have provided useful advice and discussion for various aspects of design of the RF hardware.

I also thank Dr. Trevor Wade for assistance with development of pulse sequences and his help to trouble shoot technical problems I encountered along the way with my MRI experiments.

I would also like to thank the laboratory of Dr. Paula Foster (specifically Drs. Yuanxin Chen, Amanda Hamilton and Yuanxin Chen) for providing the wet lab to do animal work and histology.

I appreciate the help of Brian Dalrymple and Frank Van Sas for fabricating the animal support bed and RF fixation hardware.

Dr. Albert Chen provided initial advice and consultation regarding hyperpolarized imaging of animal models.

I thank Jennifer Hadway, Dr. Lisa Hoffman and Dr. Timothy Yeung for help with initial training for our animal model, sharing of the tumour cell line and their animal protocol.

I would like to thank the laboratory of Dr. Robert Bartha for tumour pH research collaboration. In particular, I acknowledge the help of Mohammed Albatany (analyzing CEST data), Alex Li (acquisition of 9.4 T CEST data) and Miranda Bellyou (animal preparation and handling).

I appreciate the assistance of the laboratory of Prof. Steven Kerfoot (specifically Dr. Heather Craig) for help with microscopy.

Finally, we would also gratefully recognize funding from the Cancer Imaging Network of Ontario, the Ontario Institute for Cancer Research and the Natural Sciences and Engineering Research Council of Canada, without which, this research would not be possible.

Table of Contents

Abstract.....	i
Co-Authorship Statement.....	iii
Acknowledgments.....	v
Table of Contents.....	vii
List of Tables.....	xii
List of Figures.....	xiii
List of Appendices.....	xviii
List of Abbreviations.....	xix
Chapter 1.....	1
1 Introduction.....	1
1.1 Introduction to ^1H Magnetic Resonance Imaging.....	1
1.1.1 Nuclear spin and magnetization.....	1
1.1.2 RF pulse and Relaxation time.....	2
1.1.3 Free induction decay and chemical shift.....	3
1.1.4 k -Space and spatial encoding gradient.....	4
1.1.5 Spin-echo and gradient-echo sequence.....	5
1.1.6 Echo planar imaging sequence.....	6
1.1.7 Application.....	6
1.2 Introduction of hyperpolarized ^{13}C imaging.....	7
1.2.1 Carbon-13.....	8
1.2.2 Hyperpolarized ^{13}C	8
1.2.3 Dynamic nuclear polarization.....	9
1.2.4 Hyperpolarized ^{13}C probes.....	10
1.2.5 Hyperpolarized ^{13}C pulse sequences.....	12

1.3	Radiofrequency hardware	15
1.3.1	RF coil concept	15
1.3.2	RF coil design	16
1.3.3	Dual-frequency RF coil.....	17
1.3.4	Transmit-only, receive-only mode.....	18
1.4	Glioma.....	19
1.4.1	Background of glioma.....	19
1.4.2	Glioma therapy.....	19
1.4.3	Tumour metabolism	20
1.4.4	Tumour pH.....	22
1.5	Objectives and hypothesis.....	23
	References for Chapter 1.....	25
	Chapter 2.....	28
2	Construction and evaluation of a switch-tuned $^{13}\text{C} - ^1\text{H}$ birdcage radiofrequency coil for imaging the metabolism of hyperpolarized ^{13}C -enriched compounds	28
2.1	Introduction.....	28
2.2	Methods.....	29
2.2.1	Coil Geometry.....	29
2.2.2	Resonator Circuit	29
2.2.3	Matching Circuitry Baluns.....	32
2.2.4	Shield	32
2.2.5	RF Coil and Animal Support	32
2.2.6	Surface Coil	33
2.2.7	Power Supply and Switching Circuit.....	35
2.2.8	Imaging Phantom	35
2.2.9	Coil Calibration.....	35

2.2.10 Phantom Imaging	35
2.2.11 B_1 Mapping	36
2.2.12 Hyperpolarization	36
2.2.13 Animal Imaging	36
2.3 Results.....	38
2.3.1 Initial Coil performance	38
2.3.2 SNR Comparison Using Phantoms.....	39
2.3.3 B_1 Homogeneity	39
2.3.4 <i>In Vivo</i> Imaging.....	40
2.4 Discussion.....	41
2.5 Acknowledgements.....	45
References for Chapter 2.....	46
Chapter 3.....	48
3 Monitoring early changes in tumour metabolism in response to therapy using hyperpolarized ^{13}C MRSI in a preclinical model of glioma	48
3.1 Introduction.....	48
3.2 Methods.....	51
3.2.1 Pyruvic acid sample preparation.....	51
3.2.2 Hyperpolarization	51
3.2.3 <i>In Vivo</i> Imaging.....	52
3.2.4 Animal disease model	53
3.2.5 Histology.....	53
3.2.6 Image analysis.....	54
3.2.7 Statistics	55
3.3 Results.....	56
3.4 Discussion.....	62

3.5 Acknowledgements.....	68
References for Chapter 3.....	69
Chapter 4.....	74
4 Longitudinal Measurement of Intra- and Extracellular pH gradient in a Rat Model of Glioma.....	74
4.1 Introduction.....	74
4.2 Methods.....	76
4.2.1 ¹³ C Bicarbonate Sample Preparation	76
4.2.2 Hyperpolarization	76
4.2.3 Phantom Imaging.....	77
4.2.4 Animal Model.....	78
4.2.5 Chemical Exchange Shift Imaging for Intracellular pH	78
4.2.6 Hyperpolarized ¹³ C Bicarbonate MRSI for Extracellular pH.....	79
4.2.7 Data analysis	79
4.2.8 Statistics	80
4.2.9 Histology.....	81
4.3 Results.....	81
4.4 Discussion.....	87
4.5 Acknowledgements.....	91
References for Chapter 4.....	92
Chapter 5.....	95
5 Summary and Future work.....	95
5.1 Construction and evaluation of a switch-tuned ¹³ C – ¹ H RF coil	97
5.2 Quantifying early therapeutic response using hyperpolarized [1- ¹³ C]pyruvate MRSI.....	98
5.3 Longitudinal Measurement of pH gradient.....	99
5.4 Future work.....	100

References for Chapter 5.....	102
Appendices A- 1: Permission for reproduction of Scientific articles	104
Appendices A- 2: Animal use protocol.....	106
Curriculum Vitae	111

List of Tables

Table 1-1 Comparison between properties of ^1H and ^{13}C nuclei that affect the signal strength in MRI.....	8
Table 2-1 Network analyzer (Agilent E5061B) measurements of RF coil performance*	37

List of Figures

- Figure 1-1 Shows the magnetization, M_0 , after excitation by an RF pulse. M_0 is perturbed by an angle θ away from B_0 (along the z -axis) by excitation of an RF pulse. The longitudinal part of M_0 , M_z recovers asymptotically to the equilibrium value, M_0z , defined by Equation 2 in a time governed by the spin-lattice relaxation time, T_1 . The transverse component of the magnetization, M_t rotates in the x - y plane at the Larmor frequency. The magnitude of M_t decays exponentially with the effective time constant T_2^* 3
- Figure 1-2 Simplified diagrams of a spin-echo and a gradient-echo sequence. Each line shows application of the RF excitation pulse, the slice select gradient, x and y gradients. G_p and G_f represent the duration of phase and frequency encoding gradients. Boxes illustrate the trajectory of the 180° RF pulse, G_p and G_f in k -space. 6
- Figure 1-3 Simplified diagram of FID-CSI sequence and its data analysis. a) Each line shows application of the RF excitation pulse, the slice select gradient, x and y gradients and signal. G_p represents the duration of phase encoding gradients. Box a) illustrates the trajectory G_p and where the signal is stored in 3D k -space (with coordinate, k_x, k_y). Box b) illustrates the 3D image-space (with coordinate, x, y) after 2D Fourier transformation from 3D k -space. Each voxel a contains FID as shown in c). These FIDs can be transformed to spectra as shown in d) by a 1D Fourier transform..... 13
- Figure 1-4 Simplified circuit diagrams of $^{13}\text{C} - ^1\text{H}$ switch-tuned RF coil. a) shows the switch-tuned coil operating as a band-pass bird cage coil (^1H mode). Here, the PIN diodes are reverse biased and the end ring capacitors are not bypassed by the diodes. b) shows the switch-tuned coil operating as a low-pass bird cage coil (^{13}C mode). Here the PIN diodes are forward biased and AC current is bypassed around the end ring capacitors. 17
- Figure 1-5 Use of hyperpolarized $[1-^{13}\text{C}]$ pyruvate and ^{13}C bicarbonate for quantifying tumour metabolism and tumour pH. $[1-^{13}\text{C}]$ pyruvate and ^{13}C bicarbonate are delivered by the vasculature. $[1-^{13}\text{C}]$ pyruvate is transported into the cytoplasm of tumour (or healthy) cells by monocarboxylate transporter (MCT). Increased LDH activity in tumour cells shifts the chemical equilibrium between pyruvate and lactate, creating a larger pool of endogenous

lactate in the cytoplasm. This results in a greater concentration of [1-¹³C]lactate relative to [1-¹³C]pyruvate in tumour cells compared to healthy cells. Excess protons and acids are pumped out of the tumour into the interstitial space. The pH of the extracellular space is buffered by ¹³C bicarbonate, which converts the excess protons to water and ¹³C-labelled carbon dioxide..... 21

Figure 2-1 Simplified circuit diagram of the switch-tuned ¹³C - ¹H RF coil. The capacitors on the end rings and rungs had slight variations in value. The switch-tuned ¹³C - ¹H RF coil had a total of four RF connections, a pair for each frequency of operation. 31

Figure 2-2 Detailed schematic of the RF configuration for transmit-only, receive-only operation of the switch-tuned ¹³C - ¹H RF coil. The T/R switch provided an RF transmit pulse including a DC offset bias during transmission. The RF pulse was applied to the ¹³C quadrature hybrid circuit, which drives the switch-tuned ¹³C - ¹H RF coil in quadrature operation. In a parallel circuit, a tank circuit filtered AC current from the transmit pulse. The resulting DC bias from the transmit pulse (present only during RF transmission) was used to trigger the MOSFET circuit to supply DC current to bias the PIN diodes of the RF coils. ... 34

Figure 2-3 ¹H (¹H FGRE) and ¹³C (¹³C bbFGRE) images of a rat-sized ¹³C/¹H phantom were acquired with single- and switch-tuned ¹³C - ¹H RF coils for SNR comparison. c,f: ¹³C spectra (¹³C FID-CSI Spectrum) of a thermally polarized [1-¹³C]sodium acetate phantom were also acquired using both RF coils. The percentage SNR for the switch-tuned ¹³C - ¹H RF coil was with respect to the single-tuned coil for either ¹H or ¹³C nuclei..... 38

Figure 2-4 Comparison of ¹³C images with a thermally polarized [1-¹³C]sodium acetate phantom acquired using three different RF coils. SNR measurements were normalized to 100% for the single-tuned ¹³C RF coil..... 39

Figure 2-5 *B*₁ map obtained from the switch-tuned ¹³C - ¹H RF coil with a phantom (shown at left). Nominal flip angle, α was 6°. The *B*₁ profile was acquired axially through the phantom at the red line shown on the *B*₁ map..... 40

Figure 2-6 Summed ¹³C spectrum (left) and individual ¹³C spectra (right) overlaid on a *T*₂-weighted ¹H image of a rat's head. a) Relevant spectral peaks labeled 1 through 5 (summed from individual spectra at right) were respectively: lactate, pyruvate hydrate, alanine,

pyruvate and bicarbonate. b) A brain tumour was outlined in red. Notice the elevated lactate-to-pyruvate ratio in tumour voxels compared with healthy brain tissue..... 41

Figure 3-1 Hyperpolarized ^{13}C spectra of a rat brain with tumour. b) Regional spectral data overlaid on T_2 -weighted image. Tumour has been outlined in cyan. a) & c) Individual spectra from tumour and contralateral brain voxels. Red lines represent line fitting to spectral data in yellow. Note the increased lactate signal relative to pyruvate signal in the tumour voxel..... 52

Figure 3-2 Kaplan-Meier survival plot. Tumour implantation surgery was on Day 0 and the experimental endpoint was Day 24. Therapies were initiated on Day 10, lasting 2 days for radiotherapy and 5 days for chemotherapy. Specific details regarding the therapies are included in the text..... 56

Figure 3-3 A single representative animal from the *no therapy* group. a) Lactate-to-Pyruvate ratio maps are overlaid on axial proton images of the rat brain at longitudinal imaging time points. Tumours are outlined by cyan boundaries. b) Bar graph of measured lactate-to-pyruvate ratio of tumours and contralateral brain volumes at different imaging sessions. c) Graph of tumour volume for all imaging time points. The error bars for Lac/Pyr data represent one measurement standard deviation. The uncertainty for the tumour volume was estimated from inter-observer measurement variability. 57

Figure 3-4 Representative animal from the *combined therapy* group. a) Lactate-to-Pyruvate ratio maps are overlaid on axial proton images of the rat brain at longitudinal imaging time points. Tumours are outlined by cyan boundaries. b) Bar graph of measured lactate-to-pyruvate ratio of tumours and contralateral brain volumes at different imaging sessions. Treatment periods are indicated as hatched areas. c) Graph of tumour volume for all imaging time points. The error bars for Lac/Pyr data represent one measurement standard deviation. The uncertainty for the tumour volume was estimated from inter-observer measurement variability. 58

Figure 3-5 Longitudinal assessment of the lactate-to-pyruvate ratio in tumour tissue for four therapy groups. Radio- and chemotherapy were initiated on day 10 for a duration of 2 and 5 days respectively. No statistical comparison between the no therapy and other treatment groups was possible for days 21 and 24 due to the poor survival of the untreated group.

(Details of therapy are in the text.) Error bars represent one standard deviation for the averaged animal data..... 59

Figure 3-6 Comparison of T_2 -weighted images, lactate-to-pyruvate ratio maps, H&E staining and hypoxia staining for a representative no-therapy and combined therapy animal. A non-rigid image registration method has been used to co-register the histology to the MRI data. Magnified regions for H&E and hypoxia staining are presented next to the histology for the entire brain. Hypoxia staining (Pimonidazole) shows green contrast with blue nucleus counter staining. 60

Figure 3-7 Correlation plots for all experimental animal groups. a) Correlation plot of lactate to pyruvate ratio in tumour versus tumour volume b) Correlation plot of lactate to pyruvate ratio in tumour versus tumour growth rate. The Pearson correlation coefficients are 0.287 ($p \sim 0.105$) and 0.66 ($p < 0.001$) and R^2 -values are 0.083 and 0.416 for panels a) and b) respectively. Tumour volumes (in mm^3) were estimated at each imaging time point from T_1 -weighted images acquired after contrast enhancement. An exponential growth model was fit to the tumour volume data to estimate tumour growth rate in mm^3/day 61

Figure 4-1 Calibration data for different pH-buffered solutions mixed with hyperpolarized ^{13}C bicarbonate. a) A pH map derived from ^{13}C MRSI and the corresponding pH values obtained by pH meter. b) The linear regression between measured pH (pH meter) and observed pH (hyperpolarized ^{13}C bicarbonate) with $R^2 = 1$ 77

Figure 4-2 The progression of intra- and extracellular pH of a representative C6 glioma. Panels a) b) and c) present the T_2 -weighted images, and intra-and extracellular pH maps of the rat brain at days 8 and 12. Tumours are contoured in magenta. d) Quantification of changes of intra- and extracellular tumour pH. Statistical significance is annotated with letters (measurements with different letters are significant at $p < 0.05$). e) Longitudinal tumour volume measurements. Inter-observer variability was used for the error bar. A large region of necrosis within the tumour is evident on day 12 in panel a). This animal was sacrificed prior to the final imaging time point on day 15 due to neurological impairment. . 82

Figure 4-3 The progression of intra- and extracellular pH of a representative C6 glioma. Panels a) b) and c) present the T_2 -weighted images, and intra-and extracellular pH maps of

the rat brain at days 8, 12 and 15. Tumours are contoured in magenta. d) Quantification of changes of intra- and extracellular tumour pH. Statistical significance is annotated with letters. e) Longitudinal tumour volume measurements. Inter-observer variability was used for the error bar. 83

Figure 4-4 Longitudinal changes in cohort-averaged pH measurements. Panel a) &b) shows intra- and extracellular pH in tumour and contralateral brain measured on days 8, 12 and 15. Panel c) compares cellular pH gradient between tumour and contralateral brain at those same days. d) Average gross tumour volume measured from T_2 -weighted imaging data. Inter-observer variability was used for the error bar. All statistical significances ($p < 0.05$) are annotated with letters. 85

Figure 4-5 Correlation plot comparing pH gradient and tumour volume. Tumours that did not exhibit necrosis show a significant correlation (green line) between pH gradient and tumour volume ($p < 0.05$, Pearson correlation = 0.72). 86

Figure 4-6 Histology of the 2nd representative animal shown in Figure 4-3. The first column presents the tumour extent, pH_i and pH_e within the rodent brain. The tumour margin is outlined in magenta. The second column contains histology including H&E, HIF-1 α and Ki-67 staining of tumour and brain tissue. The third column of images contains magnified histology of the regions outlined by respective boxes in column 2. 87

List of Appendices

Appendices A- 1: Permission for reproduction of Scientific articles	104
Appendices A- 2: Animal use protocol.....	106

List of Abbreviations

^{13}C	non-radioactive isotope of carbon with 6 protons and 7 neutrons
^{18}F -FDG	2-deoxy-2-(^{18}F)fluoro-D-glucose
^1H	proton or hydrogen atom (nucleus)
2D	two-dimensional
AACID	amine and amide concentration-independent detection
AC	alternating current
ATP	adenosine triphosphate
B_0	main magnetic field strength for MRI
B_1	radiofrequency magnetic field for MRI
bbFGRE	broad-banded FGRE
C	capacitor
CEST	chemical exchange saturation transfer
CO_2	carbon dioxide
DC	direct current
DNA	deoxyribonucleic acid
DNP	dynamic nuclear polarization
DSC	dynamic susceptibility contrast
EPI	echo planer imaging
ETL	echo train length
FAI	flip-angle imaging
FGRE	fast gradient-recalled echo
FID	free induction decay
FID-CSI	free induction decay chemical shift imaging
FOV	field-of-view
FSE	fast spin-echo
Gd	gadolinium
G_f	frequency encoding gradient
G_p	phase encoding gradient
H&E	hematoxylin and eosin stain
HCO_3^-	bicarbonate
L	inductor
Lac/Pyr	lactate-to-pyruvate (ratio)
LDH	lactate dehydrogenase
M_0	longitudinal magnetization
MOSFET	metal-oxide-semiconductor field-effect transistor
MRI	magnetic resonance imaging
MRSI	magnetic resonance spectroscopic imaging
M_t	transverse magnetization
NAD $^+$	oxidized nicotinamide adenine dinucleotide
NADH	reduced nicotinamide adenine dinucleotide
OD	outer diameter
PET	positron emission tomography
pH	potential of hydrogen
pH $_e$	extracellular pH
pH $_i$	intracellular pH

Q	quality factor
R	resistor
R_1	spin-lattice relaxation rate ($R_1 = 1/ T_1$)
R_2	spin-spin relaxation rate ($R_2 = 1/ T_2$)
R_2^*	effective spin-spin relaxation rate ($R_2^* = T_2^*$)
RANO	response assessment in neuro-oncology
RECIST	response evaluation criteria in solid tumours
RF	radiofrequency
SNR	signal-to-noise ratio
T/R	transmit/receive
T_1	spin-lattice relaxation time
T_2	spin-spin relaxation rate time
T_2^*	effective spin-spin relaxation time
TE	time-to-echo
TMZ	temozolomide
TORO	transmit-only, receive-only
TR	time-to-repetition
WASSR	water saturation shift referencing
WHO	world health organization
α	flip angle
γ	gyromagnetic ratio
ω_0	Larmor angular frequency

Chapter 1

1 Introduction

1.1 Introduction to ^1H Magnetic Resonance Imaging

In this section, general background information is provided for the magnetic resonance imaging (MRI) methods relevant to this research. In particular, information regarding nuclear spin, magnetization, RF pulses, relaxation, free induction decay, chemical shift, k -space, spatial encoding, spin-echo and gradient-echo sequences, echo planar imaging sequences and their applications will be provided. Further detailed explanation of those topics can be found in several references. [1, 2]

1.1.1 Nuclear spin and magnetization

Conventional MRI involves exploiting the properties of the magnetic dipole moments of protons (^1H) as they interact with their environment for its imaging contrast. In the absence of a magnetic field, the orientation of the magnetic dipoles of protons will be random. However, in an external magnetic field, \mathbf{B}_0 , the nuclear magnetic dipole moments precess around the magnetic field direction at the Larmor frequency:

$$\omega_0 = 2\pi\gamma B_0 \quad \text{Equation 1-1}$$

where γ , is a nuclear property of the proton known as gyromagnetic ratio related to its magnetic dipole moment (for ^1H , $42.576 \times 10^6 \text{ Hz T}^{-1}$). As an ensemble of magnetic dipoles precesses in the magnetic field, longitudinal spin-lattice relaxation will cause the distribution of dipole directions to have a small alignment with the magnetic field. (In MRI, the direction of this field is assumed to be along the z -axis.) This produces a net longitudinal magnetization (\mathbf{M}_0), known as the thermal equilibrium magnetization, in the direction of the magnetic field given by:

$$M_0 \hat{z} = \frac{\rho_0 \gamma^2 \hbar^2}{4kT} B_0 \hat{z} . \quad \text{Equation 1-2}$$

Here, ρ_0 is defined as the number of protons per volume, \hbar is known as the reduced Planck constant ($h/2\pi$), k is the Boltzmann constant and T is the temperature of the sample. The thermal equilibrium magnetization achievable at body temperature and clinical field strength is small and is the major factor limiting the signal-to-noise ratio (SNR) for MRI. In the human body, the average ^1H concentration in tissue is large, $\sim 88\text{M}$ [1], which makes MRI possible for *in vivo* imaging with protons.

1.1.2 RF pulse and Relaxation time

In order to detect \mathbf{M}_0 , it must be “tipped away” or perturbed from its equilibrium along \mathbf{B}_0 . This is achieved by application of a transverse radiofrequency (RF) magnetic field, \mathbf{B}_1 , oscillating at the Larmor frequency produced by an RF transmit coil. This excites \mathbf{M}_0 so that it precesses around the z -axis at an angle α , which is known as the flip angle. For example, when an RF pulse is applied that produces a 90° flip angle, all the magnetization is excited and precesses at the Larmor frequency in the x - y plane orthogonal to \mathbf{B}_0 . Components of the excited magnetization rotating in the transverse plane (M_x and M_y) are referred to as the transverse magnetization, \mathbf{M}_t , where

$$\mathbf{M}_t(t) = M_x(t)\hat{x} + M_y(t)\hat{y}. \quad \text{Equation 1-3}$$

The transverse magnetization can be detected by an RF receive coil as an induced sinusoidal voltage resulting from the oscillating magnetic flux through this coil. As this is occurring, the longitudinal magnetization, M_z , is recovering asymptotically along \mathbf{B}_0 with an exponential time constant given by spin-lattice relaxation time, T_1 , (or its reciprocal $R_1 = 1/T_1$, the spin-lattice relaxation rate):

$$M_z = M_0(1 - e^{-t/T_1}). \quad \text{Equation 1-4}$$

The exponential decay of the magnitude of the transverse magnetization, \mathbf{M}_t , is governed by the spin-spin relaxation time, T_2 , (or its rate $R_2 = 1/T_2$):

$$M_t(t) = M_t(t = 0)e^{-t/T_2} \quad \text{Equation 1-5}$$

The decay of transverse magnetization is due to interactions between spins that cause individual spins to precess at different rates. Ultimately, M_t will decay to zero and this process is referred to as dephasing. In addition to spin-spin interactions, local magnetic field inhomogeneities caused by the inherent magnetic susceptibility of tissues and their interfaces with air can cause the transverse magnetization to decay even faster. This is characterized by the effective spin-spin relaxation time constant, T_2^* (or its rate, $R_2^* = 1/T_2^*$).

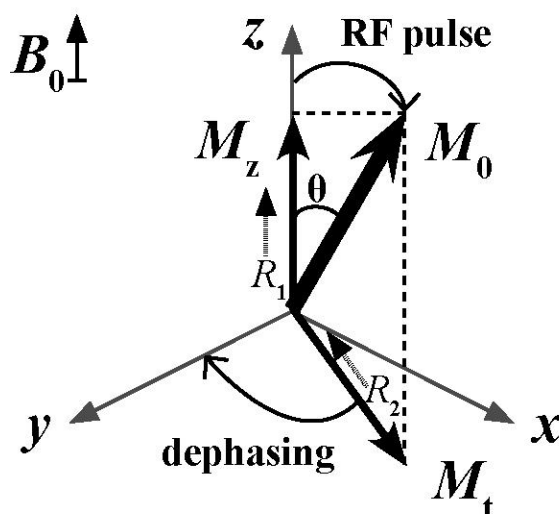


Figure 1-1 Shows the magnetization, M_0 , after excitation by an RF pulse. M_0 is perturbed by an angle θ away from B_0 (along the z -axis) by excitation of an RF pulse. The longitudinal part of M_0 , M_z recovers asymptotically to the equilibrium value, $M_0\hat{z}$, defined by Equation 2 in a time governed by the spin-lattice relaxation time, T_1 . The transverse component of the magnetization, M_t rotates in the x - y plane at the Larmor frequency. The magnitude of M_t decays exponentially with the effective time constant T_2^* .

1.1.3 Free induction decay and chemical shift

The oscillating signal with an exponentially decaying amplitude envelope acquired by the RF coil after excitation is known as a free induction decay (FID). The frequency of the FID deviates slightly from the ^1H Larmor frequency since the protons precess in the local molecular electron cloud in addition to the external field. This molecular distribution of

electrons causes a shielding effect and ultimately a small but observable shift in the Larmor frequency. This small shift is known as the chemical shift. Protons associated with different molecules exhibit different chemical shifts. Magnetic resonance spectroscopic imaging (MRSI) is a technique, which produces maps of the regional distribution of molecules discriminated by their chemical shift. The FID can be converted into a spectrum via a mathematical tool, the Fourier transform. The resulting spectrum contains different spectral lines whose frequencies correspond to the various chemical shifts of the imaged nuclei and whose amplitudes are proportional to their number density. However, due to this small chemical shift in resonant frequency, nuclei with different chemical shifts may appear to be displaced from their actual location. This small, but important imaging artifact is referred as chemical shift displacement.[3]

1.1.4 *k*-Space and spatial encoding gradient

To encode spatial information in MRI, a linearly varying magnetic field (known as a gradient) is applied across the imaging volume. This gradient can be applied along any direction. When gradients are applied during excitation by the RF pulse, a specific slab of the imaging volume can be excited instead of the entire volume. This procedure is known as slice selection. After slice selection, a spatially encoded signal is collected in *k*-space. *k*-Space is a frequency representation of the image and it can be transformed into an image using an inverse-Fourier transform. Ideally, complete coverage of *k*-space is required to produce a detailed image. Systematic application of gradients during signal acquisition determine where data are accumulated in *k*-space (spatial encoding).

For instance, in two dimensions, gradients are used to spatially encode the MRI signal by manipulating the signal frequency and phase. To collect a two-dimensional image, slice selection is used to excite a slab of finite thickness along the *z*-axis. Spatial encoding of the FID signal along the *x*-axis can be accomplished by applying a magnetic field gradient along that axis during acquisition. This is known as frequency encoding. Phase-encoding using short “blips” of a gradient applied along the *y*-axis. This alters the phase of the precessing magnetization along that direction producing spatial encoding of the MRI signal in the *y*-direction. Systematic application of the frequency and phase code gradients and acquisition of the FID signals are controlled by a set of instructions known

as the pulse sequence. After slice selection excitation, a phase-encoding gradient is applied followed by acquisition of the FID signal with frequency encoding to acquire a complete line of k -space. This needs to be repeated several times to acquire all lines of k -space data. The time between each RF excitation pulse is known as the time to repetition (TR).

1.1.5 Spin-echo and gradient-echo sequence

The transverse magnetization can be used more efficiently by refocusing the dephasing spins to create an “echo”. This echo can be induced by application of a 180° RF pulse after the transverse magnetization reaches zero or a dephasing and refocusing gradient during decay. The former technique is called a spin-echo sequence and the latter, a gradient-echo sequence. Multiple echoes can be produced for each RF excitation of the transverse magnetization so that several lines of k -space can be acquired before the transverse magnetization is fully dephased to zero. The time between application of the RF excitation pulse and when the echo is formed is known as the time-to-echo (TE). Spin-echo and gradient-echo sequences and variants are the most frequently used sequences in MRI due to their simplicity and utility.

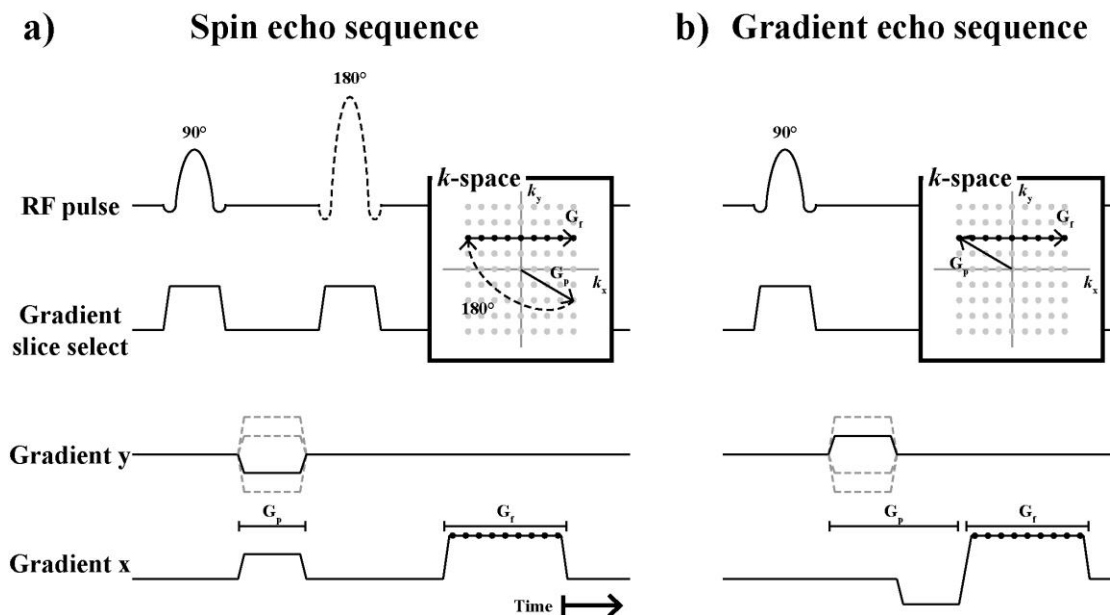


Figure 1-2 Simplified diagrams of a spin-echo and a gradient-echo sequence. Each line shows application of the RF excitation pulse, the slice select gradient, x and y gradients. G_p and G_f represent the duration of phase and frequency encoding gradients. Boxes illustrate the trajectory of the 180° RF pulse, G_p and G_f in k -space.

1.1.6 Echo planar imaging sequence

Another method used in MRI is echo planar imaging (EPI). In this rapid imaging technique, the entire k -space is acquired with a series of gradient echoes using only one or a few RF pulses. EPI requires rapid application of strong magnetic gradients to quickly fill k -space for a given image slice. This can be used to help mitigate image artifacts due to subject motion. However, due to the extended series of gradient echoes, EPI is weighted to T_2^* and is sensitive to field inhomogeneities. EPI is used to detect dynamic changes in structure and contrast in cardiac imaging and perfusion imaging.

1.1.7 Application

1.1.7.1 T_1 -weighted and T_2 -weighted imaging sequences

Different tissues in the body have specific T_1 and T_2 values, which can be used to produce image contrast between them. Using a spin- or gradient-echo sequence as described above, imaging data can be acquired with either T_1 - or T_2 -weighting. To acquire an image

with T_1 -weighted contrast, a gradient-echo sequence can be specified with a TR value on the order of the tissue T_1 value and a short TE value. TE and TR are chosen to minimize the effects of T_2^* blurring and maximize the T_1 contrast. Often a paramagnetic contrast agent such as a gadolinium chelate is used to enhance the contrast of T_1 -weighted images. These contrast agents significantly shorten the T_1 of surrounding tissue, allowing increased signal in T_1 -weighted images. To produce an image with T_2 -weighted contrast, a spin-echo sequence can be used with a long TR value and a TE value on the order of the T_2 values. Spin-echo sequences negate the effects of T_2^* decay. TE and TR are chosen to maximize the contrast related to T_2 relaxation and minimize the effects of T_1 . Fluids, such as cerebral spinal fluid have long T_2 values which are manifested as regions of increased signal in a T_2 -weighted image.

1.1.7.2 Dynamic susceptibility contrast imaging sequence

Dynamic susceptibility contrast (DSC) imaging is a technique that can be used to measure perfusion. DSC exploits the change in image contrast due to a decrease in T_2^* by the introduction of a paramagnetic agent such as a gadolinium chelate. It is common to use a gradient-echo EPI sequence to generate a time series of DSC images. A series of images are rapidly acquired during injection of the contrast agent. The temporal evolution of the signal in individual voxels is examined across the time series as a result of the bolus injection. This signal slowly increases from an initial minimum as the contrast agent clears out of the tissue. Using this signal-time curve, the blood volume and flow can be estimated on a pixel-by-pixel basis to produce tissue maps of these quantities. A more detailed explanation and discussion of the application of DSC imaging is described in reference [4].

1.2 Introduction of hyperpolarized ^{13}C imaging.

This section describes some background information for hyperpolarized ^{13}C imaging. This includes details regarding carbon-13 (^{13}C), hyperpolarization by dynamic nuclear polarization, hyperpolarized ^{13}C -enriched metabolic probes and pulse sequences for data acquisition of hyperpolarized compounds. More detailed explanations and descriptions can be found in references [5-7].

1.2.1 Carbon-13

Ordinary carbon-12 (^{12}C) is ubiquitous in tissues. However, unlike protons, it is MR invisible since it has no nuclear spin (magnetic dipole moment). Therefore, ^{12}C nuclei cannot be aligned by an external magnetic field or manipulated by application of an RF pulse. Among the isotopes of carbon, carbon-13 (^{13}C) is a stable and naturally occurring isotope that has a nuclear spin of $\frac{1}{2}$. Thus, ^{13}C is visible with MRI; however, two major issues complicate its imaging. First, the natural abundance of ^{13}C is 1.11% compared to 98.93% for ^{12}C and 99.98% for ^1H . [8] Since the signal is proportional to the number of ^{13}C nuclei in an imaging voxel, the detectable ^{13}C signal is significantly lower than that of protons. Secondly, the gyromagnetic ratio of ^{13}C is approximately 4 times less than that of ^1H . From equation 1, M_0 is proportional to γ^2 . Furthermore, the FID signal induced in the RF receive coil is also proportional to γ . Therefore, the MRI signal is proportional to γ^3 and it becomes quite evident that it is a significant challenge to perform MRI with ^{13}C nuclei. Although, it is possible to detect ^{13}C signal with MRI, it is very time consuming and not particularly feasible for an *in vivo* study.

Table 1-1 Comparison between properties of ^1H and ^{13}C nuclei that affect the signal strength in MRI.

Nucleus	^1H	^{13}C
Natural abundance	99.98%	1.11%
Gyromagnetic ratio (MHz/T)	42.577	10.705
Relative signal strength	1	0.0002

1.2.2 Hyperpolarized ^{13}C

To counter the limited sensitivity of ^{13}C MRI, a few measures can be taken. Instead of relying on the presence of endogenous naturally abundant (1.11%) ^{13}C in the imaging volume, highly-enriched ^{13}C -labelled molecules can be introduced. In practice, a fairly large dose of ^{13}C -labelled agents would need to be distributed throughout the tissue. High-field MRI would also increase the observed ^{13}C signal but this is an expensive

solution and practical limits exist on field strength. Hyperpolarization is another possible solution to this problem. As the name suggests, hyperpolarization is an *in vitro* process to enhance the magnetization of a sample by increasing the degree of alignment of the contained nuclei beyond that achievable at thermal equilibrium (see Section 1.1.1). In theory, any nucleus with non-zero nuclear spin can be hyperpolarized; however, successful application depends on physical properties of the nucleus and its environment. There are several methods of hyperpolarization but this thesis will focus on the dynamic nuclear polarization (DNP) method used at the Robarts Research Institute.

1.2.3 Dynamic nuclear polarization

In principle, any liquid or solid containing molecules with MRI-sensitive nuclei can be hyperpolarized by this method. The basic principle behind DNP is the transfer of spin polarization from electron to nucleus. This transfer of spin polarization is mediated by microwave irradiation. For this method, a stable radical is doped uniformly throughout a liquid sample containing 100%-enriched ^{13}C molecules. The magnetic dipole moment of an electron is nearly three orders of magnitude larger than that of a proton and, at high magnetic field strengths (3.35 T) and low temperatures (1.4 K), the unpaired electron of the radical is nearly 100% polarized (aligned). By irradiating the pool of polarized electrons from the doped radical with microwaves at a frequency near the electron spin resonance (94 GHz), the electronic polarization can be transferred to surrounding nuclei achieving a very high degree of polarization. [9] However, in this physical state (~ 1.4 K) the frozen hyperpolarized liquids cannot be directly used for *in vivo* imaging. Hyperpolarized compounds must be rapidly warmed to near body temperature, properly buffered and free radicals removed for clinical use. This can be accomplished by quickly mixing it with a super-heated buffer solution at high pressure. This process is referred to as “dissolution” and it allows the buffered hyperpolarized solution to be rapidly prepared for *in vivo* experimentation while preserving most of its magnetization achieved by DNP. Using DNP, the MRI signal from hyperpolarized ^{13}C liquids can be increased 10,000-fold compared to thermal equilibrium. A detailed explanation of the method DNP is presented in reference [6].

1.2.4 Hyperpolarized ^{13}C probes

Since carbon is the backbone of almost all biological molecules, it is possible to label almost any biological molecule with ^{13}C for use as a hyperpolarized contrast agent. However, for hyperpolarized ^{13}C probes to be of practical use, a few details need to be considered. Firstly, the T_1 values of these probes must be sufficiently long enough to sustain their magnetization for MRI. Although hyperpolarization can greatly increase the potential signal achievable from ^{13}C -enriched compounds, this signal rapidly disappears as the magnetization decays to the thermal equilibrium magnetization by spin-lattice relaxation governed by the T_1 value. After a time interval equal to $3 \times T_1$, approximately 95% of signal is already lost. Before the sample is completely relaxed, the hyperpolarized ^{13}C probe must be transported to the MRI, injected and circulated through the vasculature into the tissue of interest and rapidly imaged with MSRI. Furthermore, *in vivo* T_1 relaxation is faster than *in vitro* T_1 relaxation due to interaction with other molecules in the vasculature and tissues. Secondly, ^{13}C nuclei in different positions in a molecule likely possess different chemical shifts due to spin-spin couplings. This is known as magnetic inequivalence. This leads to splitting of the ^{13}C signal producing a more complicated nuclear magnetic resonance spectrum. Finally, as a probe of *in vivo* metabolism the hyperpolarized agent must be delivered quickly and rapidly undergo metabolism within the tissue of interest before imaging. As a result, the single most limiting factor for effective imaging of hyperpolarized ^{13}C imaging is the finite T_1 value of the ^{13}C nucleus. For ^{13}C nuclei in small endogenous molecules, *in vitro* T_1 values of tens of seconds are possible facilitating imaging of their metabolism. In this thesis, the *in vivo* use of two hyperpolarized ^{13}C metabolic probes will be presented: $[1-^{13}\text{C}]$ pyruvate and ^{13}C bicarbonate.

1.2.4.1 $[1-^{13}\text{C}]$ pyruvate

$[1-^{13}\text{C}]$ pyruvate is the most commonly used hyperpolarized ^{13}C probe for *in vivo* metabolic imaging. Also, it is the first in-human hyperpolarized imaging probe. [10] ^{13}C pyruvate has been used for investigating metabolism in cardiac disease, prostate, breast and brain cancers in different animal models including murine, rat, and pig models. [11-14] This broad use of pyruvate can be explained by its several advantages. First,

pyruvate is a key metabolite at the center of an important metabolic pathway. Pyruvate can be converted into carbohydrates, fatty acids, amino acids and metabolic energy. Pyruvate is readily used by tissue with high metabolic activity. Commonly in cancer, pyruvate is converted to lactate instead of contributing to the Krebs cycle. [15] Measuring conversion between pyruvate and lactate is a straight forward process using hyperpolarized ^{13}C MRSI. In this case, the first carbon of pyruvate is labelled. If a study of a pathway within the Krebs cycle is desired, then the second carbon of pyruvate is labelled instead or as well. Secondly, the C_1 of pyruvate has a relatively long T_1 approximately 65 s at 3T. [16] This long T_1 ensures that the magnetization of ^{13}C -pyruvate is sustained during delivery to the tissues of interest and conversion into other metabolites. Finally, pyruvate (with a single ^{13}C label) is detected as a single spectral peak and its metabolic byproducts are well separated by chemical shift. This facilitates accurate quantification of the concentration of the metabolite and its metabolic products. In this thesis, $[1-^{13}\text{C}]$ pyruvate was used to probe metabolism to $[1-^{13}\text{C}]$ lactate. In terms of chemical shifts, $[1-^{13}\text{C}]$ pyruvate is separated by 12 ppm from $[1-^{13}\text{C}]$ lactate and 4 ppm from $[1-^{13}\text{C}]$ alanine.

1.2.4.2 ^{13}C Bicarbonate

Another hyperpolarized ^{13}C probe relevant to this thesis is ^{13}C bicarbonate. pH imaging with ^{13}C bicarbonate has been demonstrated in animal models of disease. [17] Bicarbonate plays an important role in the pH buffer system. Tissues maintain pH through a balance of bicarbonate and carbon dioxide (CO_2) under the influence of carbonic anhydrase. The ratio of bicarbonate and CO_2 concentrations can be used to estimate the pH of tissue using the Henderson-Hasselbalch equation as follows:

$$\text{pH} = \text{p}K_a + \frac{[\text{HCO}_3^-]}{[\text{CO}_2]}. \quad \text{Equation 1-6}$$

Here, $\text{p}K_a$ (6.17) is the logarithmic acid dissociation constant and $[\text{HCO}_3^-]$ and $[\text{CO}_2]$ are the concentrations of bicarbonate and CO_2 respectively. By labelling bicarbonate with ^{13}C , the ratio of bicarbonate and carbon dioxide concentrations can be measured using hyperpolarized ^{13}C MRSI and maps of tissue pH are readily obtained. Since uptake of bicarbonate by cells is slow compared to *in vivo* spin lattice relaxation of ^{13}C bicarbonate,

this method measures pH in the extracellular space. Unfortunately, the *in vitro* T_1 of ^{13}C bicarbonate is only ~ 33 s, and ~ 10 s *in vivo* at 3T. [18] This is much faster relaxation than for ^{13}C pyruvate. Therefore, imaging of hyperpolarized ^{13}C bicarbonate must be performed quickly. The use of deuterium oxide instead of water as the solvent for the dissolution media can significantly increase T_1 . [18] However, a large dose of deuterium oxide could alter *in vivo* metabolism and at significant volumes is poisonous in animals. [19] ^{13}C bicarbonate and $^{13}\text{CO}_2$ possess single spectral peaks, which are well separated by a 36-ppm chemical shift.

1.2.5 Hyperpolarized ^{13}C pulse sequences

Due to the limitation of finite T_1 values of hyperpolarized ^{13}C compounds, MRI sequences must be efficient. This includes imaging time and use of the ^{13}C probe magnetization. The magnetization of the ^{13}C nucleus relaxes to thermal equilibrium in tens of seconds and the DNP process requires approximately an hour to hyperpolarize another sample for injection so that signal averaging as used in conventional MRI is not a realistic option. Therefore, the magnetization of the hyperpolarized sample must be excited with a series of small flip angle RF pulses to conserve the initial magnetization for the acquisition of all k -space data. In addition, a short TR is required to preserve SNR. Two imaging sequences were used in this thesis: free induction decay chemical shift imaging and spectrally selective spiral imaging.

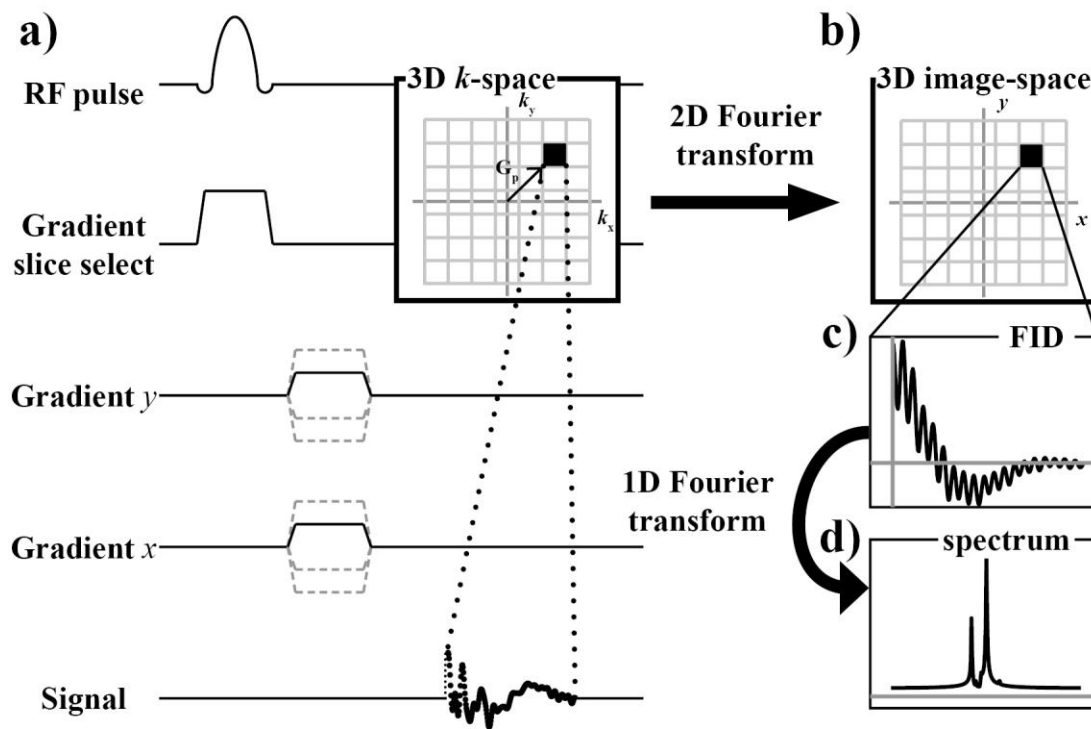


Figure 1-3 Simplified diagram of FID-CSI sequence and its data analysis. a) Each line shows application of the RF excitation pulse, the slice select gradient, x and y gradients and signal. G_p represents the duration of phase encoding gradients. Box a) illustrates the trajectory G_p and where the signal is stored in 3D k -space (with coordinate, k_x , k_y). Box b) illustrates the 3D image-space (with coordinate, x , y) after 2D Fourier transformation from 3D k -space. Each voxel a contains FID as shown in c). These FIDs can be transformed to spectra as shown in d) by a 1D Fourier transform.

1.2.5.1 FID-CSI

Free induction decay chemical shift imaging (FID-CSI) is an enhanced version of a free induction decay pulse sequence. After the RF excitation pulse and slice selection gradient, phase gradients are added to encode spatial information. The resulting three-dimensional k -space is a data matrix where the first and second dimensions represent spatial space of k_x & k_y and the third dimension (spectral space) represents the spatially encoded FID of that k -space coordinate. Once, the spatial portion of k -space is Fourier transformed into image space, the remaining spectral dimension represents the FIDs of an individual image voxel. The equation representing this FID is given here:

$$S(t) = \sum_{n=1}^m A_n e^{-i\Omega_n t + \phi_n} e^{-R_{2n}^* t} . \quad \text{Equation 1-7}$$

$S(t)$ is the signal at time, t , m is the number of spectral lines with unique chemical shifts. A_n is the amplitude, Ω_n is the frequency offset, ϕ_n is the phase offset, and R_{2n}^* is the effective spin-spin relaxation rate of spectral component, n . The number of spectral lines depends on the number of metabolites in the spectrum and the number of inequivalent ^{13}C nuclei per metabolite. As the number of spectral lines becomes large, spectral overlap becomes a potential difficulty. For the metabolites used in this thesis, their spectra are largely well separated and signal parameters can be accurately estimated from fitting equation 1-7 to the FID data. In particular, the amplitude of each metabolite in the FID is extracted, which is used to estimate the relative amount of ^{13}C metabolite in each imaging voxel. This produces the same result as measuring the area of a spectral line. Voxel-by-voxel spectra can be produced by Fourier transformation and displayed as a function of chemical shift from the peak (*i.e.* major) metabolite in ppm. The spatial resolution of the spectral data is limited by the number of RF pulses and ultimately the total sample magnetization. Since each k -space point requires an RF excitation pulse, even with small flip angle excitation, only a limited k -space matrix can be acquired with sufficient SNR, resulting in a relatively low-resolution image. The k -space matrix can be artificially increased by zero-filling in spatial or spectral dimensions to increase the apparent resolution after transformation. However, this does not actually improve resolution, but it may be desired for aesthetic reasons. Often, a Gaussian filter is used to apodize the FID signal to reduce high frequency noise in the resulting spectrum. Further mathematical details regarding the relationship between the FID signal and resulting spectrum can be found in reference [20].

1.2.5.2 Spectrally selective spiral imaging

This sequence was developed by Dr. Rolf F. Schulte (General Electric Healthcare) and is described in detail in reference [21]. For this sequence, a spectrally selective RF excitation pulse is employed. This RF pulse excites only a chosen metabolite(s) based on its unique chemical shift(s). Then, the k -space data is acquired with a two-dimensional spiral trajectory through k -space. Unlike, the Cartesian k -space acquisition described

before, k -space is encoded in polar coordinates and then re-gridded into a Cartesian coordinate system. The advantage of this method is that the regional distribution map for each metabolite can be generated with a single RF pulse. Each metabolite is separately excited and imaged serially. This is a very fast process so that even though data for different metabolites are collected at slightly different times, relative metabolite concentrations can still be assumed to be the ratios of the observed metabolite signals. Furthermore, each metabolite map can be averaged to improve SNR until all the magnetization has been expended or relaxed and the flip angle can be separately optimized for each metabolite to further increase efficient use of the magnetization. However, because only a narrow band of excitation frequencies is employed, it is important to carefully calibrate the excitation frequencies and bandwidths to coincide with the chemical shifts of the metabolites of interest.

1.3 Radiofrequency hardware

Details of the bespoke radiofrequency (RF) coil for $^{13}\text{C}/^1\text{H}$ MRI are discussed in this section. This includes consideration of RF materials and components, RF design, dual-frequency operation and transmit-only, receive-only (TORO) operation. Complete details can be found in these references [22, 23].

1.3.1 RF coil concept

The purpose of the RF coil is to generate a uniform RF magnetic field, \mathbf{B}_1 for sample excitation and to detect the resulting \mathbf{M}_t . To maximize its efficiency for both excitation and detection, an RF coil must resonate (be tuned) at the Larmor frequency of a particular nucleus (*i.e.* ^1H or ^{13}C). Also, the RF coil must be “matched” for a specific impedance (usually 50Ω) The RF coil circuit can be represented as an array of lumped circuit elements including resistors (R), inductors (L) and capacitors (C). The relationship between L , C and resonant angular frequency (ω_0) is described by the equation:

$$\omega_0^2 = \frac{1}{LC}. \quad \text{Equation 1-8}$$

The geometry of the RF conductors within the RF structure and the choice of conductor material determines the inductances and resistances. Then, capacitors are added to

achieve resonance at a particular frequency. These capacitances can be considered as tuning capacitors (C_t), since it is difficult to alter the inductance of the RF structure, without changing its physical dimensions or materials. The impedance of the RF coil must be matched to that of the rest of the RF transceiver chain including the transmission lines that connects the RF coil to the excitation source and RF detector. Without proper impedance matching, the measured FID will be attenuated by signal reflections. This is accomplished by adding a circuit to transform the impedance of the RF coil to 50Ω . Finally, a “balun” is added to the RF circuitry to unbalanced the RF signal. The balun reduces RF current in the shields of coaxial cables and inputs. This provides the desired optimum signal transmission and compatibility with the RF transceiver chain.

1.3.2 RF coil design

There are many RF coil designs suitable for MRI. The key objective is to design a circuit that will provide an oscillating magnetic field perpendicular to \mathbf{B}_0 . The simplest design is a loop circuit. It is known as a surface RF coil, which has a very high sensitivity for a limited imaging volume near the plane of the circuit loop. It is relatively easy to construct and it is placed very near or against the imaging volume. In principle, the loop can also be multi-turned or have a curved or complex topology to conform to the size and shape of imaging volume. Surface coils are not used for RF excitation because they have poor RF homogeneity even over a limited region of interest. However, the resulting limited field of view makes them ideal RF receive antennae since they only detect noise from a small volume. In general, the sensitivity of the surface coil drops off rapidly for distances greater than the physical dimensions (*i.e.* diameter or length) of the RF coil.

Another common RF design is known as the birdcage RF coil, named for its physical structure. As name suggests, this design is composed of two end rings connected by several rungs resulting in a structure that looks like the skeleton of a birdcage. A birdcage RF coil produces a very homogenous \mathbf{B}_0 field as the number of rungs employed are increased. However, the sensitivity of this architecture can be severely influenced by interactions (loading) of the coil with its imaging sample. Based on where the capacitors are added to resonate the RF circuit, three distinct RF architectures can be identified. For low-pass architecture, the capacitors are inserted into the rungs. For high-pass

architecture, they are introduced between rung connections on both of the end rings. When capacitors are added to end rings and rungs, this produces a band-pass architecture. The choice of birdcage architecture largely depends on the resonant frequency as well as the complexity and cost of the number of capacitors. Birdcage RF coils produce a B_1 field, which rotates in the transverse plane, perpendicular to rungs, when it is driven by two RF signals with a 90° phase difference. This is known as quadrature operation, which also increases the receive sensitivity of the RF coil by a factor of $\sqrt{2}$ compared to operation with a single RF connection (port). Quadrature operation requires special hardware to achieve the 90° phase offset between ports.

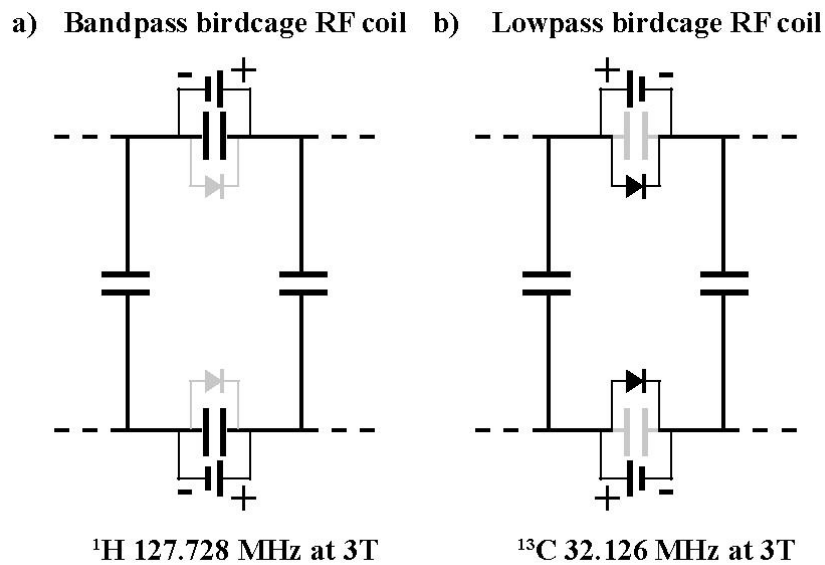


Figure 1-4 Simplified circuit diagrams of $^{13}\text{C} - ^1\text{H}$ switch-tuned RF coil. a) shows the switch-tuned coil operating as a band-pass bird cage coil (^1H mode). Here, the PIN diodes are reverse biased and the end ring capacitors are not bypassed by the diodes. b) shows the switch-tuned coil operating as a low-pass bird cage coil (^{13}C mode). Here the PIN diodes are forward biased and AC current is bypassed around the end ring capacitors.

1.3.3 Dual-frequency RF coil

A simple RF coil is typically optimized to resonate at one chosen frequency. For metabolic imaging with ^{13}C MRSI, it is desirable for the RF hardware to be capable of operating at the Larmor frequencies of ^1H to assess morphology and ^{13}C nuclei to map

metabolism. In principle, this could be accomplished with separate RF coils; however, changing RF coils is inconvenient and disturbs image registration between morphological and metabolic data. The use of an RF system, which is simultaneously resonant at both frequencies or that can be rapidly “switch-tuned” between frequencies eliminates the need for subsequent image registration and its associated uncertainties and expedites data collection.

RF architectures for multi-nuclear imaging are inherently more complex than single-tuned RF systems and, as a result, often have reduced signal sensitivity and potential losses in image SNR must be weighed against the advantages of image registration and convenience. This research employed an RF system, which uses a switch-tuning strategy to achieve the highest possible SNR for dual-frequency operation. This was accomplished through the incorporation of PIN (PN junction with isolation region) diodes to change the RF coil architecture between low-pass (^{13}C) and band-pass (^1H) operation (See Figure 1-4). In this scheme, the PIN diodes are placed in parallel with the end ring capacitors. When the PIN diodes are forward biased by application of a DC bias, the end ring capacitors are bypassed and the RF coil resonates at the ^{13}C Larmor frequency as a low-pass RF coil. Reverse biasing the PIN diodes enables band-pass operation at the ^1H frequency. In addition, a ^{13}C RF surface coil was added for transmit-only, receive-only operation to further improve ^{13}C SNR.

1.3.4 Transmit-only, receive-only mode

As described in chapter 1.1.2, transmission and reception are usually accomplished by a single RF coil. For transmit-only, receive-only (TORO) operation, a separate transmit RF coil is used to excite the volume with homogenous \mathbf{B}_1 at a desired flip angle. The important goal is to provide homogenous \mathbf{B}_1 such that the sample magnetization over the entire imaging volume is excited to the same flip angle. Thus, a birdcage RF coil is typically used for transmission. For reception, a separate receive RF coil is utilized to act as a sensitive antenna to detect the resulting \mathbf{M}_t . To achieve the highest SNR, a local surface RF coil is chosen for its high sensitivity over a limited volume. One complication with the TORO system architecture is coupling between transmit and receive RF coils. It is desirable to only have the transmit coil resonant only during transmission and the

receive coil only resonant during reception. For this switch-tuned RF system, decoupling of the ^{13}C transmit and receive RF coils was accomplished by rapidly switching the resonant frequency of the birdcage coil after transmission.

1.4 Glioma

A rat glioma model was used in this thesis as a prototypical solid tumour model to evaluate pyruvate-to-lactate conversion measured by ^{13}C MRSI as a biomarker for treatment response and demonstrate pH mapping in tumours. This section contains information regarding background information for glioma, glioma therapy, tumour metabolism and tumour pH.

1.4.1 Background of glioma

Glioma is a type of brain tumour that arises from glial cells. It is the most common primary brain tumour and comprises 80% of all malignant brain tumours. [24] Gliomas are graded between I ~ IV according to World Health Organization (WHO). [25] The grading scale spans Grade I, categorized as a non-proliferating non-malignant tumour to Grade IV considered a highly proliferating malignant tumour. The most common and aggressive malignant glioma is glioblastoma, categorized as WHO grade IV. Glioblastoma has very poor prognosis and a median survival rate of only 12 to 15 months. [26] Severe interventions such as surgical removal and radio/chemotherapy are offered as treatments. Despite these efforts, this cancer inevitably recurs and further undermines the well-being of patients. [27]

1.4.2 Glioma therapy

The most common treatment of glioma is surgical removal of the tumour (when it is accessible) followed by radiotherapy and chemotherapy. For radiotherapy, a total of 60 Gy is delivered locally in 2 Gy fractions over 5 to 6 weeks. [28] Radiotherapy induces double strand breaks of DNA causing cellular death. Surgical resection and conformal radiotherapy is employed to preferentially eliminate tumour and spare healthy brain tissue. This is followed by adjuvant chemotherapy. Typically for glioma, a dose of 150 mg/m^2 of temozolomide (TMZ) is given once daily for 5 days followed by 23 days

without treatment. [28] TMZ is an alkylating agent that damages DNA by methylating a specific site of DNA, which results in cellular death. Highly proliferating cells are vulnerable to TMZ. However, its action is non-specific and its effects are not restricted to tumours limiting its therapeutic window. TMZ also causes adverse side effects such as nausea and vomiting. Other chemotherapeutic drugs such as antiangiogenic agents or growth factor receptor tyrosine kinase inhibitors are also used in combination. [29] Despite these aggressive and multimodal treatments, the median survival rate of patients is increased to only 15 months. Considering the toxicity of these therapies, accurate and prompt knowledge of treatment efficacy is paramount to guide therapeutic choice and improve end-of-life care.

1.4.3 Tumour metabolism

The metabolic profile of tumours change during their progression. As mentioned in “The Hallmarks of Cancer”, tumour metabolism is one of several key therapeutic targets [30]. The most notable change of metabolism exhibited by many tumours is an increased rate of glycolysis and reduction of oxidative phosphorylation compared with other tissue even with the availability of oxygen. This phenomenon was first observed by Dr. Otto Heinrich Warburg and is referred to as the Warburg Effect. [31] In greater detail, the uptake of glucose is increased by glucose transporters in many cancer cells. Glucose is converted into pyruvate by several upregulated enzymes. The resulting pyruvate is converted into lactate and produces oxidized nicotinamide adenine dinucleotide (NAD⁺) from reduced nicotinamide adenine dinucleotide (NADH) by increased lactate dehydrogenase (LDH) activity. [32] Compared to oxidative phosphorylation where pyruvate is metabolized in the Krebs cycle in the mitochondria of cells to produce adenosine triphosphate (ATP), the energy production by glycolysis is very inefficient (measured as ATP production per molecule of glucose). As a result, tumour cells often exhibit increased glucose uptake through increased membrane transport. [33] These traits can be detected by several molecular imaging techniques. Positron emission tomography, PET, using 2-deoxy-2-(¹⁸F)fluoro-D-glucose (¹⁸F-FDG), can quantitatively measure the uptake of glucose in tissue. [34] Highly aggressive tumours such as glioma, exhibit increased ¹⁸F-FDG uptake. [35] As discussed in chapter 1.2.4.1, hyperpolarized ¹³C

pyruvate can also be used to measure metabolic conversion between pyruvate and lactate. In tumours, where increased lactate production is observed, the application of therapy has produced a commensurate decrease in lactate production. [7] Brain tissue is highly metabolic reducing the contrast for brain tumours when assessed by ^{18}F -FDG PET. Quantification of glioma metabolism with ^{13}C pyruvate does not suffer this limitation.

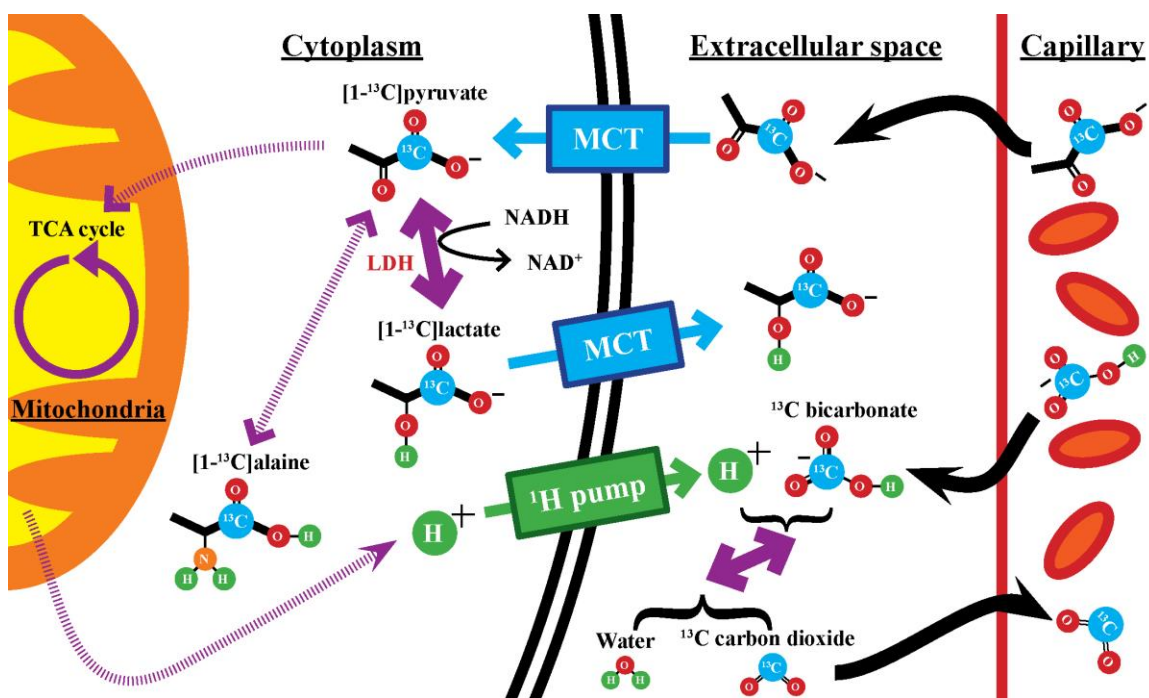


Figure 1-5 Use of hyperpolarized $[1-^{13}\text{C}]$ pyruvate and ^{13}C bicarbonate for quantifying tumour metabolism and tumour pH. $[1-^{13}\text{C}]$ pyruvate and ^{13}C bicarbonate are delivered by the vasculature. $[1-^{13}\text{C}]$ pyruvate is transported into the cytoplasm of tumour (or healthy) cells by monocarboxylate transporter (MCT). Increased LDH activity in tumour cells shifts the chemical equilibrium between pyruvate and lactate, creating a larger pool of endogenous lactate in the cytoplasm. This results in a greater concentration of $[1-^{13}\text{C}]$ lactate relative to $[1-^{13}\text{C}]$ pyruvate in tumour cells compared to healthy cells. Excess protons and acids are pumped out of the tumour into the interstitial space. The pH of the extracellular space is buffered by ^{13}C bicarbonate, which converts the excess protons to water and ^{13}C -labelled carbon dioxide.

1.4.4 Tumour pH

pH is the scale measuring hydrogen ion activity in a given environment. Proteins are often functional only within a limited pH range. [36] Therefore, tissues operate to maintain pH both intracellularly and extracellularly. Within cells, hydrogen ions and metabolic acids are generated, which decrease the intracellular pH (pH_i). To balance this acidic environment, hydrogen ions and cations are pumped out of the cell until the electrochemical gradient of cell is balanced. [37] This results in acidification of the interstitial space due to excessive hydrogen ions. The extracellular pH (pH_e) is maintained largely by the bicarbonate buffer system. Excess hydrogen ions are combined with bicarbonate ions into carbon dioxide and water as shown here:



This process is facilitated by carbonic anhydrase and can be reversed if the surrounding environment becomes too alkaline. Excess carbon dioxide and water are removed by the vascular system. Similarly, within tumours, the pH also needs to be regulated. Since a tumour is highly proliferative, it produces more metabolic acids. [32] To compensate, the tumour often over-expresses transporters to transfer metabolic acids and cations into the extracellular space. In the end, the pH_i of the tumour cell becomes slightly alkaline due to upregulated ion pumping. [37] The pH_e of the tumour becomes acidic and without functional and efficient vascularization, acidification of the extracellular space is increased. This regional hypoxia resulting from insufficient vascularization can intensify the aggressive proliferation of the tumour. [38] Compared to healthy tissues, which exhibit $\text{pH}_e > \text{pH}_i$, tumours often show the opposite behaviour ($\text{pH}_i > \text{pH}_e$). [39] This reversal of the pH gradient is an important a factor in the electrochemical gradient across tumour membrane. Glioma is known to develop a very low pH_e and this pH has been correlated with its invasiveness. [38] Extracellular pH can be measured using hyperpolarized ^{13}C bicarbonate as described in chapter 1.2.4.2. The intracellular pH can be measured using an MRI method known as Chemical Exchange Saturation Transfer (CEST). [40]

1.5 Objectives and hypothesis

The objective of this thesis was to investigate molecular changes in tumour metabolism. Assessment of tumour metabolism during tumour progression could potentially aid in choosing patient-specific therapies. Hyperpolarized ^{13}C imaging is an emerging technique that is capable of non-invasively mapping the distribution of ^{13}C -labelled molecular probes. In this thesis, $[1-^{13}\text{C}]$ pyruvate and ^{13}C bicarbonate were used to assess different aspects of tumour metabolism in a rat model of glioma. We hypothesized that *in vivo* hyperpolarized ^{13}C imaging would be capable of sensitive and prompt assessment of the therapeutic response of solid tumours ($[1-^{13}\text{C}]$ pyruvate) and to detect regional changes in the pH gradient of tumours (^{13}C bicarbonate).

The objective of chapter 1 is to provide the necessary introductory information for chapters 2, 3 and 4. This includes ^1H MRI, hyperpolarized ^{13}C MRSI, RF hardware and glioma biology. In particular, sections 1.1 and 1.2 provide an explanation of the imaging techniques and methods used in later chapters. A complete description was not possible within the limitations of the journal manuscript format. Basic background information required to understand the construction of RF coil in chapter 2 has been provided in section 1.3. Finally, section 1.4 provides important biological aspects of the glioma model that was used in this thesis.

The objective of chapter 2 is to describe the construction and evaluation of a novel switch-tuned $^{13}\text{C} - ^1\text{H}$ RF coil, which was required for this imaging research. Special RF coil technology is required to perform ^{13}C MRSI, in order to provide high sensitivity to the ^{13}C signal and facilitate co-registration between ^1H and ^{13}C imaging data. The design and construction of a switch-tuned $^{13}\text{C} - ^1\text{H}$ RF coil is discussed in chapter 2. Single tuned ^1H and ^{13}C RF coils have also been constructed and evaluated along with switch-tuned $^{13}\text{C} - ^1\text{H}$ RF coil. Improved signal sensitivity using the TORO mode is also explored.

The objective of chapter 3 is to demonstrate the use of hyperpolarized ^{13}C MRSI to assess early therapeutic efficacy in a preclinical tumour model. A high rate of lactate production from pyruvate is correlated with tumour proliferation. Using hyperpolarized $[1-$

^{13}C pyruvate as a probe, its conversion to [$1\text{-}^{13}\text{C}$]lactate was quantified longitudinally in a rat model of glioma. Early tumour response or lack of response to radiotherapy, chemotherapy and combined therapies are compared with the absence of therapy in a longitudinal imaging study using a C6 rat glioma model. Imaging results are validated with histology at experimental endpoint.

The objective of chapter 4 is to longitudinally measure the intracellular/extracellular pH gradient in a rat glioma model. CEST MRI was used for pH_i measurement and hyperpolarized ^{13}C -bicarbonate MRSI used for pH_e measurement. Progression between tumour volume and pH gradient is discussed in chapter 4. Histology (including haematoxylin and eosin, HIF-1 α and Ki-67 staining) is compared with tumour pH gradient maps.

Chapter 5 summarizes the results from the three previous chapters and their contributions towards molecular imaging of tumour metabolism in a rat model of glioma. This chapter also includes future work for further expansion of these studies.

References for Chapter 1

1. Haacke, E.M., et al., *Magnetic Resonance Imaging: Physical Principles and Sequence Design*. 1999: Wiley.
2. Bernstein, M.A., K.F. King, and Z.J. Zhou, *Handbook of MRI pulse sequences*. 2004, Amsterdam ; Boston: Academic Press. xxii,1017 p.
3. Posse, S., et al., *MR spectroscopic imaging: principles and recent advances*. J Magn Reson Imaging, 2013. **37**(6): p. 1301-25.
4. Shiroishi, M.S., et al., *Principles of T2 *-weighted dynamic susceptibility contrast MRI technique in brain tumor imaging*. J Magn Reson Imaging, 2015. **41**(2): p. 296-313.
5. Gunther, U.L., *Dynamic nuclear hyperpolarization in liquids*. Top Curr Chem, 2013. **335**: p. 23-69.
6. Ardenkjaer-Larsen, J.H., et al., *Increase in signal-to-noise ratio of > 10,000 times in liquid-state NMR*. Proc Natl Acad Sci U S A, 2003. **100**(18): p. 10158-63.
7. Brindle, K.M., et al., *Tumor Imaging Using Hyperpolarized C-13 Magnetic Resonance*. Magnetic Resonance in Medicine, 2011. **66**(2): p. 505-519.
8. Coplen, T.B. and Y. Shrestha, *Isotope-abundance variations and atomic weights of selected elements: 2016 (IUPAC Technical Report)*. Pure and Applied Chemistry, 2016. **88**(12): p. 1203-1224.
9. Deboer, W. and T.O. Niinikoski, *Dynamic Proton Polarization in Propanediol Below 0.5 K*. Nuclear Instruments & Methods, 1974. **114**(3): p. 495-498.
10. Nelson, S.J., et al., *Metabolic Imaging of Patients with Prostate Cancer Using Hyperpolarized [1-C-13]Pyruvate*. Science Translational Medicine, 2013. **5**(198).
11. Day, S.E., et al., *Detecting tumor response to treatment using hyperpolarized C-13 magnetic resonance imaging and spectroscopy*. Nature Medicine, 2007. **13**(11): p. 1382-1387.
12. Albers, M.J., et al., *Hyperpolarized 13C lactate, pyruvate, and alanine: noninvasive biomarkers for prostate cancer detection and grading*. Cancer Res, 2008. **68**(20): p. 8607-15.
13. Witney, T.H., et al., *Detecting treatment response in a model of human breast adenocarcinoma using hyperpolarised [1-13C]pyruvate and [1,4-13C2]fumarate*. Br J Cancer, 2010. **103**(9): p. 1400-6.

14. Golman, K., et al., *Cardiac metabolism measured noninvasively by hyperpolarized C-13 MRI*. *Magnetic Resonance in Medicine*, 2008. **59**(5): p. 1005-1013.
15. Gatenby, R.A. and R.J. Gillies, *Why do cancers have high aerobic glycolysis?* *Nature Reviews Cancer*, 2004. **4**(11): p. 891-899.
16. Chattergoon, N., et al., *Field dependence of T1 for hyperpolarized [1-13C]pyruvate*. *Contrast Media Mol Imaging*, 2013. **8**(1): p. 57-62.
17. Gallagher, F.A., et al., *Magnetic resonance imaging of pH in vivo using hyperpolarized (13)C-labelled bicarbonate*. *Nature*, 2008. **453**(7197): p. 940-U73.
18. Martinez-Santesteban, F.M., et al., *T1 nuclear magnetic relaxation dispersion of hyperpolarized sodium and cesium hydrogencarbonate-13 C*. *NMR Biomed*, 2017.
19. Altermatt, H.J., J.O. Gebbers, and J.A. Laissue, *Heavy water delays growth of human carcinoma in nude mice*. *Cancer*, 1988. **62**(3): p. 462-6.
20. Keeler, J., *Understanding NMR spectroscopy*. 2nd ed. 2010, Chichester, U.K.: John Wiley and Sons. xiii, 511 p.
21. Schulte, R.F., et al., *Saturation-recovery metabolic-exchange rate imaging with hyperpolarized [1-13C] pyruvate using spectral-spatial excitation*. *Magn Reson Med*, 2013. **69**(5): p. 1209-16.
22. Mispelter, J., M. Lupu, and A. Briguet, *NMR Probeheads for Biophysical And Biomedical Experiments: Theoretical Principles And Practical Guidelines*. 2006: Imperial College Press.
23. Jin, J.-M., *Electromagnetic analysis and design in magnetic resonance imaging*. Biomedical engineering series. 1998, Boca Raton: CRC Press. xiv, 282 p.
24. Omuro, A. and L.M. DeAngelis, *Glioblastoma and other malignant gliomas: a clinical review*. *JAMA*, 2013. **310**(17): p. 1842-50.
25. Komori, T., H. Sasaki, and K. Yoshida, *[Revised WHO Classification of Tumours of the Central Nervous System: Summary of the Revision and Perspective]*. No Shinkei Geka, 2016. **44**(8): p. 625-35.
26. Legler, J.M., et al., *Cancer surveillance series [corrected]: brain and other central nervous system cancers: recent trends in incidence and mortality*. *J Natl Cancer Inst*, 1999. **91**(16): p. 1382-90.
27. Davis, M.E., *Glioblastoma: Overview of Disease and Treatment*. *Clin J Oncol Nurs*, 2016. **20**(5): p. S2-8.

28. Mason, W.P., et al., *Canadian recommendations for the treatment of glioblastoma multiforme*. *Curr Oncol*, 2007. **14**(3): p. 110-7.
29. Minniti, G., et al., *Chemotherapy for glioblastoma: current treatment and future perspectives for cytotoxic and targeted agents*. *Anticancer Res*, 2009. **29**(12): p. 5171-84.
30. Hanahan, D. and R.A. Weinberg, *Hallmarks of Cancer: The Next Generation*. *Cell*, 2011. **144**(5): p. 646-674.
31. Warburg, O., F. Wind, and E. Negelein, *The Metabolism of Tumors in the Body*. *J Gen Physiol*, 1927. **8**(6): p. 519-30.
32. Kroemer, G. and J. Pouyssegur, *Tumor cell metabolism: cancer's Achilles' heel*. *Cancer Cell*, 2008. **13**(6): p. 472-82.
33. Galeffi, F. and D.A. Turner, *Exploiting metabolic differences in glioma therapy*. *Curr Drug Discov Technol*, 2012. **9**(4): p. 280-93.
34. Gambhir, S.S., *Molecular imaging of cancer with positron emission tomography*. *Nature Reviews Cancer*, 2002. **2**(9): p. 683-693.
35. Weber, W.A., N. Avril, and M. Schwaiger, *Relevance of positron emission tomography (PET) in oncology*. *Strahlentherapie Und Onkologie*, 1999. **175**(8): p. 356-373.
36. Alberts, B., et al., *Molecular Biology of the Cell 4th Edition: International Student Edition*. 2002: Taylor & Francis Group.
37. Swietach, P., et al., *The chemistry, physiology and pathology of pH in cancer*. *Philos Trans R Soc Lond B Biol Sci*, 2014. **369**(1638): p. 20130099.
38. Webb, B.A., et al., *Dysregulated pH: a perfect storm for cancer progression*. *Nat Rev Cancer*, 2011. **11**(9): p. 671-7.
39. Gerweck, L.E. and K. Seetharaman, *Cellular pH gradient in tumor versus normal tissue: potential exploitation for the treatment of cancer*. *Cancer Res*, 1996. **56**(6): p. 1194-8.
40. McVicar, N., et al., *Quantitative tissue pH measurement during cerebral ischemia using amine and amide concentration-independent detection (AACID) with MRI*. *J Cereb Blood Flow Metab*, 2014. **34**(4): p. 690-8.

Chapter 2

2 Construction and evaluation of a switch-tuned ^{13}C – ^1H birdcage radiofrequency coil for imaging the metabolism of hyperpolarized ^{13}C -enriched compounds

*Heeseung Lim, Kundan Thind, Francisco M. Martinez-Santesteban,
and Timothy J. Scholl*

Journal of Magnetic Resonance Imaging. September 2013. DOI: 10.1002/jmri.24458

2.1 Introduction

The development of hyperpolarization technology to increase the magnetization of ^{13}C -enriched endogenous compounds [1, 2] has enabled their use as contrast agents with MRI. Cellular metabolism, which is often altered in diseases dictates the rate of uptake of cellular substrates and their conversion for individual metabolic needs of the cell [3]. ^{13}C imaging and spectroscopy with MR can readily measure those rates and thereby quantify cellular metabolism [4-6]. The inherent physical properties of the ^{13}C -isotope such as its limited natural abundance (1.1%) and its low gyromagnetic ratio (the ^{13}C gyromagnetic ratio is four times less than that of ^1H) results in a significantly lower MR signal [7]. The use of endogenous compounds with highly enriched ^{13}C compounds as metabolic probes can overcome the natural abundance problem to a large extent; however, more importantly, ^{13}C substrates can be highly magnetized (hyperpolarized) by dynamic nuclear polarization (DNP) *in vitro* and then used as injectable agents to probe *in vivo* metabolism [2].

Regional and time-resolved *in vivo* metabolic information can be determined using hyperpolarized ^{13}C imaging and spectroscopy. Despite signal enhancement through hyperpolarization, this information is limited in spatial or temporal resolution by the amount of signal available due to the transient nature of the hyperpolarized state. Metabolic information can be co-registered with tissue morphology obtained at higher resolution using conventional proton MRI. The use of dual or switch-tuned RF hardware that can image both nuclei without a change of RF coils or repositioning of the animal

model simplifies the co-registration of metabolism and anatomy and makes this registration essentially exact.

This study describes the construction and performance of a switch-tuned ^{13}C - ^1H birdcage radiofrequency (RF) coil that can be rapidly switched between anatomical imaging mode (^1H) and metabolic imaging mode (^{13}C) by use of PIN (PN junction with isolation region) diodes. To determine the utility of the switch-tuned ^{13}C - ^1H RF coil, individual single-tuned ^1H and ^{13}C birdcage RF coils with identical dimensions were constructed for a detailed comparison of imaging performance. A ^{13}C receive-only surface RF coil was integrated with the switch-tuned ^{13}C - ^1H RF coil exploiting its fast frequency switching capability to enable transmit-only, receive-only (TORO) operation for ^{13}C spectroscopy with improved sensitivity. Lastly *in vivo* ^{13}C spectroscopy and ^1H imaging were performed using TORO operation to demonstrate the practicality of this hardware strategy.

2.2 Methods

2.2.1 Coil Geometry

All RF coils were constructed with the same physical dimensions and materials for accurate comparison of imaging performance gauged by the observed signal-to-noise ratio (SNR). The coil dimensions were chosen to accommodate an animal model up to the size of a small rabbit. Each coil consisted of a birdcage resonator and a shield. The resonator was constructed on a cylindrical acrylic tube, 88.9 mm in outer diameter (OD) by 266.7 mm in length. The thickness of the coil form was 3.2 mm. The RF shield (356 mm long, 165 mm OD) was constructed on a separate cylindrical acrylic tube and two nylon rings were used to concentrically locate it with respect to the resonator. These rings also served to fasten the coil assembly to a rail system that was used to position the hardware in the scanner.

2.2.2 Resonator Circuit

Three eight-rung birdcage resonators were constructed: a single-tuned ^{13}C (32.115 MHz at 3 Tesla [T]) low-pass resonator, a single-tuned ^1H (127.728 MHz at 3T) band-pass

resonator and a switch-tunable combined ^{13}C low-pass and ^1H band-pass resonator. Self-adhering, copper foil tape (12.7-mm-wide by 0.07-mm-thick) was fitted into grooves, which were accurately machined into the acrylic forms and the copper conductors were soldered together to form the basic eight-rung resonator geometry. The length of each rung was 101.6 mm and the diameter of the end rings was 87.3 mm. High-Q capacitors ($Q > 2000$, Working voltage: 500 V, American Technical Ceramics) were used to resonate the coil. The capacitances were initially determined to a few percent by software (Birdcage Builder Version 1.0 Software, College of Medicine, Penn State Hershey) and later refined as resonators were fine-tuned [8]. The switch-tuned ^{13}C - ^1H resonator included PIN diodes (Micro-semi UM9415) in parallel with each of the capacitors on the end rings. The PIN diodes were biased through a network of 10-mH RF chokes (Bourns 4612-RC).

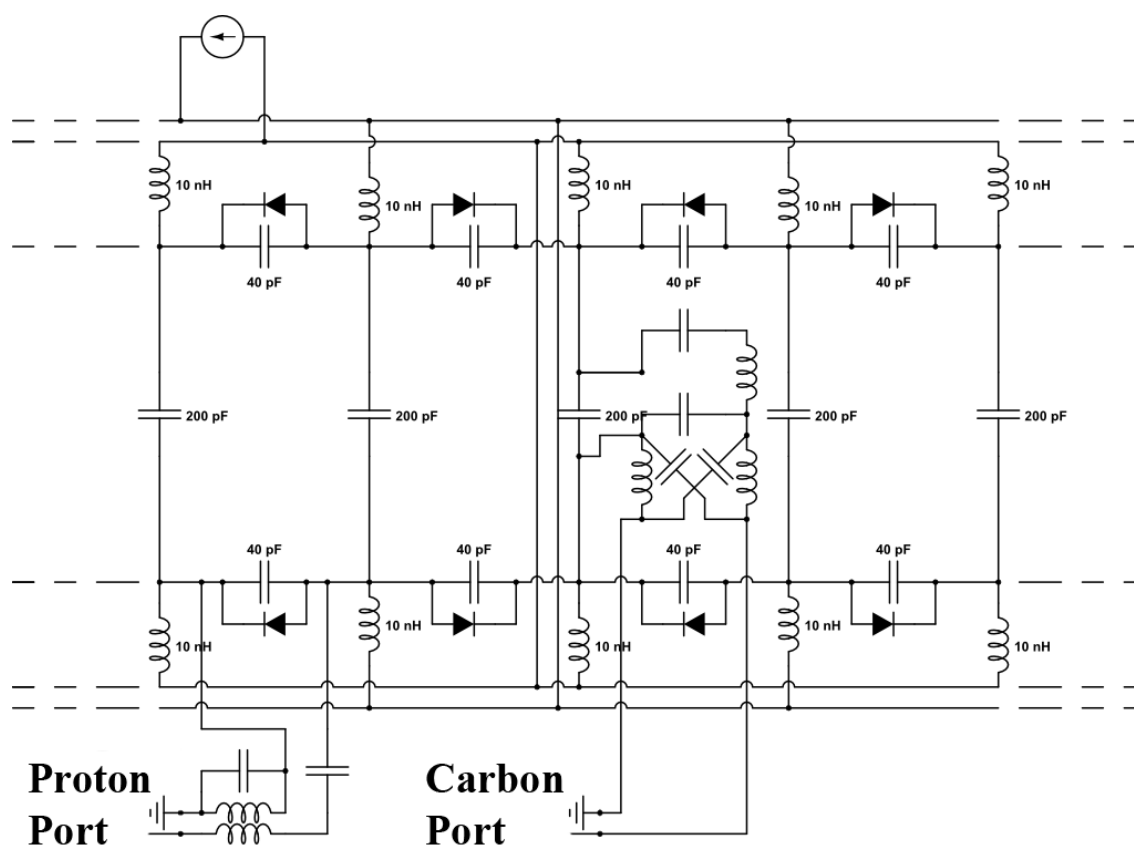


Figure 2-1 Simplified circuit diagram of the switch-tuned ^{13}C - ^1H RF coil. The capacitors on the end rings and rungs had slight variations in value. The switch-tuned ^{13}C - ^1H RF coil had a total of four RF connections, a pair for each frequency of operation.

A simplified circuit diagram of the switch-tuned ^{13}C - ^1H RF coil is shown in Figure 2-1. The RF circuitry consisted of eight rungs and four matching networks. Each frequency matching network was 90° apart in phase from each other. The birdcage coil is well documented in the literature [9]. An eight-rung birdcage RF coil provided a homogenous B_1 field while minimizing complexity of construction [10]. The single-tuned ^{13}C coil is a low-pass birdcage design that uses lower-value capacitors. The single-tuned ^1H coil and switch-tuned ^{13}C - ^1H RF coil used a band-pass birdcage circuit. The band-pass or hybrid birdcage circuit is a combination of low-pass and high-pass birdcage circuitry, which conveniently lends itself to a switching scheme between these two resonator geometries. Switch-tuning was accomplished by controlling the RF impedance of the PIN diodes

using a DC bias. The method of switch-tuning resonator frequencies for different nuclei using PIN diodes had been previously described for two relatively closely spaced Larmor frequencies 127.728 MHz (^1H at 3T) and 97.302 MHz (^3He at 3T) using band-pass geometry [11]. In that RF system, the relatively small frequency shift was achieved without a complete change of the resonator geometry.

Bias current to the PIN diodes was DC-choked to confine RF current to the resonator. Careful use of twisted-pair cable for bias currents and use of RF chokes suppressed any RF noise coming from the bias supply or from pickup along the cables. Impedance matching circuits and baluns were chosen to use convenient values of capacitance and inductance. All coils were first tuned while loaded with an appropriate phantom in their shields and then slightly re-tuned at the scanner for optimum signal reception.

2.2.3 Matching Circuitry Baluns

Separate impedance matching circuits and baluns (balanced→unbalanced) were used for each frequency. Each coil was matched to 50 Ω and “unbalanced” at a particular frequency to reduce RF current in the coaxial shield [10]. The ^{13}C frequency was matched with a π matching circuit and unbalanced with an LC balun. The ^1H frequency was matched with a capacitive matching circuit and unbalanced with a cable-trap balun.

2.2.4 Shield

The shield was comprised of strips of overlapping aluminum tape. Continuous strips of self-adhering tape (330 mm long by 25.4 mm wide by 0.13 mm thick) were oriented on the cylindrical form in a direction along the axis of rotation. Each strip of aluminum tape overlapped the previous layer in the circumferential direction by 6 mm and was separated with a layer of insulating Kapton tape.

2.2.5 RF Coil and Animal Support

The RF coils and animal tray were supported by a pair of non-conducting glass-fiber reinforced plastic rails. These rails were located by plastic struts fixed to a platform that was designed to fasten onto the patient bed of a GE Healthcare MR750 3T MRI scanner (GE Healthcare, Waukesha, WI). All the components of the rail system and platform are

MR compatible. A custom-built animal bed could be slid along the rail system and locked at a specific longitudinal position. The animal bed provided delivery and recovery of anesthesia through a nose cone and was heated by water (40°C) circulating through internal channels to keep the animal warm under anesthesia during imaging experiments.

2.2.6 Surface Coil

A rectangular (91.0 mm by 90.0 mm) ^{13}C surface RF coil was used for signal reception only. It was constructed on a curved acrylic form with an OD of 56.3 mm. The circuit was actively detuned during RF transmission using a DC bias applied to a PIN diode. Capacitive matching was used to match the coil to 50 Ω and a cable trap balun was used to eliminate shield currents.

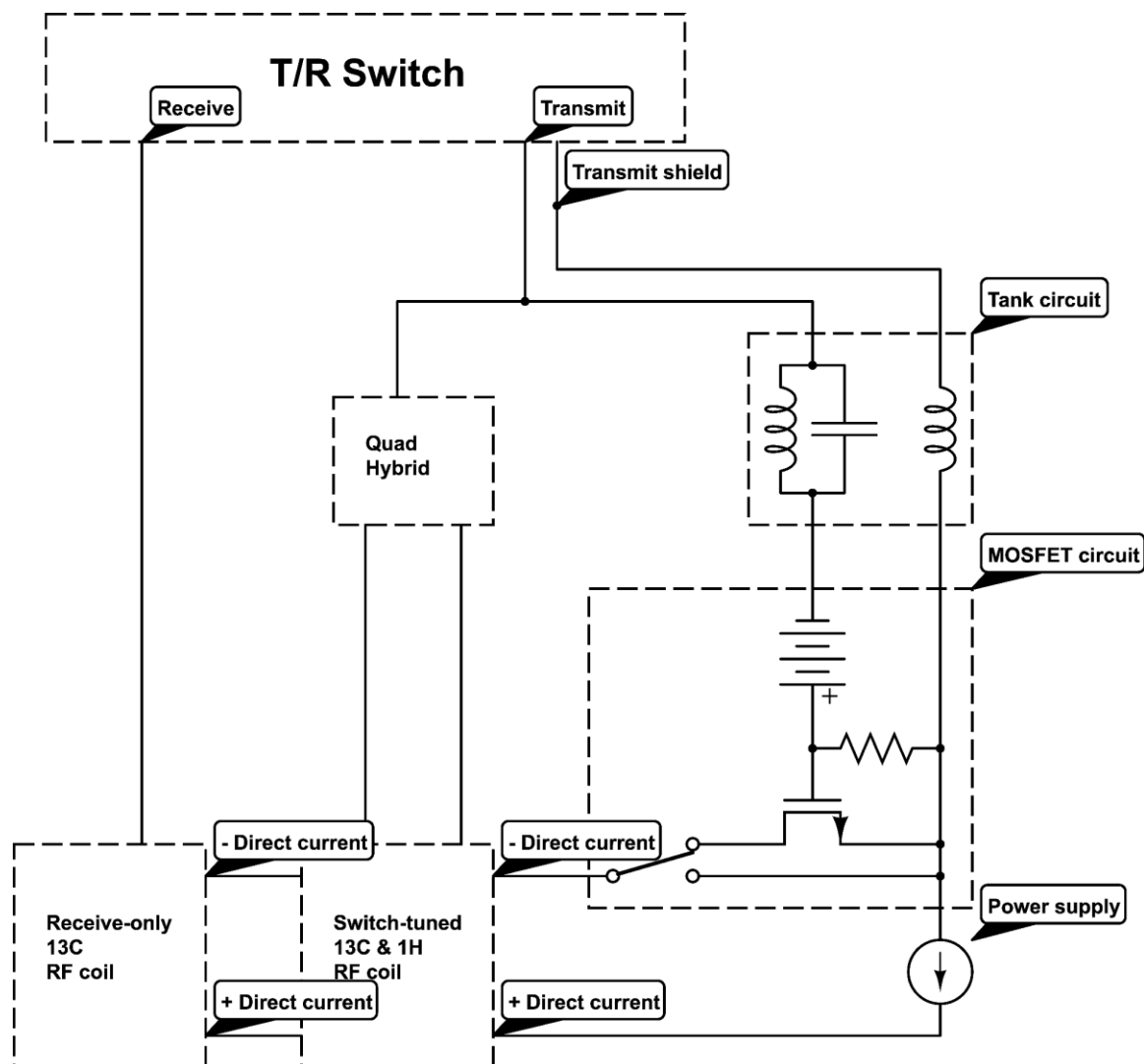


Figure 2-2 Detailed schematic of the RF configuration for transmit-only, receive-only operation of the switch-tuned ^{13}C - ^1H RF coil. The T/R switch provided an RF transmit pulse including a DC offset bias during transmission. The RF pulse was applied to the ^{13}C quadrature hybrid circuit, which drives the switch-tuned ^{13}C - ^1H RF coil in quadrature operation. In a parallel circuit, a tank circuit filtered AC current from the transmit pulse. The resulting DC bias from the transmit pulse (present only during RF transmission) was used to trigger the MOSFET circuit to supply DC current to bias the PIN diodes of the RF coils.

2.2.7 Power Supply and Switching Circuit

Active frequency switching and detuning of the RF coils during TORO operation was accomplished by application of DC biases to the PIN diodes. A metal-oxide-semiconductor field-effect transistor (MOSFET) circuit (see Figure 2-2) was used to control current from an Agilent U8002A power supply. During transmit/ receive (T/R) operation of the switch-tuned RF hardware in ^1H mode, the PIN diodes were reverse-biased to prevent the RF current from biasing the end-ring diodes and detuning the resonator.

2.2.8 Imaging Phantom

Two imaging phantoms were used to calibrate and test the coils. A rat-sized phantom was constructed using a cylindrical container, 57.5 mm in diameter and 127.0 mm in length with two separate coaxial compartments. The inner compartment held three glass vials containing different ^{13}C -enriched compounds: $[1-^{13}\text{C}]$ sodium acetate, ^{13}C -urea, and $[1-^{13}\text{C}]$ pyruvate. The outer compartment was filled with 0.15-mmol/L MnCl_2 in 0.9% saline solution for coil loading. This phantom was designed to roughly mimic a rat model after ^{13}C metabolite injection. The second phantom consisted of a 5-mL plastic vial, containing 7-mol/L $[1-^{13}\text{C}]$ sodium acetate. Gd^+ contrast agent was added to the sodium acetate phantom to achieve a T_1 of less than one second.

2.2.9 Coil Calibration

All the coils have been interfaced to the GE 3T MRI scanner. The $^{13}\text{C}/^1\text{H}$ rat phantom was used to calibrate ^1H imaging and the ^{13}C sodium acetate phantom was used to calibrate ^{13}C imaging and spectroscopy. Calibration of tip angles was determined by adjusting the transmit gain to obtain a 90° pulse with the phantoms.

2.2.10 Phantom Imaging

For ^1H images, two-dimensional (2D) coronal images of the phantoms were acquired with a 128-mm \times 128-mm field-of-view (FOV) and 40-mm slice thickness resulting in a 0.5-mm-per-voxel in-plane resolution. A fast gradient-recalled echo (FGRE) sequence was used with the following parameters: repetition time (TR) = 34 ms, echo time (TE) =

4.1 ms, flip angle, $\alpha = 90^\circ$ and 16 averages. For ^{13}C imaging, the in-plane resolution was reduced to 1 millimeter over the same field of view (FOV) and with the same slice thickness as the coronal ^1H images. Images of the phantoms were acquired using a broadband FGRE (bbFGRE) sequence with $\text{TR} = 34$ ms, $\text{TE} = 2.3$ ms, $\alpha = 90^\circ$ and 64 averages. Image SNR was calculated with MATLAB code using the dual acquisition method [12]. In addition, ^{13}C spectra of the sodium acetate phantom were acquired using a free induction decay chemical shift imaging (FID-CSI) pulse sequence with $\text{TR} = 1000$ ms, $\alpha = 90^\circ$ and 64 averages. ^{13}C spectra SNR were analyzed using SAGE 7.7 (GE Healthcare, Waukesha, WI, USA).

2.2.11 B_1 Mapping

Using the $^{13}\text{C}/^1\text{H}$ phantom, a 3D B_1 map with 2-mm isotropic resolution was obtained with a noninverting double-angle Look-Locker pulse sequence [13] ($\text{TR} = 3.7$ ms, 16 echo trains, nominal flip angle, $\alpha = 6^\circ$ and 8 different TIs per angle). B_1 maps were reconstructed from raw data using dedicated software written in MATLAB (Mathworks, Natick, MA).

2.2.12 Hyperpolarization

Trityl radical (OX063, GE Healthcare) was added at 15 mmol/L to ^{13}C -enriched (99%) $[1-^{13}\text{C}]$ pyruvic acid (Cambridge Isotope Laboratories, Andover, MA). Approximately 25 mL of the mixture was hyperpolarized at 1.4 K and 3.35T using a HyperSense DNP apparatus (Oxford Instruments Abingdon, Oxfordshire, UK). After approximately 45 min of polarization, the hyperpolarized sample was rapidly thawed and diluted with a buffering solution producing an 80-mmol/L $[1-^{13}\text{C}]$ pyruvate solution buffered to a pH of ~ 7.6 with a liquid-state polarization of $\sim 15\%$ [14]. Approximately 3 mL of the $[1-^{13}\text{C}]$ pyruvate solution was gathered in a syringe and rapidly transferred to the MRI for imaging.

2.2.13 Animal Imaging

Male Wistar rats were used for the *in vivo* experiments. One million C6 rat glioma cells were implanted in the rat brain using a stereotactic frame. During the imaging session, the

rat was anesthetized using isoflurane and warmed by a heated animal bed to maintain body temperature. Rat breathing and temperature were continuously recorded using a small animal monitoring and gating system (S.A. instruments, Stony Brook, NY). Axial T_2 -weighted ^1H images of the rat brain were initially acquired using a fast-spin echo sequence with a 80-mm by 80-mm FOV, 0.3-mm isotropic resolution, 3-mm slice thickness, TR = 4000 ms, TE = 85 ms, 16-echo trains and 9 averages. The buffered hyperpolarized [$1\text{-}^{13}\text{C}$]pyruvate solution was injected through the tail vein catheter in a single 12-s bolus injection. Twenty-five seconds after the start of injection, ^{13}C spectra (axial plane, 12 by 12 spectral imaging matrix, TR = 80 ms, bandwidth = 5 kHz, 2048 pts, $\alpha = 10^\circ$) were acquired using a 2D FID-CSI pulse sequence with a 60-mm by 60-mm FOV, slice thickness \approx tumour extent. All animal procedures were approved by the University Council on Animal Care, Animal Use Subcommittee.

Table 2-1 Network analyzer (Agilent E5061B) measurements of RF coil performance*

	Single-Tuned Coil		Switch-tuned Coil	
	^1H	^{13}C	^1H	^{13}C
Nucleus	^1H	^{13}C	^1H	^{13}C
Resonant frequency (MHz)†	127.74	32.15	127.70	32.09
Reflected signal (dB) †	-44.0	-37.5	-40.6	-40.9
Quality factor	200	183	109	45
Isolation (dB)	-22.8	-42.5	-20.9	-44.0

* All RF coils were preloaded with the animal tray and a $^{13}\text{C}/^1\text{H}$ phantom. Resonant frequency, reflected signal and isolation were measured using a 5-MHz frequency window. The RF coil quality factor was measured with the network analyzer using separate transmitting and receiving RF coils placed outside and inside (respectively) of the single- and switch-tuned ^{13}C - ^1H RF coils.

† Averaged value for both channels.

2.3 Results

2.3.1 Initial Coil performance

Benchtop measurements of the coil performance are shown in Table 2-1. All coils were preloaded with the animal tray and $^{13}\text{C}/^1\text{H}$ phantom. The resonant frequencies were within 30 kHz of nominal values at 3T. Quality factors were systematically lower for the switch-tuned $^{13}\text{C} - ^1\text{H}$ RF coil compared with the single-tuned RF coils (for proton 109 vs. 200, for carbon 45 vs. 183). Isolation between quadrature channels was very similar for the switch-tuned $^{13}\text{C} - ^1\text{H}$ RF coil and single-tuned RF coils, but ^{13}C isolation was much greater than that observed for ^1H . ^{13}C transmit power for the switch-tuned $^{13}\text{C} - ^1\text{H}$ RF coil was higher than the single-tuned ^{13}C RF coil.

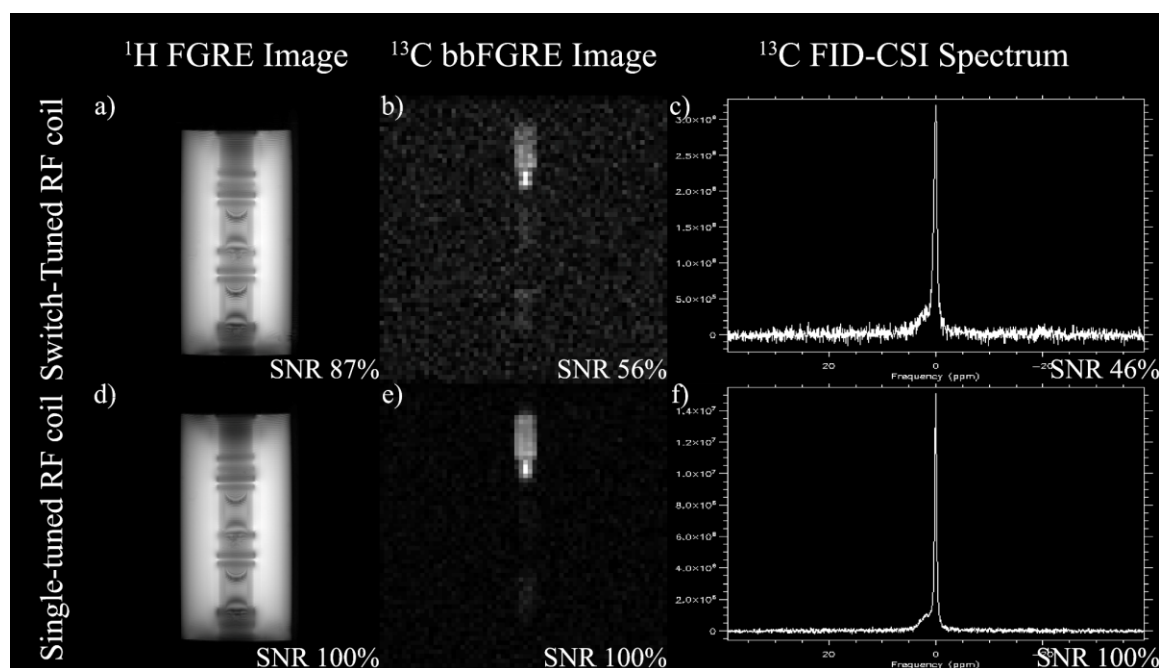


Figure 2-3 ^1H (^1H FGRE) and ^{13}C (^{13}C bbFGRE) images of a rat-sized $^{13}\text{C}/^1\text{H}$ phantom were acquired with single- and switch-tuned $^{13}\text{C} - ^1\text{H}$ RF coils for SNR comparison. c, f: ^{13}C spectra (^{13}C FID-CSI Spectrum) of a thermally polarized $[1-^{13}\text{C}]$ sodium acetate phantom were also acquired using both RF coils. The percentage SNR for the switch-tuned $^{13}\text{C} - ^1\text{H}$ RF coil was with respect to the single-tuned coil for either ^1H or ^{13}C nuclei.

2.3.2 SNR Comparison Using Phantoms

Images of phantoms acquired from the three coils are shown in Figures 2-3 and 2-4. For ^1H operation, the image SNR observed from the switch-tuned ^{13}C - ^1H RF coil was 87% that of the single-tuned ^1H RF coil. For ^{13}C operation, the SNR observed using the switch-tuned ^{13}C - ^1H RF coil was 56% that of the single-tuned ^{13}C RF coil. Operation of the switch-tuned ^{13}C - ^1H RF coil in TORO mode with the ^{13}C surface receive coil showed the highest SNR determined from ^{13}C images of our phantoms. The resulting image SNR was increased by a factor of 2.35 for TORO operation compared with single-tuned ^{13}C T/R operation. Additional SNR comparisons from ^{13}C spectra are shown in Figure 2-3c and f. For ^{13}C spectroscopy, the SNR measured using the switch-tuned ^{13}C - ^1H RF coil (T/R operation) was 46% of that observed from the single-tuned ^{13}C RF coil.

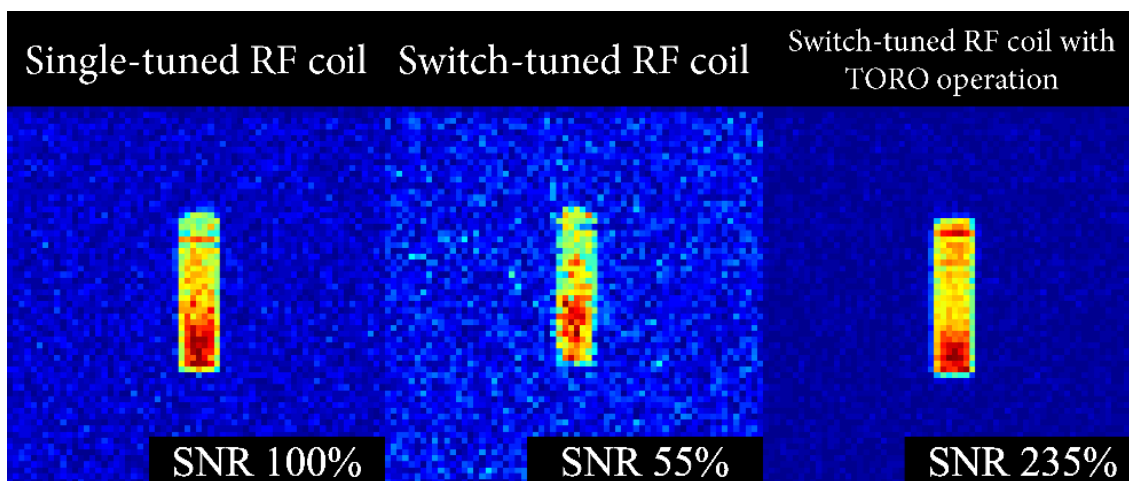


Figure 2-4 Comparison of ^{13}C images with a thermally polarized $[1-^{13}\text{C}]$ sodium acetate phantom acquired using three different RF coils. SNR measurements were normalized to 100% for the single-tuned ^{13}C RF coil.

2.3.3 B_1 Homogeneity

Figure 2-5 illustrates a T_1 -weighted ^1H image, B_1 map and its respective B_1 profile. The mean observed flip angle was 5.66° with standard deviation of 0.4327 for a nominal value of 6° . The B_1 profile revealed only a small amount of Gibbs ringing and RF inhomogeneity over the entire volume of the phantom.

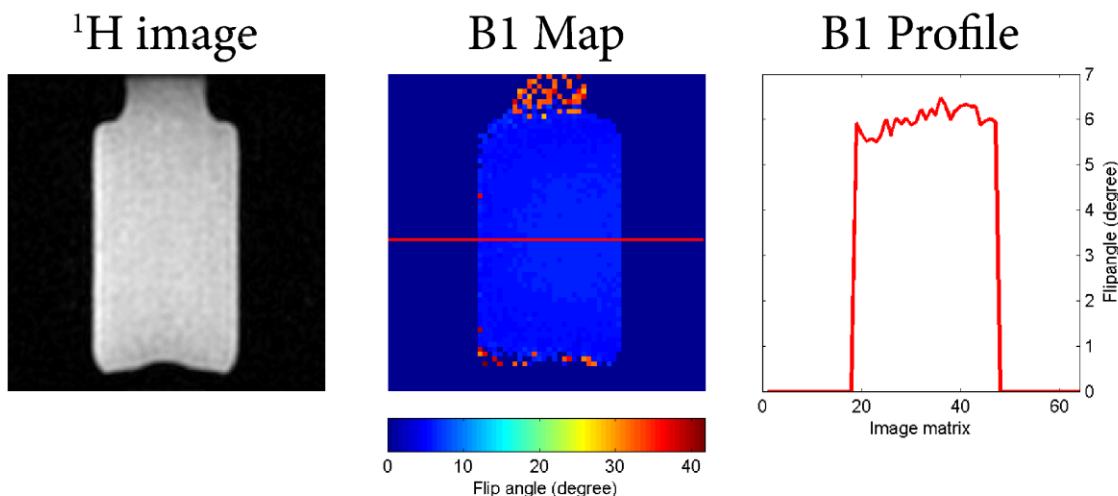


Figure 2-5 B_1 map obtained from the switch-tuned ^{13}C - ^1H RF coil with a phantom (shown at left). Nominal flip angle, α was 6° . The B_1 profile was acquired axially through the phantom at the red line shown on the B_1 map.

2.3.4 *In Vivo* Imaging

A summed spectrum from individual rat brain voxels is shown Figure 2-6a. Individual ^{13}C -spectra overlaid on a T_2 -weighted ^1H image of a rat brain glioma are shown in Figure 2-6b. These spectra contained five relevant spectral components (numbered 1 to 5 from left to right); lactate, pyruvate hydrate, alanine, pyruvate, and bicarbonate. Spectral quantification and image registration was carried out using SAGE 7.7. The boundary of the tumour region was highlighted in red and voxels containing tumour exhibit higher lactate to pyruvate ratio (Lac/Pyr) than healthy tissue voxels.

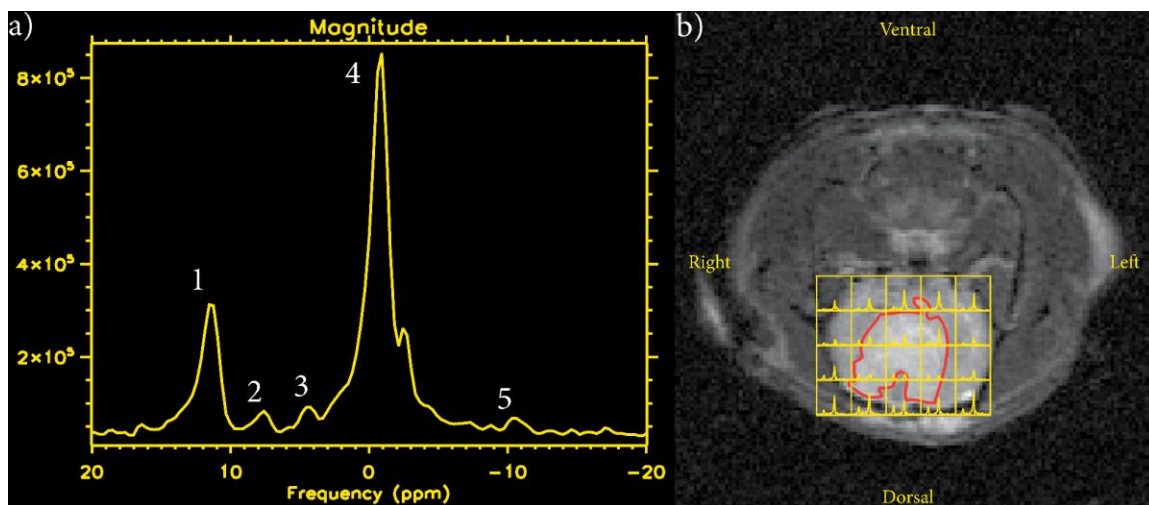


Figure 2-6 Summed ^{13}C spectrum (left) and individual ^{13}C spectra (right) overlaid on a T_2 -weighted ^1H image of a rat's head. a) Relevant spectral peaks labeled 1 through 5 (summed from individual spectra at right) were respectively: lactate, pyruvate hydrate, alanine, pyruvate and bicarbonate. b) A brain tumour was outlined in red. Notice the elevated lactate-to-pyruvate ratio in tumour voxels compared with healthy brain tissue.

2.4 Discussion

All three birdcage coils were geometrically identical and share common circuit components and construction methods that had been optimized for 50Ω impedance. Baluns were added to each matching network to eliminate RF current in the coaxial shields and prevent unwanted common mode currents. Suitable biasing of the diodes produced a switchable capability that is used to rapidly alter the resonator geometry from band-pass configuration (^1H) to low-pass configuration (^{13}C). When the switch-tuned ^{13}C - ^1H RF coil was forward biased, PIN diodes on rings of the band-pass birdcage resonator presented a low-impedance path to RF, effectively eliminating the ring capacitors resulting in a low-pass RF coil that resonates at the ^{13}C Larmor frequency. Conversely, when the switch-tuned ^{13}C - ^1H RF coil was reverse biased (or no DC is applied), the intrinsic capacitance of the PIN diodes in parallel with the ring capacitors, produced a band-pass birdcage resonator at the ^1H frequency.

Benchtop measurements of the quality factor for each coil were obtained as an assessment of coil sensitivity [10]. Reflected signal strength from the RF coil provided a secondary determination of coil performance, assessing coil matching. In initial coil performance testing, the reflected signal strength did not vary much from coil to coil. Yet, when the quality factor was considered, the switch-tuned ^{13}C - ^1H RF coil has poorer performance than single-tuned RF coils for both nuclei. This translated to reduced SNR during imaging.

There were a few factors that contribute to reduction in quality factor of the switch-tuned ^{13}C - ^1H RF coil. Use of PIN diodes could cause dissipation of the RF energy stored in the resonator circuit. During forward biasing, the RF resistance of the diodes was low but not negligible. When reversed biased, a PIN diode operated as a low-Q capacitor in parallel with the ring capacitors. The junction capacitance of the PIN diodes was nominally 4 pF, which is approximately 10% of the capacitance of the ring capacitors. The addition of bias lines and RF chokes may also reduce the efficiency through imperfect RF blocking. Increased complexity of the resonator due to the addition of extra components for switch-tuning could lead to asymmetries in the resonator circuit that are difficult to correct.

Individual PIN diodes were forward biased with a current of 0.375 A. With this bias current, the nominal resistance of the PIN diodes at 32.1 MHz was measured to be 0.5 Ω . Most of the power supplied by the bias power supply was dissipated in the RF chokes which have a DC resistance of 1.5 Ω . This resulted in a small amount of heating of the RF coil structure during ^{13}C imaging. In practical use, the coil was largely operated in ^1H mode and this heating was insignificant considering the proximity of the heated animal bed inside the RF coil.

Image SNR and spectral SNR were compared between coils. Based on benchtop measurements, reduced SNR for both frequencies was expected. Quality factors of the switch-tuned ^{13}C - ^1H RF coil were lower than those measured for the corresponding single-tuned RF coil. For proton imaging, benchtop measurements of the Quality factor showed a 46% reduction for the switch-tuned ^{13}C - ^1H RF coil compared with its single-

tuned RF coil. Comparisons of proton SNR between these coils yielded a loss of 13% for the switch-tuned configuration. For comparisons at the ^{13}C frequency, the Quality factor of the switch-tuned ^{13}C - ^1H RF coil was only 25% that of the single frequency coil resulting in a larger reduction of imaging SNR. An SNR loss of 45% for the switch-tuned ^{13}C channel was observed compared with the ^{13}C single-tuned RF coil. Coil efficiencies were expected to drop for the switch-tuned ^{13}C - ^1H RF coil due to the added losses of extra necessary circuit components.

Modifications to the switch-tuned ^{13}C - ^1H RF coil were investigated to improve SNR. RF chokes with different inductances were investigated; however, these changes did not affect the ^{13}C SNR. No significant SNR improvement was noticed by increasing the DC bias current beyond the typical value that was required for ^{13}C operation. It was interesting that it is possible to fine-tune the matching of ^{13}C coils using the DC biasing current. The exact mechanism was unknown, but it was likely linked to small corresponding changes in the PIN diode resistance. This characteristic is also observed when the coil is reverse-biased to ^1H mode but the amount of fine-tuning of the ^1H frequency during reverse biasing is not very significant in comparison to that achievable with variations of forward bias current.

B_1 homogeneity was another important factor for an RF coil. Application of uniform RF energy across a sample is essential for some RF pulse sequences [10] and important for quantification of the spectroscopic data. For a coil possessing an inhomogeneous B_1 field, an RF pulse would excite a sample with a non-uniform flip angle. The switch-tuned ^{13}C - ^1H RF coil displayed a homogeneous B_1 field for the proton channel across a large field of view. The measured flip angle was very close to the expected value of 6° with a small measurement standard deviation. The B_1 profile demonstrated a small amount of Gibbs ringing artifact at the edge of phantom boundary. Although not measured in this work, it would be expected that the ^{13}C B_1 field was similar to that of the proton [15].

Detailed information about TORO operation of RF hardware had been previously described [16]. TORO operation takes advantage of the highly sensitive localized ^{13}C surface RF coil and homogeneous transmission field. The ^{13}C surface RF coil and switch-

tuned ^{13}C - ^1H RF coil were precisely tuned and matched with the position of the ^{13}C surface RF coil fixed at the center of the birdcage coil with a suitable loading phantom. During TORO operation, transmit and receive RF coils must be alternately tuned/detuned during transmit and receive phases. This was accomplished by application of a DC bias current to PIN diodes in the RF hardware circuitry. For imaging, a DC bias current was applied during RF transmission, which switches the ^{13}C - ^1H birdcage RF coil to resonance at the ^{13}C frequency and simultaneously detunes the surface RF coil. After transmission, the absence of this bias shifted the resonant frequency of the birdcage coil to the proton frequency. This effectively decoupled the birdcage and ^{13}C surface RF coils and enabled reception of the ^{13}C surface RF coil at the ^{13}C frequency. For ^1H imaging, the small ^{13}C surface RF coil did not couple significantly to the birdcage resonator operating at the ^1H frequency during either transmission or reception. Therefore, no other decoupling circuitry was required. Bias current provided by the MRI scanner was limited and not sufficient to bias all the required PIN diodes. For this work, the DC bias from the scanner was used to control a fast MOSFET switching circuit that modulated the current from an auxiliary DC power supply, effectively increasing the available bias current. In theory, TORO operation could also be implemented at the ^1H frequency with an appropriate surface RF coil but this was not undertaken for this work.

To illustrate the capability of the switch-tuned ^{13}C - ^1H RF coil, an *in vivo* experiment was conducted. After injection of hyperpolarized $[1\text{-}^{13}\text{C}]\text{pyruvate}$, the SNR for the summed spectra was easily sufficient to determine the amount of pyruvate and its metabolites observed in the rat model of glioma. The ratio of observed Lac/Pyr was often used as a measurement of local hypoxia to study diseases such as cancer [17]. However, other metabolites such as alanine or bicarbonate could be also monitored [17]. The high SNR resulting from TORO operation permitted quantification of the Lac/Pyr in individual voxels of the rat brain and tumour yielding regional information of tumour metabolism. Tumours manifesting significantly higher Lac/Pyr were well documented in the literature and this biomarker could be used to identify early onset of tumour progression [18] or tumour response to therapy [19, 20]. Other relevant information such as perfusion and angiography could be acquired using ^1H imaging. Exact co-registration of ^1H and ^{13}C data facilitated unambiguous evaluation of the higher resolution ^1H data

with tissue metabolism obtained by ^{13}C imaging. In the future, TORO operation of this RF coil will be used to monitor various animal disease models with hyperpolarized ^{13}C substrates.

In conclusion, this study described the construction of a switch-tuned ^{13}C - ^1H birdcage RF coil and compares its imaging performance with identical single-tuned RF coils as a true measure of its utility and to measure potential SNR losses due to its more complicated circuitry. Imaging comparisons measured a reduction in observed SNR for the switch-tuned ^{13}C - ^1H RF coil compared with identical single-tuned RF coils at either frequency. However, for TORO operation with a ^{13}C surface RF coil, the ^{13}C SNR was 4.2 times higher than ordinary T/R operation of the switch-tuned ^{13}C - ^1H RF coil. The B_1 field profile for ^1H imaging provided uniform RF excitation over a 13-cm FOV. A dual frequency or switch-tuned RF coil permits data acquisition at two distinct frequencies (*i.e.*, for different nuclei) with exact image co-registration for those images. But unlike a dual frequency RF coil, the integration of a ^{13}C surface RF coil with the ^{13}C - ^1H switch-tuned RF coil for TORO operation was relatively simple (due to shifts of the resonator frequency) producing significant improvements in imaging SNR. This switch-tuned ^{13}C - ^1H RF birdcage coil operating with a ^{13}C receive-only surface RF coil in TORO mode was extremely useful for analyzing *in vivo* models where anatomic information of ^1H images provides a high-resolution background against which to evaluate regional metabolic information obtained by ^{13}C spectroscopy or imaging with enhanced SNR.

2.5 Acknowledgements

The authors wish to thank useful discussions with Andrew Alejski, Kyle Gilbert and Jian-xiong Wang for various aspects of design of the RF hardware. The animal support bed and RF fixation hardware were fabricated by Brian Dalrymple and Frank Van Sas. We wish to acknowledge the help of Trevor Wade for assistance with B_1 mapping and Albert Chen for initial advice and consultation regarding hyperpolarized imaging of animal models. We would also like to thank the laboratory of Paula Foster for initial help with our tumour model.

References for Chapter 2

1. Wolber, J., et al., *Generating highly polarized nuclear spins in solution using dynamic nuclear polarization*. Nuclear Instruments & Methods in Physics Research Section a-Accelerators Spectrometers Detectors and Associated Equipment, 2004. **526**(1-2): p. 173-181.
2. Ardenkjaer-Larsen, J.H., et al., *Increase in signal-to-noise ratio of > 10,000 times in liquid-state NMR*. Proc Natl Acad Sci U S A, 2003. **100**(18): p. 10158-63.
3. Alberts, B., et al., *Molecular Biology of the Cell 4th Edition: International Student Edition*. 2002: Taylor & Francis Group.
4. Golman, K., et al., *Metabolic imaging by hyperpolarized C-13 magnetic resonance imaging for in vivo tumor diagnosis*. Cancer Research, 2006. **66**(22): p. 10855-10860.
5. Golman, K., R. in't Zandt, and M. Thaning, *Real-time metabolic imaging*. Proceedings of the National Academy of Sciences of the United States of America, 2006. **103**(30): p. 11270-11275.
6. Golman, K., et al., *Cardiac metabolism measured noninvasively by hyperpolarized C-13 MRI*. Magnetic Resonance in Medicine, 2008. **59**(5): p. 1005-1013.
7. Haacke, E.M., et al., *Magnetic Resonance Imaging: Physical Principles and Sequence Design*. 1999: Wiley.
8. Chin, C., et al., *Birdcage Builder, version 1.0*, in *Copyright Center for NMR Research, Dept. Radiology, Pennsylvania State University College of Medicine*. 1998.
9. Hayes, C.E., et al., *An Efficient, Highly Homogeneous Radiofrequency Coil for Whole-Body Nmr Imaging at 1.5-T*. Journal of Magnetic Resonance, 1985. **63**(3): p. 622-628.
10. Mispelter, J., M. Lupu, and A. Briguet, *NMR Probeheads for Biophysical And Biomedical Experiments: Theoretical Principles And Practical Guidelines*. 2006: Imperial College Press.
11. Wang, J.-X., et al., *An Efficient Switched Double-Frequency Birdcage Coil for 3He and 1H Imaging*, in *ISMRM 16th Scientific Meeting & Exhibition*. 2008: Toronto, Ontario, Canada.
12. Firbank, M.J., et al., *A comparison of two methods for measuring the signal to noise ratio on MR images*. Phys Med Biol, 1999. **44**(12): p. N261-4.

13. Wade, T.P., C. Mckenzie, and B.K. Rutt, *No Inversion Double Angle Look-Locker (niDALL) for Flip Angle Mapping*, in *Joint Annual Meeting ISMRM-ESMRMB 2010*. 2010: Stockholm, Sweden.
14. Chattergoon, N., et al., *Field dependence of T1 for hyperpolarized [1-13C]pyruvate*. *Contrast Media Mol Imaging*, 2013. **8**(1): p. 57-62.
15. Shen, G.X., F.E. Boada, and K.R. Thulborn, *Dual-frequency, dual-quadrature, birdcage RF coil design with identical B-1 pattern for sodium and proton imaging of the human brain at 1.5 T*. *Magnetic Resonance in Medicine*, 1997. **38**(5): p. 717-725.
16. Barberi, E.A., et al., *A transmit-only/receive-only (TORO) RF system for high-field MRI/MRS applications*. *Magn Reson Med*, 2000. **43**(2): p. 284-9.
17. Gallagher, F.A., M.I. Kettunen, and K.M. Brindle, *Biomedical applications of hyperpolarized C-13 magnetic resonance imaging*. *Progress in Nuclear Magnetic Resonance Spectroscopy*, 2009. **55**(4): p. 285-295.
18. Chen, A.P., et al., *Hyperpolarized C-13 spectroscopic imaging of the TRAMP mouse at 3T-initial experience*. *Magn Reson Med*, 2007. **58**(6): p. 1099-106.
19. Park, I., et al., *Detection of Early Response to Temozolomide Treatment in Brain Tumors Using Hyperpolarized C-13 MR Metabolic Imaging*. *Journal of Magnetic Resonance Imaging*, 2011. **33**(6): p. 1284-1290.
20. Park, I., et al., *Hyperpolarized C-13 magnetic resonance metabolic imaging: application to brain tumors*. *Neuro-Oncology*, 2010. **12**(2): p. 133-144.

Chapter 3

3 Monitoring early changes in tumour metabolism in response to therapy using hyperpolarized ^{13}C MRSI in a preclinical model of glioma

Heeseung Lim, Francisco Martinez-Santesteban, Michael D. Jensen, Albert Chen, Eugene Wong and Timothy J. Scholl

The manuscript has been submitted to the Scientific Reports and is in the process of revision. May 2017 SREP-17-22263

3.1 Introduction

Brain cancer is a challenging disease with very poor prognosis and outcomes. The most prevalent form of malignant brain tumours is glioma, which arises from glial cells.[1] While there are aggressive therapies available (*i.e.* surgical resection, radiotherapy, and chemotherapy), patients diagnosed with the most aggressive (grade IV) malignant glioma have a disappointing five-year survival rate of 5.1%. [2] Despite aggressive treatment, these tumours almost inevitably recur.[3]

Advances in imaging techniques help radiologists to noninvasively detect and assess brain tumours. Magnetic resonance imaging (MRI) is the preferred clinical diagnostic tool for brain tumour detection,[4] yet it is still challenging to observe both the therapeutic response and efficacy during the course of the treatments. Because radiotherapy and chemotherapy affect tumours at the molecular level (DNA damage, blocking protein/RNA), phenotypical changes (tumour size, diffusion, proliferation) that arise from therapies, can be challenging to detect during the early staging of treatment.

Clinical assessment of the progression of a primary brain tumour can be assessed by contrast-enhanced MRI using one of the following criteria: Response Assessment in Neuro-Oncology (RANO) criteria, Response Evaluation Criteria in Solid Tumours (RECIST) or World Health Organization criteria.[5, 6] The RANO criteria, updated from MacDonald criteria, includes measurable morphological changes in the tumour size due

to therapy. Tumour response is divided into four different groups based on changes in contrast-enhancing tumour volumes: 1. complete response with no tumour enhancement, 2. partial response with > 50% reduction in tumour size, 3. progressive disease with > 25% increase in tumour size, and 4. stable disease with no changes in tumour size. Other criteria methods use similar categorizations of groups but differ in methodology for measurement of tumour size. All criteria methods depend on the post contrast-enhancement of tumours visualized using MRI. However, it is often difficult to determine if the enhancement is a result of tumour reoccurrence, radiation necrosis or pseudo-progression.[5]

Tumour metabolism has been identified as a “hallmark of cancer”.[7] Tumours require an increased amount of energy and nutrients to proliferate at a much faster rate compared to healthy tissues. To sustain increased energy demands, tumour metabolism is altered.[8] Most notably, energy production in tumour cells often switches from predominantly oxidative phosphorylation in the mitochondria (Krebs cycle) to anaerobic glycolysis (followed by lactic acid fermentation) in the cytosol.[9, 10] This is also known as Warburg Effect. This choice of energy production generates an intracellular pool of lactic acid as a potential molecular imaging biomarker.[11] Moreover, the excretion of lactic acid and protons from tumour cells accelerates acidification of the extracellular space and increases the viability of these cells through further vascularization.[10] Clinical studies have demonstrated an increased metabolic uptake of 2-deoxy-2-[¹⁸F]fluoro-D-glucose (¹⁸F-FDG) in tumours using positron emission tomography (PET).[12, 13] The ability to monitor therapeutic changes accurately and in a timely manner in brain tumours will provide a further understanding of tumour metabolism and guide initiation of alternative (or salvage) therapies.

Hyperpolarized ¹³C magnetic resonance spectroscopic imaging (¹³C MRSI) is an emerging molecular imaging tool with MRI that can directly quantify metabolic changes in tissues. A chosen cellular substrate is enriched with ¹³C and then hyperpolarized (highly magnetized) in the polarizer to increase the potential ¹³C MRSI signal by nearly five orders of magnitude.[14] After injection of the hyperpolarized ¹³C-enriched substrate, the substrate and its byproducts from metabolic processes can be individually

detected *in vivo* by their inherent chemical shifts using magnetic resonance. The hyperpolarized signal is transient as the magnetization of the ^{13}C nuclei relaxes to thermal equilibrium. This is highly dependent on the hyperpolarized contrast agent's spin-lattice relaxation time (T_1) and that of its metabolic byproducts.[15]

The most common and widely researched hyperpolarized ^{13}C contrast agent is [1- ^{13}C]pyruvate.[16] After a bolus injection and circulation, hyperpolarized [1- ^{13}C]pyruvate is taken up by cells through active transport,[17] and converted into three major metabolic byproducts: [1- ^{13}C]alanine, ^{13}C bicarbonate and [1- ^{13}C]lactate.[16] Tumours exhibit increased lactate production through upregulated lactate dehydrogenase (LDH) production by oncogenes.[9] Cells targeted by metabolic therapy have reduced LDH activity and thereby often exhibit reduced lactate production.[18, 19] The production of [1- ^{13}C]lactate in tumour tissues by metabolizing injected hyperpolarized [1- ^{13}C]pyruvate can be tracked using ^{13}C MRSI. In this way, the therapeutic response of tumours is monitored by measuring changes in [1- ^{13}C]lactate conversion from [1- ^{13}C]pyruvate.

Both glioma and brain tissues are highly metabolic and readily uptake metabolites for energy. This reduces the contrast and effectiveness of ^{18}F -FDG PET for imaging and quantification of brain tumours which must be confirmed by other means.[13, 20, 21] For instance, brain tissues express high background signal with ^{18}F -FDG PET, particularly in the cortex, due to high metabolic activity.[22] On the other hand, pyruvate is actively taken up by glioma cells through monocarboxylate transport and rapidly converted to lactate by upregulated LDH activity.[23, 24] Glioma cells are highly proliferative, utilizing the lactate alternative energy source as well as amino acid production.[11] Thus, MRSI of hyperpolarized [1- ^{13}C]pyruvate has an advantage of directly measuring metabolic activity in glioma cells and the ability to distinguish these cells from other highly metabolic brain tissues through their altered metabolic signature.

The purpose of this study was to monitor the metabolic response of tumours to chemo- and radiotherapies using hyperpolarized ^{13}C MRSI in an orthotopic rat model of glioma and compare with conventional methods of treatment response assessment. Assessment of tumour response to therapy using hyperpolarized ^{13}C MRSI has been shown in several

models and therapies;[25-29] however, no longitudinal study has compared therapeutic responses to different therapies. Since each therapy relies on a different treatment mechanism, this will likely produce different metabolic responses to treatment. As discussed above, tumour response to therapy can be assessed by the observed ratio of [1-¹³C]lactate with respect to [1-¹³C]pyruvate in the cytosol of tumour cells using ¹³C MRSI. The results of this study illustrate the ability of ¹³C MRSI of hyperpolarized [1-¹³C]pyruvate to quantify therapeutic response for different therapies and to follow tumour progression or response with noninvasive longitudinal imaging.

3.2 Methods

3.2.1 Pyruvic acid sample preparation

A trityl radical, OX63 (Oxford Instruments, Concord MA, U.S.A.) was mixed with 99%-enriched [1-¹³C]pyruvic acid (Sigma Aldrich, Miamisburg OH, U.S.A) to a final concentration of 15mM. The pyruvic acid preparation was stirred and heated to 60°C to dissolve, then cooled and stored at -4°C for later use. Before hyperpolarization, ProHance gadolinium contrast agent (Bracco Diagnostics, Monroe Township, NJ, U.S.A.) was added at a concentration of 1 mM to the pyruvic acid sample to enhance polarization and reduce polarization time.[30]

3.2.2 Hyperpolarization

A Hypersense dynamic nuclear polarizer (Oxford Instruments, Abingdon, UK) was used to hyperpolarize the prepared [1-¹³C]pyruvic acid sample. The DNP operates at a temperature of 1.4 K and a magnetic field strength of 3.35 T. The pyruvic acid preparation was irradiated with microwaves from a source operating at 94.125 GHz achieving ~90% nuclear polarization of the solid after 45 min. For dissolution, the sample was rapidly thawed and mixed with a super-heated 80-mM phosphate buffer solution containing 0.34-mmol/L ethylenediaminetetraacetic acid. The resulting solution was dispensed into a flask prior to uptake into a syringe for injection. The resulting 80-mM hyperpolarized [1-¹³C] pyruvate buffered solution had a final volume of ~4 ml with a pH of 7.4 at 37°C. Its measured T_1 was ~ 65 s at 3 Tesla[15] and its liquid-state polarization was > 12%.

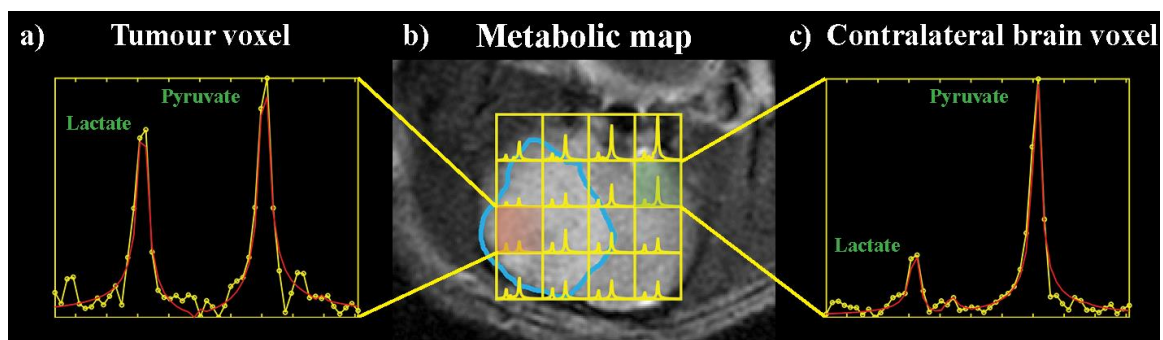


Figure 3-1 Hyperpolarized ^{13}C spectra of a rat brain with tumour. b) Regional spectral data overlaid on T_2 -weighted image. Tumour has been outlined in cyan. a) & c) Individual spectra from tumour and contralateral brain voxels. Red lines represent line fitting to spectral data in yellow. Note the increased lactate signal relative to pyruvate signal in the tumour voxel.

3.2.3 *In Vivo* Imaging

All imaging sessions were performed using a GE Discovery MR750 3.0 T MRI (General Electric Healthcare, Waukesha WI, U.S.A.). A custom-built, switch-tuned ^{13}C - ^1H radiofrequency (RF) coil with a local ^{13}C receive-only RF coil was used in transmit-only/receive-only operating mode for ^{13}C imaging.[31] Switch-tuning between ^1H and ^{13}C frequencies produced inherently registered images for morphology (^1H) and metabolism (^{13}C). A single imaging session consisted of (in sequential order), T_2 -weighted ^1H imaging, hyperpolarized ^{13}C MRSI, and post-Gd contrast T_1 -weighted ^1H imaging. T_2 -weighted ^1H images were acquired using a fast spin echo pulse sequence with the following imaging parameters: 80×80 mm field of view (FOV), 0.3-mm isotropic in-plane resolution, 3-mm slice thickness, repetition time (TR) = 4000 ms, echo time (TE) = 85 ms, bandwidth = 10.42 Hz, echo train length = 16 and number of averages = 4. For hyperpolarized ^{13}C MRSI, animals were injected by tail vein with approximately a 3-ml bolus of the buffered hyperpolarized $[1\text{-}^{13}\text{C}]\text{pyruvate}$ solution. 2D ^{13}C -spectral maps were acquired 25 s after the injection using free induction decay chemical shift imaging (FID-CSI) with the following parameters: 60×60 mm FOV, 5-mm isotropic in-plane resolution, slice thickness = 10 to 15 mm (depending on tumour extent), TR = 80 ms, spectral width = 5000 Hz and number of points = 256. Regional ^{13}C -spectra are

shown in Figure 3-1. Prior to T_1 -weighted ^1H imaging, 100 mM of Magnevist (Bayer HealthCare Pharmaceuticals Inc., Whippany NJ, U.S.A.) was injected by tail vein catheter. T_1 -weighted ^1H images were acquired using a fast gradient echo pulse sequence with the following parameters: $80 \times 40 \times 32$ mm FOV, 0.5-mm isotropic resolution, flip angle = 25° , TR = 6.9 ms, TE = 2.9 ms and 9 averages.

3.2.4 Animal disease model

Eighteen male Wistar rats (Charles River Laboratories, Senneville, QC, Canada) with an initial weight of ~ 250 g (~ 5 to 7 weeks old) were used for this study. One million rat glioma cells C6 (CCL-107, Purchased 2011, American Type Culture Collection, Manassas, VA, U.S.A.) were stereotactically implanted in the caudate nucleus of the right brain hemisphere (day 0). C6 cells were passaged 9 times and tested for mycoplasma using MycoAlertTM (Lonza, Mississauga, ON, Canada) before use. Seven days post cell implantation, animals underwent pre-therapy imaging sessions. On day 10, animals were randomly divided into four groups: 1. no therapy, 2. radiotherapy, 3. chemotherapy, and 4. radio- and chemotherapy (combined therapy). Group 1 (no therapy) functioned as the control group. The radiotherapy group received a localized radiation dose of 20 Gy in two fractions on two consecutive days to the tumour using a μCT GE Vision 120CT (General Electric Healthcare, Waukesha WI, U.S.A.) with a custom-built collimator.[32] The chemotherapy group received intraperitoneal injections of 40 mg/kg of TMZ (Sigma Aldrich, Miamisburg OH, U.S.A.) dissolved in dimethyl sulfoxide for 5 consecutive days. The combined therapy group received both therapies, with the same timeline as described above. Starting on day 12, and every 3 days thereafter, animals underwent post-therapy imaging sessions. At endpoint, rats were sacrificed for histological examination. All animal procedures were approved by the University Council on Animal Care, Animal Use Subcommittee.

3.2.5 Histology

Following the final post-therapy imaging session, the rats were injected by tail vein catheter with 60-mg/kg Pimonidazole (Hypoxyprobe Inc., Burlington MA, U.S.A.) 30 minutes prior to sacrifice. The rats were then sacrificed, perfused with 4%

paraformaldehyde (Sigma Aldrich, Miamisburg OH, U.S.A), and the brains were extracted and refrigerated at 5 °C in 4% paraformaldehyde. The brains were then sectioned to 5-mm-thick paraffin slabs and later further sectioned to 5 μm for staining. Brain sections were stained with hematoxylin & eosin (H&E) and for hypoxia. Whole-brain sectioned slices were scanned using light-fluorescent microscopy (Leica Microsystems Inc., Concord ON, Canada). Histological image slices were co-registered to the MRI images using Slicer (Version 4.31, Surgical Planning Laboratory, Brigham & Women's Hospital Boston MA, U.S.A.) using a custom software plugin.[33]

3.2.6 Image analysis

The ¹³C MRSI raw data were analyzed using a custom-written MATLAB (MathWorks, Natick MA, U.S.A.) script. Free induction decay signals from each k -space point were apodized by a 20-Hz Gaussian filter. The signals were spatially zero-filled and then Fourier transformed in frequency and phase-encoding directions. Signal for the individual metabolites is represented by the time-domain signal function as described in reference [34]:

$$S(t) = Ae^{-i\Omega t + \phi} e^{-R_2^* t}. \quad \text{Equation 3-1}$$

Here, $S(t)$ is the signal at time t , A is the amplitude of the signal, Ω is the frequency offset, and ϕ is the phase offset. R_2^* is the effective spin-spin relaxation rate given by $R_2^* = \frac{1}{T_2^*}$. Each voxel could potentially contain up to 5 different summed metabolite signals. Initial estimates for the parameters for each individual metabolite (A_i , Ω_i , ϕ_i , and R_{2i}^*) were obtained by examining the data. The summed signal model for all observed metabolites was fitted to the processed data by a nonlinear least-squares curve-fitting method on a voxel-by-voxel basis to extract metabolite parameters and their uncertainties. These parameters were used to calculate the lactate to pyruvate ratio (Lac/Pyr ratio) and propagate an associated uncertainty. An example of spectral fitting is showing in Figure 3-1.

3.2.7 Statistics

Post-Gd tumour volumes were measured from the T_1 -weighted contrast images using ITK-Snap (www.itksnap.org, [35]). Boundaries of tumours were manually contoured and the volumes were calculated. Inter-observer variability was used for the error of tumour volume. Cohort statistics were calculated using SPSS (IBM Corp., Armonk, NY USA). Analysis of variance (ANOVA) with Dunnett's post hoc test was performed to calculate the statistical differences between groups at each day and overall group differences respectively. The uncertainties propagated from parameter fitting were used to weight Lac/Pyr ratios for ANOVA analysis. Uncertainties for the Lac/Pyr ratio are reported as standard error of the mean of measurements. The correlations between Lac/Pyr ratio, tumour volume and tumour growth rate were tested using Pearson correlation.

3.3 Results

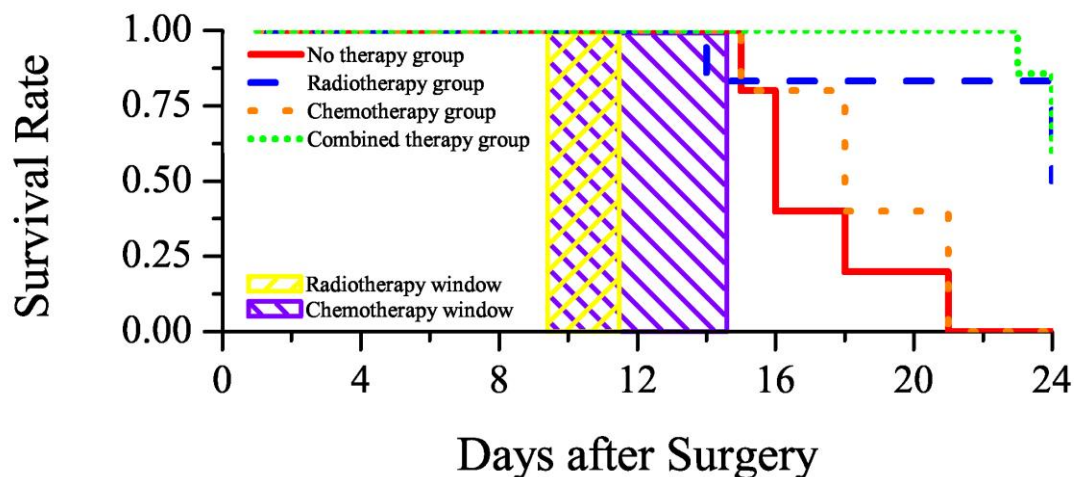


Figure 3-2 Kaplan-Meier survival plot. Tumour implantation surgery was on Day 0 and the experimental endpoint was Day 24. Therapies were initiated on Day 10, lasting 2 days for radiotherapy and 5 days for chemotherapy. Specific details regarding the therapies are included in the text.

A total of 18 rodents were monitored using hyperpolarized $[1-^{13}\text{C}]$ pyruvate MRSI at multiple time points: 7, 12, 15, 18, 21 and 24 days after tumour implantation. During the course of the longitudinal study, the health of some animals deteriorated due to the increased tumour burden and these animals were sacrificed earlier than the expected endpoint. Figure 3-2 depicts the survival rate of each group. The radio- and combined therapy groups had the highest mean survival time at 25 days followed by chemotherapy at 18 days and lastly the no therapy group at 17 days. A Kaplan-Meier method was used to determine if there were any differences in the survival distribution for the therapy groups. The survival distributions for different therapy groups are statistically different ($p < 0.0005$).

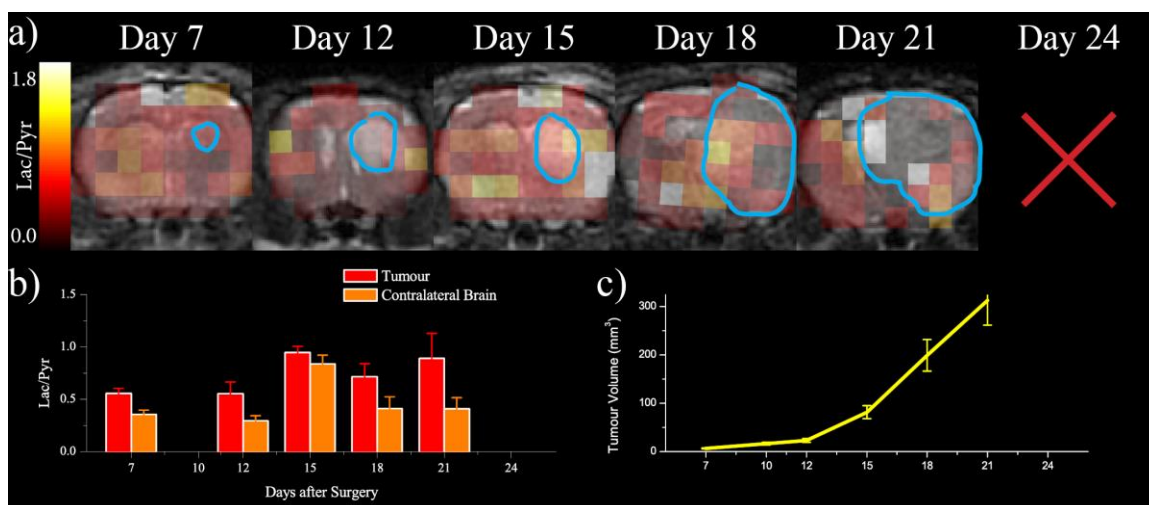


Figure 3-3 A single representative animal from the *no therapy* group. a) Lactate-to-Pyruvate ratio maps are overlaid on axial proton images of the rat brain at longitudinal imaging time points. Tumours are outlined by cyan boundaries. b) Bar graph of measured lactate-to-pyruvate ratio of tumours and contralateral brain volumes at different imaging sessions. c) Graph of tumour volume for all imaging time points. The error bars for Lac/Pyr data represent one measurement standard deviation. The uncertainty for the tumour volume was estimated from inter-observer measurement variability.

Figures 3-3 and 3-4 illustrate longitudinal assessments of therapeutic response in a rat model of glioma comparing Lac/Pyr ratio and tumour volume. Figure 3-3 shows longitudinal imaging data for a representative rodent from the no-therapy group. Rapid tumour growth is readily apparent in Figure 3-3 a) and is quantified in 3-3 c). Longitudinal measurements of the Lac/Pyr ratio are presented in Figure 3-3 b), comparing tumour and contralateral brain for each ^{13}C imaging session. Higher Lac/Pyr ratios are observed in tumour tissue compared to contralateral brain tissue. Lac/Pyr ratio increased with tumour growth. As illustrated in Figure 3-3 c), without any therapy, the tumour grew rapidly. Due to the large tumour burden and resulting adverse health effects, the rodent was sacrificed before the last imaging session at day 24, in compliance with terms of the animal use protocol. Neurological impairment and lack of appetite were observed for all rodents that did not receive therapy and as a result, these animals were sacrificed before the final imaging time point, typically between days 15 and 21.

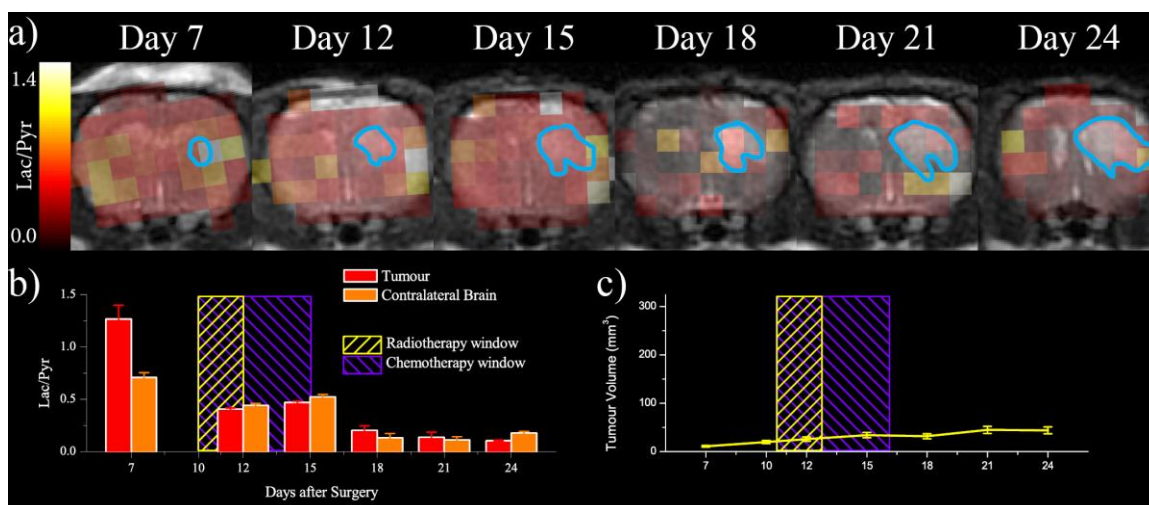


Figure 3-4 Representative animal from the *combined therapy* group. a) Lactate-to-Pyruvate ratio maps are overlaid on axial proton images of the rat brain at longitudinal imaging time points. Tumours are outlined by cyan boundaries. b) Bar graph of measured lactate-to-pyruvate ratio of tumours and contralateral brain volumes at different imaging sessions. Treatment periods are indicated as hatched areas. c) Graph of tumour volume for all imaging time points. The error bars for Lac/Pyr data represent one measurement standard deviation. The uncertainty for the tumour volume was estimated from inter-observer measurement variability.

Figure 3-4 shows a representative rodent from the combined therapy group. Tumour growth shown in Figure 3-4 a) and quantified in 3-4 c) is slower compared to that of the no therapy group. On day 7, the Lac/Pyr ratio is higher in the tumour than in contralateral brain tissue (see Figure 3-4 b)). Within two days post therapy, the tumour Lac/Pyr ratio drops to that of contralateral brain. Further longitudinal measurements show similar Lac/Pyr ratios in tumour and healthy brain until the final imaging session on day 24. Reduced tumour growth assessed by volume measurements commensurate with therapeutic response was not apparent until day 21.

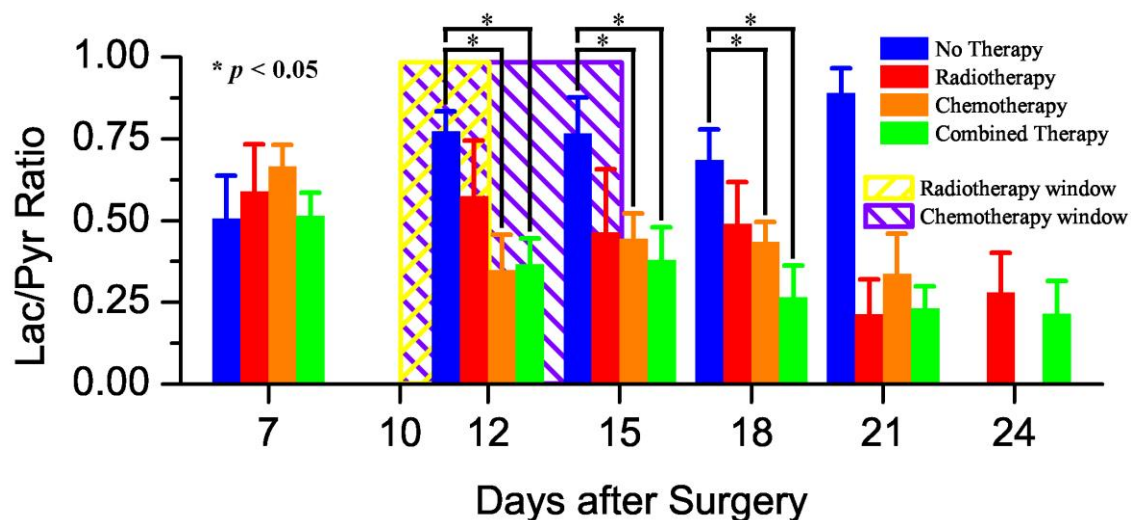


Figure 3-5 Longitudinal assessment of the lactate-to-pyruvate ratio in tumour tissue for four therapy groups. Radio- and chemotherapy were initiated on day 10 for a duration of 2 and 5 days respectively. No statistical comparison between the no therapy and other treatment groups was possible for days 21 and 24 due to the poor survival of the untreated group. (Details of therapy are in the text.) Error bars represent one standard deviation for the averaged animal data.

Figure 3-5 illustrates a longitudinal comparison of the average Lac/Pyr ratio in tumours for the four therapy groups measured up to 24 days post cell implantation. A consistently elevated Lac/Pyr ratio was observed in the tumours for the no therapy group for all time points. No statistical comparison between the no therapy and other treatment groups was possible for days 21 and 24 due to the poor survival of the untreated group. Some of the rodents that received radiotherapy showed a Lac/Pyr ratio reduction in the tumour tissue at day 12, but as a whole, that group did not show a significant reduction ($p \approx 0.33$). The rodents that received either chemotherapy or combined therapy show a statistically significant reduction in the Lac/Pyr ratio within the tumour volumes ($p < 0.05$) post-therapy (Day 12, 15 and 18). However, the rodents that received only chemotherapy did not survive to the endpoint at day 24 despite a significant reduction in the Lac/Pyr ratio. Application of combined therapy produced the best therapeutic response as assessed by tumour Lac/Pyr ratio and confirmed by the survival data.

Tumour volume measured from T_1 -weighted post-Gd images at day 18 show similar trends as Lac/Pyr ratio. In the absence of therapy, tumour volumes significantly increased in size until animals were sacrificed. The average enhancing tumour volume in the no therapy group at endpoint was $384 \pm 63 \text{ mm}^3$. All applied therapies showed reduced tumour growth by endpoint assessed by volume measurement. The average enhancing tumour volume for chemotherapy, radiotherapy and combined therapies were: 140 ± 23 , 107 ± 18 and $54 \pm 9 \text{ mm}^3$ respectively at endpoint. Rodents with tumours that received radiotherapy and combined therapy would be classified as having stable disease based on the RANO criteria. Whereas, for rodents with tumours that received chemotherapy, the observed tumour volume growth rate would produce a classification of progressive disease. Notably, when using only the T_1 -weighted post-Gd images as one would in the clinic, these classifications would only be possible as early as 18 days after cell implantation.

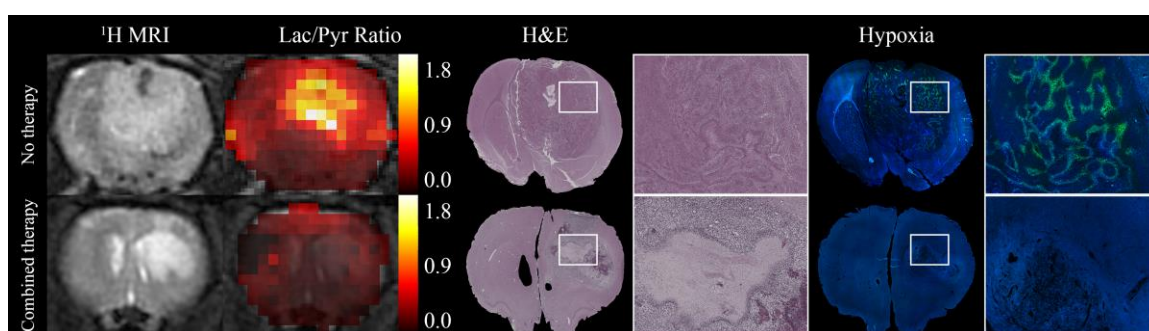


Figure 3-6 Comparison of T_2 -weighted images, lactate-to-pyruvate ratio maps, H&E staining and hypoxia staining for a representative no-therapy and combined therapy animal. A non-rigid image registration method has been used to co-register the histology to the MRI data. Magnified regions for H&E and hypoxia staining are presented next to the histology for the entire brain. Hypoxia staining (Pimonidazole) shows green contrast with blue nucleus counter staining.

Figure 3-6 presents the representative histological results comparing rodents that received either no therapy or combined therapy. The T_2 -weighted image, Lac/Pyr ratio images, and histological sections have been co-registered as described above. The tumours within the brain are easily distinguishable by ^1H MRI and H&E staining. Lac/Pyr ratio and hypoxia

staining show similar contrast between tumour and contralateral brain tissues. Comparing contralateral brain and tumour measurements, rodents that did not receive therapy showed higher Lac/Pyr ratio activity and hypoxia within the tumour, whereas animals that received combined therapy had minimal Lac/Pyr ratio activity through the entire brain and no hypoxia signal within the tumour at endpoint.

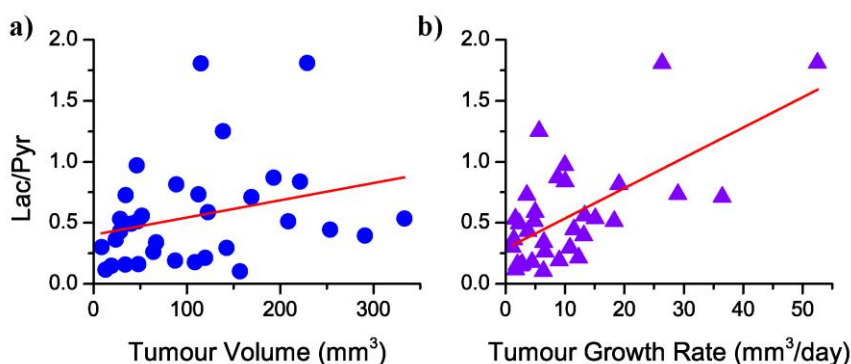


Figure 3-7 Correlation plots for all experimental animal groups. a) Correlation plot of lactate to pyruvate ratio in tumour versus tumour volume b) Correlation plot of lactate to pyruvate ratio in tumour versus tumour growth rate. The Pearson correlation coefficients are 0.287 ($p \sim 0.105$) and 0.66 ($p < 0.001$) and R^2 -values are 0.083 and 0.416 for panels a) and b) respectively. Tumour volumes (in mm^3) were estimated at each imaging time point from T_1 -weighted images acquired after contrast enhancement. An exponential growth model was fit to the tumour volume data to estimate tumour growth rate in mm^3/day .

Tumour volumes were contoured and measured using post-Gd contrast enhanced T_1 -weighted images acquired at each imaging time point. Tumour growth rates were modeled from these measurements. The correlations of tumour Lac/Pyr ratio versus tumour volume and growth rate are presented in Figure 3-7. The Pearson correlation coefficients for these data are 0.287 ($p \sim 0.105$) and 0.66 ($p < 0.001$) respectively. Tumour Lac/Pyr ratio was not correlated with tumour volume; however, a moderate and statistically significant correlation with tumour growth rate was observed.

3.4 Discussion

The goal of this study was to demonstrate the ability to detect early changes in therapeutic response in tumours using hyperpolarized [1-¹³C]pyruvate MRSI and to evaluate potential clinical translation. Targeted therapy of tumour metabolism has gained more interest recently but therapeutic effects on tumour metabolism are not fully understood.[36] The ability to measure metabolic changes in tumours will aid to not only further understand tumour metabolism, but may also provide biomarkers to determine which therapeutic methods will be effective against tumours.

The C6 rodent glioma model was chosen to study the therapeutic response of solid tumours because this model is well established in the literature and its tumour characteristics are well defined.[37, 38] During glioma progression, the tumour evolves into two different regions. The outer layer of tumour is highly vascularized and well-perfused, whereas the inner core of the tumour becomes necrotic and hypoxic due to lack of functioning or effective vasculature.[39] In addition, as the tumour grows, the blood brain barrier becomes disrupted, which can allow for increased fluid exchange with the vasculature.[40] In MRI, tumours, edema, and cerebrospinal fluid appear hyperintense on T_2 -weighted ¹H images,[41] complicating tumour volume measurements. Therefore, T_1 -weighted post-Gd ¹H images were used to measure tumour volumes. Given that malignant glioma possesses disrupted and leaky vasculature, low-molecular weight paramagnetic contrast agents can effectively accumulate within the tumour.[42] Post-Gd-contrast T_1 -weighted ¹H images were used to determine tumour volumes in this study. Contrast-enhanced tumours have increased conspicuity with hyperintense contrast compared to surrounding brain tissue for T_1 -weighted ¹H images. In addition, regions of edema and necrosis can be discriminated by lack of enhancement.[43]

Figures 3-3 and 3-4 show the progression of glioma in two different therapy groups using tumour volumes measured from T_1 -weighted ¹H images. C6 glioma cells are extremely aggressive and grow exponentially as shown Figures 3-3a) & c). The RECIST criteria are the conventional indicators of therapeutic response. Post-therapy success is associated with stability or recession of tumour size. To detect post-therapeutic changes, tumour volume must be monitored repeatedly after therapy. In this model, using the standard

clinical method of detection with ^1H imaging, the earliest post-therapeutic tumour volume changes were observed on day 18 (8 days after the therapy was given) and later confirmed to be stable disease. Tumour recurrence was not observable in this study due to the finite length of the study. Prolonged monitoring of post-therapeutic tumour volume changes would be required to dismiss tumour recurrence. Considering that most malignant gliomas eventually recur despite rigorous therapies,[1] early detection of therapeutic response or progression would not only be essential for prediction of prognosis but also improve quality of life for patients by terminating treatment when it is not effective.

The purpose of this study was to evaluate the effectiveness of hyperpolarized ^{13}C MRSI to detect early therapeutic changes by measuring tumour metabolism. Metabolic changes such as upregulated glucose uptake in tumours are clinically assessed by ^{18}F -FDG PET. However, ^{18}F -FDG is also readily taken up by highly metabolic tissue. This leads to the possibility of false positive results for ^{18}F -FDG PET, which may require confirmation by other means.[13, 20, 21] For example, high metabolic activity in the cortex of the brain can produce an elevated background signal, which confounds the interpretation of ^{18}F -FDG PET results.[22] As an alternative, radiolabeled amino acids can be used to target brain tumours because amino acids are essential to highly proliferating tissues.[22, 44]

Hyperpolarized ^{13}C -labeled glucose can be used in a similar manner as ^{18}F -FDG for tumour detection and characterization; however significant challenges exist. First, the T_1 of hyperpolarized ^{13}C labeled glucose is too short (< 2 s) for detection of metabolic byproducts.[45] The T_1 of glucose can be substantially increased by replacing all protons in the glucose with deuterium but this significantly increases the cost of this substrate.[46] Secondly, the labeling of various carbon atoms in the glucose molecule results in different chemical shifts for its ^{13}C nuclei and those of its metabolic byproducts. Often these chemical shifts are close to each other, which complicates the separation of metabolites as the spectrum becomes congested. In this study, we used $[1-^{13}\text{C}]$ pyruvate as the metabolic probe agent, which offers several advantages over glucose. The T_1 of $[1-^{13}\text{C}]$ pyruvate at 3 T is ~ 65 s *in vitro* (~ 45 s *in vivo*), which is long enough for pyruvate to circulate through the circulatory system of our animal model and converted to

downstream metabolites.[15] Furthermore, the ^{13}C -labeled carbon can only be transferred to four different metabolites; lactate, pyruvate hydrate, alanine, and bicarbonate. All these metabolites are individually represented as single spectral peaks and are well separated by their chemical shifts producing a fully resolved spectrum, which can be readily quantified as shown in Figure 3-1.

Among the metabolites produced from $[1-^{13}\text{C}]$ pyruvate, the $[1-^{13}\text{C}]$ lactate signal is a sensitive biomarker for therapeutic effect in tumours where its production from pyruvate can be correlated with LDH activity and lactate pool (cellular redox state). The $[1-^{13}\text{C}]$ lactate signal is normalized to the $[1-^{13}\text{C}]$ pyruvate signal to mitigate differences in pyruvate delivery and uptake in tumours and compared with that of healthy brain tissue. Increased LDH activity in metabolically active tumour cells will result in an increase in observed Lac/Pyr ratio, whereas necrotic tumour regions or healthy cells will have little to no lactate production as a result of limited LDH activity and a lower Lac/Pyr ratio. As illustrated in the representative case for a rodent that received no therapy in Figure 3-3 b), the Lac/Pyr ratio in tumour tissue is consistently larger than that of the healthy contralateral brain tissue. Furthermore, increased Lac/Pyr ratio corresponds to rapid progression of the tumour as shown in Figure 3-3 c). This is further demonstrated in the correlation plots of Figure 3-7. Here, tumour volume does not statistically correlate with Lac/Pyr ratio. Yet, there was a moderate and statistically significant correlation between Lac/Pyr ratio and tumour growth rate. Thus, Lac/Pyr ratio is potentially related to the growth of tumour which coincides with increased LDH activity rather than tumour volume.[47] This suggests that in principle, measurement of Lac/Pyr ratio at a single time point can be predictive of tumour response, which would require longitudinal tumour volume measurements over time for conventional assessment.

As tumours rapidly grow, ineffective vascularization and necrosis of the core becomes evident. In Figure 3-3 a), particularly on day 21, there was inadequate delivery of hyperpolarized $[1-^{13}\text{C}]$ pyruvate to regions of the tumour precluding sufficient metabolite signal for accurate quantification of the Lac/Pyr ratio. For representative animals, blood volume and flow were longitudinally measured using dynamic susceptibility contrast imaging (data not shown). The blood flow and blood volume in tumour were lower than

contralateral brain and this may indicate decreased tumour perfusion and possibly necrosis at that time point.

Conversely, as illustrated in the representative case for the rodent that received combined therapy (Figure 3-4 b)), two days after starting the combined therapies, the tumour already exhibited a reduced Lac/Pyr ratio compared to day 7. This ratio was comparable to that of the remaining brain tissue over the rest of the longitudinal experiment. Changes in Lac/Pyr ratio in tumour tissue directly suggests a reduction in LDH activity and cell death and potentially effective therapeutic response. Measured Lac/Pyr ratios in both tumour and contralateral brain declined and remained low after the window of therapy. This might be a result of inflammation, which subsided after treatment caused by radiotherapy, intracranial hypertension from the growing tumour and/or a side-effect of the administration of chemotherapy.[48] For this representative animal, blood flow and blood volume in the tumour and contralateral brain were also measured. The blood flow and blood volume in tumour were returned to a level consistent with the contralateral brain region approximately 14 days after therapy. (data not shown) The restoration of blood flow and blood volume suggests changes in tumour vasculature due to therapy. However, this observation can be only made in the later time points of the experiment. The large variation in blood flow and blood volume is a result of differences between the boundary of the tumour compared to the core of tumour.[49] The boundary of the tumour shows increased blood flow and blood volume compared to the core when it is treated. This leads to a reduction in therapeutic efficacy near the tumour core where there is limited blood flow and blood volume.

In the clinic, patients diagnosed with glioma undergo surgery followed by radio- and chemotherapy.[50] Unfortunately, the effectiveness of a particular therapeutic method for an individual patient may be unclear because of variation in tumour progression among patients. Determining the efficacy of therapy as early as possible would provide an important tool for evaluation of new therapies and improved survival to patients. Figure 3-5 shows the average Lac/Pyr ratio in tumours for the no therapy group and three therapy groups. As expected, the no therapy group shows elevated Lac/Pyr ratio sustained throughout the study, which is possibly due to increased tumour LDH activity. Blood

flow and blood volume ratios suggests that the tumour was poorly vascularized and necrotic; however, these data were not collected for all animals and, as a result, no absolute conclusion can be drawn.

Among the three therapy groups (radiotherapy, chemotherapy, and combined therapy), the combined therapy group had the highest survivability and displayed significant reduction in Lac/Pyr ratio within the tumours. Combined therapy is expected to induce greater DNA damage compared to a single therapy alone, which leads to cellular apoptosis, reduced LDH activity and tumour burden.[51] In the literature, significant evidence exists suggesting radiotherapy helps to increase vasculature permeability and improve delivery of chemotherapeutic drugs to tumour sites.[52, 53] The chemotherapy group showed a statistically significant reduction of Lac/Pyr ratio in tumours; however, this group of rats had a high rate of mortality. Chemotherapy animals lost a significant amount of weight after therapy despite a moderate dose of TMZ given to those rats.[54, 55] TMZ is known to cause nausea, vomiting, fatigue, headache as adverse reactions in human.[55, 56] These side effects, may have been the cause of weight loss for these animals, which negatively impacted their survivability. This may suggest that chemotherapy on its own is sufficient to cause dysfunction in tumour metabolism and proliferation; however, it is not potent enough alone to extend survival. The radiotherapy group has a slow and not statistically significant decline in the Lac/Pyr ratio, yet this group had low mortality compared to the chemotherapy group. In fact, there was a large variation in the Lac/Pyr ratio after therapy among the radiotherapy group suggesting the radiotherapy efficacy varies among the cohort. Despite injecting approximately the same number of C6 cells and providing a standard conformal radiation dose, an individual animal can show a varied therapeutic response to radiotherapy. Those tumours that did not respond to radiotherapy may indicate resistance to therapy and tumour recurrence. However, the experimental timeline would need to be extended to confirm the metabolic profile associated with resistance to therapy and recurrence.

Lastly, Figure 3-6 presents histological validation of Lac/Pyr measurements in the tumour model. Histological sections have been co-registered to the MR imaging data for accurate comparison. Tumour location and size are apparent from H&E images and with ¹H MRI.

Although the T_2 -weighted contrast would suggest that the tumours are relatively homogenous, at least in structure, it is apparent from the Lac/Pyr ratio map and hypoxia staining that tumour metabolism varies throughout the tumour. The untreated tumour shows strong hypoxia staining as well as a high Lac/Pyr ratio. As previously noted in the literature, the tumour environment becomes hypoxic leading to increasing LDH activity. However, following effective therapy, the large reduction in the Lac/Pyr ratio shown in the combined therapy group compared to the no therapy group suggest a reduction in LDH activity. This is further verified by differences in the hypoxia staining between these two cohorts. For the untreated tumour, increased LDH activity is associated with a hypoxic tumour environment due to insufficient or inefficient vascularization, which was verified by hypoxia staining at endpoint. For the combined therapy group, reduced hypoxia was observed commensurate with the lower measured Lac/Pyr ratios. Looking forward to clinical translation, these findings suggest that the Lac/Pyr ratio is a non-invasive imaging biomarker for assessment of hypoxia in the tumour microenvironment, which may be a useful tool for early assessment of tumour response to therapy.

In summary, this study examined longitudinal therapeutic response to different therapies using hyperpolarized $[1-^{13}\text{C}]$ pyruvate MRSI. For cases where a standard treatment is ineffective, early assessment of therapeutic response is highly desirable to prompt alternative or salvage therapies or to improve end-of-life care. We have observed different early therapeutic responses assessed by changes in the Lac/Pyr ratio of tumour. All therapies produced unique changes in the Lac/Pyr ratio compared to the no-therapy control group. In contrast, therapeutic assessment using tumour volume showed a similar time-course to that assessed by Lac/Pyr ratio; yet, significant changes were not discernable until much later after therapy. Heterogeneous response to therapies observed in individual animals and across therapy groups was well characterized by hyperpolarized $[1-^{13}\text{C}]$ pyruvate MRSI. Lac/Pyr ratio measured across therapy groups was demonstrated to be correlated with tumour growth after initiation of therapy. Regional differences in Lac/Pyr ratio were compared with histology at endpoint and have been shown to be consistent with hypoxia. In conclusion, this study demonstrates the use of hyperpolarized $[1-^{13}\text{C}]$ pyruvate to probe real time tumour metabolism, which can provide a useful longitudinal non-invasive biomarker for assessment of therapeutic response.

3.5 Acknowledgements

The authors thank the laboratories of Dr. Paula Foster (specifically Drs. Yuanxin Chen and Amanda Hamilton) and Dr. Steven Kerfoot (Dr. Heather Craig) as well as Jennifer Hadway for initial help with our tumour model. We would also gratefully recognize funding from the Cancer Imaging Network of Ontario and the Ontario Institute for Cancer Research.

References for Chapter 3

1. Wen, P.Y. and S. Kesari, *Malignant gliomas in adults*. N Engl J Med, 2008. **359**(5): p. 492-507.
2. Ostrom, Q.T., et al., *CBTRUS Statistical Report: Primary Brain and Central Nervous System Tumors Diagnosed in the United States in 2008-2012*. Neuro Oncol, 2015. **17 Suppl 4**: p. iv1-iv62.
3. Li, J., et al., *The future role of personalized medicine in the treatment of glioblastoma multiforme*. Pharmgenomics Pers Med, 2010. **3**: p. 111-27.
4. Bradley, W.G., Jr., et al., *Comparison of CT and MR in 400 patients with suspected disease of the brain and cervical spinal cord*. Radiology, 1984. **152**(3): p. 695-702.
5. Mehta, A.I., et al., *Monitoring radiographic brain tumor progression*. Toxins (Basel), 2011. **3**(3): p. 191-200.
6. Wen, P.Y., et al., *Updated response assessment criteria for high-grade gliomas: response assessment in neuro-oncology working group*. J Clin Oncol, 2010. **28**(11): p. 1963-72.
7. Hanahan, D. and R.A. Weinberg, *Hallmarks of Cancer: The Next Generation*. Cell, 2011. **144**(5): p. 646-674.
8. Kroemer, G. and J. Pouyssegur, *Tumor cell metabolism: cancer's Achilles' heel*. Cancer Cell, 2008. **13**(6): p. 472-82.
9. Brahimi-Horn, M.C., J. Chiche, and J. Pouyssegur, *Hypoxia signalling controls metabolic demand*. Curr Opin Cell Biol, 2007. **19**(2): p. 223-9.
10. Gatenby, R.A. and R.J. Gillies, *Why do cancers have high aerobic glycolysis?* Nature Reviews Cancer, 2004. **4**(11): p. 891-899.
11. Kennedy, K.M. and M.W. Dewhirst, *Tumor metabolism of lactate: the influence and therapeutic potential for MCT and CD147 regulation*. Future Oncol, 2010. **6**(1): p. 127-48.
12. Mankoff, D.A., et al., *Tumor-specific positron emission tomography imaging in patients: [18F] fluorodeoxyglucose and beyond*. Clin Cancer Res, 2007. **13**(12): p. 3460-9.
13. Weber, W.A., N. Avril, and M. Schwaiger, *Relevance of positron emission tomography (PET) in oncology*. Strahlentherapie Und Onkologie, 1999. **175**(8): p. 356-373.

14. Ardenkjaer-Larsen, J.H., et al., *Increase in signal-to-noise ratio of > 10,000 times in liquid-state NMR*. Proc Natl Acad Sci U S A, 2003. **100**(18): p. 10158-63.
15. Chattergoon, N., et al., *Field dependence of T1 for hyperpolarized [1-13C]pyruvate*. Contrast Media Mol Imaging, 2013. **8**(1): p. 57-62.
16. Gallagher, F.A., M.I. Kettunen, and K.M. Brindle, *Biomedical applications of hyperpolarized C-13 magnetic resonance imaging*. Progress in Nuclear Magnetic Resonance Spectroscopy, 2009. **55**(4): p. 285-295.
17. Pinheiro, C., et al., *Role of monocarboxylate transporters in human cancers: state of the art*. J Bioenerg Biomembr, 2012. **44**(1): p. 127-39.
18. Phan, L.M., S.C. Yeung, and M.H. Lee, *Cancer metabolic reprogramming: importance, main features, and potentials for precise targeted anti-cancer therapies*. Cancer Biol Med, 2014. **11**(1): p. 1-19.
19. Tennant, D.A., R.V. Duran, and E. Gottlieb, *Targeting metabolic transformation for cancer therapy*. Nat Rev Cancer, 2010. **10**(4): p. 267-77.
20. Zhu, A., D. Lee, and H. Shim, *Metabolic positron emission tomography imaging in cancer detection and therapy response*. Semin Oncol, 2011. **38**(1): p. 55-69.
21. Strauss, L.G., *Fluorine-18 deoxyglucose and false-positive results: A major problem in the diagnostics of oncological patients*. European Journal of Nuclear Medicine, 1996. **23**(10): p. 1409-1415.
22. Ledezma, C.J., et al., *18F-FDOPA PET/MRI fusion in patients with primary/recurrent gliomas: initial experience*. Eur J Radiol, 2009. **71**(2): p. 242-8.
23. Lin, R.Y., et al., *Human monocarboxylate transporter 2 (MCT2) is a high affinity pyruvate transporter*. J Biol Chem, 1998. **273**(44): p. 28959-65.
24. Park, J.M., et al., *Metabolite kinetics in C6 rat glioma model using magnetic resonance spectroscopic imaging of hyperpolarized [1-(13)C]pyruvate*. Magn Reson Med, 2012. **68**(6): p. 1886-93.
25. Day, S.E., et al., *Detecting tumor response to treatment using hyperpolarized C-13 magnetic resonance imaging and spectroscopy*. Nature Medicine, 2007. **13**(11): p. 1382-1387.
26. Park, I., et al., *Detection of Early Response to Temozolomide Treatment in Brain Tumors Using Hyperpolarized C-13 MR Metabolic Imaging*. Journal of Magnetic Resonance Imaging, 2011. **33**(6): p. 1284-1290.

27. Witney, T.H., et al., *Detecting treatment response in a model of human breast adenocarcinoma using hyperpolarised [1-13C]pyruvate and [1,4-13C2]fumarate*. Br J Cancer, 2010. **103**(9): p. 1400-6.
28. Witney, T.H., et al., *A Comparison between Radiolabeled Fluorodeoxyglucose Uptake and Hyperpolarized C-13-Labeled Pyruvate Utilization as Methods for Detecting Tumor Response to Treatment*. Neoplasia, 2009. **11**(6): p. 574-U88.
29. Park, J.M., et al., *Hyperpolarized (13)C-lactate to (13)C-bicarbonate ratio as a biomarker for monitoring the acute response of anti-vascular endothelial growth factor (anti-VEGF) treatment*. NMR Biomed, 2016. **29**(5): p. 650-9.
30. Friesen-Waldner, L., et al., *Optimisation of dynamic nuclear polarisation of [1-(13)C] pyruvate by addition of gadolinium-based contrast agents*. J Magn Reson, 2012. **223**: p. 85-9.
31. Lim, H., et al., *Construction and evaluation of a switch-tuned (13) C - (1) H birdcage radiofrequency coil for imaging the metabolism of hyperpolarized (13) C-enriched compounds*. J Magn Reson Imaging, 2014. **40**(5): p. 1082-90.
32. Jensen, M.D., et al., *Implementation and commissioning of an integrated micro-CTRT system with computerized independent jaw collimation*. Med Phys, 2013. **40**(8): p. 081706.
33. Gibson, E., et al., *Registration of prostate histology images to ex vivo MR images via strand-shaped fiducials*. J Magn Reson Imaging, 2012. **36**(6): p. 1402-12.
34. Keeler, J., *Understanding NMR spectroscopy*. 2nd ed. 2010, Chichester, U.K.: John Wiley and Sons. xiii, 511 p.
35. Yushkevich, P.A., et al., *User-guided 3D active contour segmentation of anatomical structures: significantly improved efficiency and reliability*. Neuroimage, 2006. **31**(3): p. 1116-28.
36. Vander Heiden, M.G., *Targeting cancer metabolism: a therapeutic window opens*. Nat Rev Drug Discov, 2011. **10**(9): p. 671-84.
37. Grobбен, B., P.P. De Deyn, and H. Slegers, *Rat C6 glioma as experimental model system for the study of glioblastoma growth and invasion*. Cell and Tissue Research, 2002. **310**(3): p. 257-270.
38. Barth, R.F. and B. Kaur, *Rat brain tumor models in experimental neuro-oncology: the C6, 9L, T9, RG2, F98, BT4C, RT-2 and CNS-1 gliomas*. J Neurooncol, 2009. **94**(3): p. 299-312.
39. Vajkoczy, P., et al., *Characterization of angiogenesis and microcirculation of high-grade glioma: An intravital multifuorescence microscopic approach in the*

- athymic nude mouse*. Journal of Cerebral Blood Flow and Metabolism, 1998. **18**(5): p. 510-520.
40. Erdlenbruch, B., et al., *Alkylglycerol opening of the blood-brain barrier to small and large fluorescence markers in normal and C6 glioma-bearing rats and isolated rat brain capillaries*. Br J Pharmacol, 2003. **140**(7): p. 1201-10.
 41. Drevelegas, A., *Imaging of brain tumors with histological correlations*. 2nd ed. 2011, Berlin: Springer. x, 432 p.
 42. Graif, M., et al., *Contrast-enhanced MR imaging of malignant brain tumors*. AJNR Am J Neuroradiol, 1985. **6**(6): p. 855-62.
 43. Steen, R.G., *Edema and tumor perfusion: characterization by quantitative 1H MR imaging*. AJR Am J Roentgenol, 1992. **158**(2): p. 259-64.
 44. Becherer, A., et al., *Brain tumour imaging with PET: a comparison between [18F]fluorodopa and [11C]methionine*. Eur J Nucl Med Mol Imaging, 2003. **30**(11): p. 1561-7.
 45. Harada, M., et al., *Selection of endogenous 13C substrates for observation of intracellular metabolism using the dynamic nuclear polarization technique*. Jpn J Radiol, 2010. **28**(2): p. 173-9.
 46. Allouche-Arnon, H., et al., *In vivo magnetic resonance imaging of glucose - initial experience*. Contrast Media Mol Imaging, 2013. **8**(1): p. 72-82.
 47. Park, J.M., et al., *Measuring mitochondrial metabolism in rat brain in vivo using MR Spectroscopy of hyperpolarized [2-(1)(3)C]pyruvate*. NMR Biomed, 2013. **26**(10): p. 1197-203.
 48. Thind, K., et al., *Mapping metabolic changes associated with early Radiation Induced Lung Injury post conformal radiotherapy using hyperpolarized (1)(3)C-pyruvate Magnetic Resonance Spectroscopic Imaging*. Radiother Oncol, 2014. **110**(2): p. 317-22.
 49. Ulmer, S., et al., *Use of dynamic susceptibility-contrast MRI (DSC-MRI) to assess perfusion changes in the ipsilateral brain parenchyma from glioblastoma*. Journal of Neuro-Oncology, 2009. **91**(2): p. 213-220.
 50. Norden, A.D. and P.Y. Wen, *Glioma therapy in adults*. Neurologist, 2006. **12**(6): p. 279-92.
 51. Frosina, G., *DNA repair and resistance of gliomas to chemotherapy and radiotherapy*. Mol Cancer Res, 2009. **7**(7): p. 989-99.

52. Lammers, T., et al., *Effect of radiotherapy and hyperthermia on the tumor accumulation of HPMA copolymer-based drug delivery systems*. J Control Release, 2007. **117**(3): p. 333-41.
53. Jain, R.K., *Normalization of tumor vasculature: an emerging concept in antiangiogenic therapy*. Science, 2005. **307**(5706): p. 58-62.
54. Stepanenko, A.A., et al., *Temozolomide promotes genomic and phenotypic changes in glioblastoma cells*. Cancer Cell Int, 2016. **16**: p. 36.
55. Zhang, Y.H., et al., *Temozolomide/PLGA microparticles: a new protocol for treatment of glioma in rats*. Med Oncol, 2011. **28**(3): p. 901-6.
56. Stupp, R., et al., *Radiotherapy plus concomitant and adjuvant temozolomide for glioblastoma*. N Engl J Med, 2005. **352**(10): p. 987-96.

Chapter 4

4 Longitudinal Measurement of Intra- and Extracellular pH gradient in a Rat Model of Glioma

*Heeseung Lim, Mohammed Albatany, Francisco Martínez-Santesteban, Robert Bartha
and Timothy J. Scholl*

An updated version of the following chapter will be submitted to Tomography as a journal manuscript.

4.1 Introduction

Cancer is a physiologically and genetically diverse disease resulting in abnormal cellular proliferation. Cancer cells have altered biological pathways and microenvironment that support this proliferation. These changes have been widely studied and some categorized as *hallmark* features of cancer because they are common to many types of genetically diverse tumours.[1] These hallmark features impact on important aspects of cancer progression and therapy. Among the identified hallmarks, the deregulation of metabolism and poor vascularization are main contributors to altered intra- and extracellular pH within tumours.[1-4] Altered tumour pH, in particular the intracellular to extracellular pH gradient, is an important factor that drives cancer progression, by enhancing oncogene expression, increasing metastatic potential, and altering drug efficacy.[5, 6]

The cellular pH gradient is defined as the difference between intracellular pH (pH_i) and extracellular pH (pH_e). In normal tissue, pH_i is ~ 7.2 and pH_e is ~ 7.4 , [7-9] resulting in a negative pH gradient (~ -0.2) across the cellular membrane. In contrast, tumour cells possess a positive pH gradient (~ 0.5), where pH_i is ~ 7.4 and pH_e is ~ 6.9 . [7, 8, 10-12] This reversal of the pH gradient is the result of modified cellular metabolism, which promotes tumour cell growth and invasion. As most tumour cells favor anaerobic metabolism over aerobic metabolism, even with the presence of oxygen (Warburg effect), the rate of glycolysis and lactic acid production is increased.[4] Significant decreases in intracellular pH due to accumulation of metabolic acids, would normally damage a cell,

but tumour cells actively maintain homeostasis by transporting protons into the extracellular space.[13] Inefficient tumour vasculature is not able to completely support the bicarbonate/carbon dioxide buffer system so that the extracellular space of tumour becomes more acidic.[13] This leads to destruction of the extracellular matrix, promoting tumour cell invasion and eventually metastasis.[7] The tumour pH gradient is further increased as the tumour becomes hypoxic and the vasculature fails to provide sufficient buffers. [14] Non-invasive measurement of the tumour pH gradient would aid in treatment planning and evaluating treatment response.

Several non-invasive imaging techniques have been developed to quantify intra- and extracellular tissue pH.[10] In this study, intracellular tissue pH was measured using a novel chemical exchange saturation transfer (CEST) magnetic resonance imaging (MRI) technique called amine and amide concentration-independent detection (AACID).[15] This method exploits the differential pH dependence of the exchange rate of amine and amide protons with bulk water to measure pH. A CEST image is produced to determine the ratio of the amine to amide CEST effect, which can be converted into a measurement of intracellular pH from a separate calibration.[15] Extracellular tissue pH was measured with hyperpolarized ^{13}C magnetic resonance spectroscopic imaging (MRSI). The use of ^{13}C -labelled bicarbonate as a contrast agent to evaluate pH_e was previously reported in the literature.[16] Hyperpolarized ^{13}C bicarbonate is injected into the vasculature and after circulation reaches the tissue of interest where it exchanges with the pre-existing bicarbonate/carbon dioxide pool under carbonic anhydrase activity. Extracellular pH can be derived from the Henderson-Hasselbalch equation using the ratio of ^{13}C bicarbonate and $^{13}\text{CO}_2$ measured by ^{13}C MRSI. By serially combining these approaches, the pH gradient of tissue can be mapped and quantified in the same pre-clinical model.

This study followed the progression of the pH gradient of tumour cells in an untreated orthotopic rodent model of glioma. C6 rat glioma tumours exhibit rapid growth, vascularization and invasion.[17] Previous studies have noted that these tumours develop necrotic cores and exhibit regional hypoxia.[17, 18] Adequate vascularization facilitates effective delivery of hyperpolarized ^{13}C bicarbonate to the tumour. For this aggressive

tumour model, significant changes in the pH gradient are expected over time, making it an ideal solid tumour model for longitudinal studies of tumour pH.

The purpose of the study was to measure and characterize longitudinal changes in the tumour pH gradient. There have been several studies measuring pH of tissue using techniques as described above.[15, 16, 19-21] However, no longitudinal study exists measuring both pH_e and pH_i in a consecutive fashion to map regional differences and temporal changes in pH gradient in an untreated tumour. We hypothesized that the pH gradient would increase over time as the tumour increased in size. Knowledge of pH gradient is vital for tumour characterization and selecting appropriate therapy, since the outcome of therapy can be dependent on pH. The results of this study provide insight regarding changes in tumour pH linked to aggressive growth.

4.2 Methods

4.2.1 ^{13}C Bicarbonate Sample Preparation

95% enriched ^{13}C cesium bicarbonate (Sigma Aldrich, Miamisburg OH, U.S.A.) was dissolved in a 4:1 glycerol and deuterium oxide mixture at a final concentration of 6.3 mol/L. In addition, OX63 trityl radical (Oxford Instruments, Concord MA, U.S.A.) and ProHance gadolinium contrast agent (Bracco Diagnostics, Monroe Township, NJ, U.S.A.) were added to the sample at final concentrations of 25 mmol/L and 0.5 mol/L respectively. The final mixture was heated to 60°C and stirred to dissolve. The resulting bicarbonate preparation was stored at -4°C for later use.

4.2.2 Hyperpolarization

^{13}C cesium bicarbonate was hyperpolarized using dynamic nuclear polarization (DNP) (HyperSense, Oxford Instruments, Abingdon, UK). The bicarbonate sample was cooled to 1.4 K at 3.3 T in the DNP apparatus and irradiated with 50 mW of microwave radiation at a frequency of 94.123 GHz to transfer electronic spin magnetization to the ^{13}C -labelled bicarbonate. Approximately 90% solid state polarization was achieved during two hours of hyperpolarization. The sample was rapidly mixed with a superheated mixture of 80-mmol/L phosphate buffer (pH = 7.2) and 100-mg/L

ethylenediamine tetra-acetic acid disodium salt dehydrate (EDTA, Sigma-Aldrich, St. Louis MO, U.S.A.). The resulting hyperpolarized solution had a ^{13}C bicarbonate concentration of 150 mmol/L and a pH of 7.4 at 37°C. The *in vitro* spin lattice relaxation time and polarization values of the ^{13}C nucleus were 26.2 ± 1.4 s and $\sim 7.5\%$ measured at 3 T.[22]

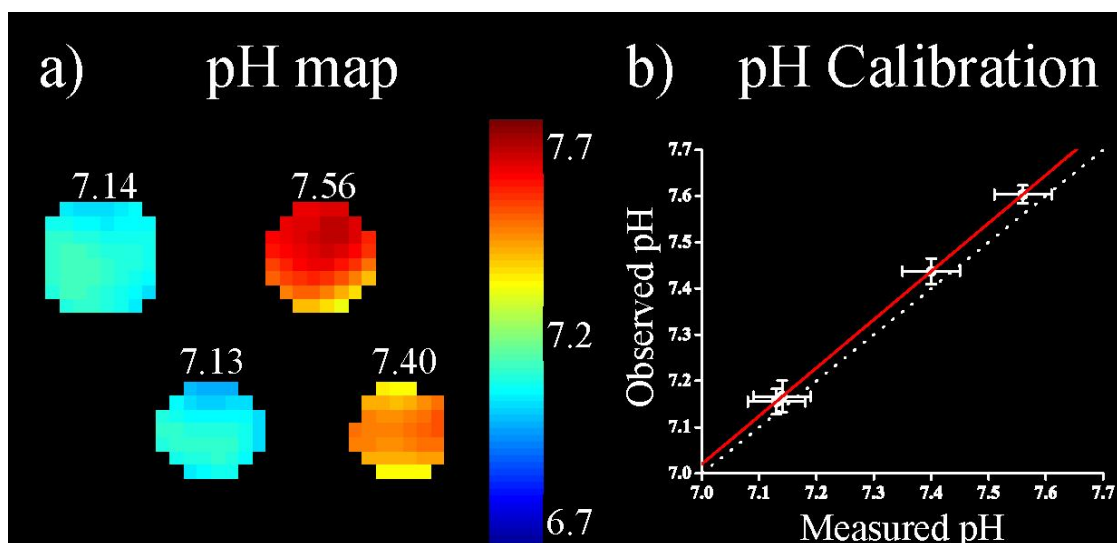


Figure 4-1 Calibration data for different pH-buffered solutions mixed with hyperpolarized ^{13}C bicarbonate. a) A pH map derived from ^{13}C MRSI and the corresponding pH values obtained by pH meter. b) The linear regression between measured pH (pH meter) and observed pH (hyperpolarized ^{13}C bicarbonate) with $R^2 = 1$.

4.2.3 Phantom Imaging

To calibrate pH measurement from hyperpolarized ^{13}C bicarbonate, four separate phosphate buffers with different pH values (6.4, 6.6, 6.8, 7.0) were prepared prior to the experiments. One milliliter of each phosphate buffer was mixed with an equal volume of 200 mmol/L buffered hyperpolarized ^{13}C bicarbonate solution. For catalysis, 1 mg of carbonic anhydrase (Sigma Aldrich, Miamisburg OH, U.S.A.) corresponding to ~ 2500 Wilbur-Anderson units, was added to each solution as a catalyst. The resulting mixtures were imaged with MRSI at 3 T (General Electric Healthcare Discovery MR750 3.0 T, Milwaukee WI, U.S.A.). Immediately after imaging, the pH of each mixture was

recorded using a pH meter (VWR Symphony SB70P digital bench-model pH meter, VWR International, Mississauga ON, Canada)

4.2.4 Animal Model

A total of 7 Wistar rats weighing approximately 250 g (~5 to 7 weeks old), were used in this study. On day zero, animals were surgically implanted with approximately one million C6 rat glioma cells in the right caudate nucleus of the brain. Animals were scanned on days 8, 12 and 15. CEST was performed first using a 9.4 T small animal MRI scanner (Agilent, Santa Clara, CA) to measure pH_i . Under anesthesia, the animals were then transferred to the same 3 T MRI for hyperpolarized ^{13}C MRSI to determine pH_e . All animal procedures were performed in accordance with relevant guidelines and regulations stipulated by an animal use protocol approved by the University Council on Animal Care, Animal Use Subcommittee at Western University.

4.2.5 Chemical Exchange Shift Imaging for Intracellular pH

CEST imaging on the 9.4T MRI was performed with a 50-mm-diameter volume birdcage coil built in-house. Standard anatomical T_2 -weighted images were used for tumour localization. The T_2 -weighted images were acquired using a 2D fast spin-echo pulse sequence (FSE) with the following parameters: field of view (FOV) = 38.4×38.4 mm, 0.3-mm isotropic in-plane resolution, slice thickness = 1 mm, repetition time (TR) = 3000 ms, echo time (TE) = 10 ms, echo train length (ETL) = 4, and effective TE = 40 ms. Upon initial tumour detection by MRI, two slices from the T_2 -weighted image data with maximum tumour extent were selected for CEST imaging. Three sequential CEST images were acquired using an FSE sequence with the following parameters: FOV = 38.4×38.4 mm, 0.6-mm in-plane resolution, slice thickness = 2 mm, TR = 7000 ms, TE = 7 ms, ETL = 32, effective TE = 7 ms and preceded by a continuous RF pulse with an amplitude of 1.5 μT and duration of 4s. CEST images were acquired at different saturation frequencies (1.2 to 4.5 ($\Delta=0.1$) ppm, from 5.4 to 6.6 ($\Delta=0.1$) ppm, -1000 and 1000 ppm images were acquired as reference, producing a total of 49 images). For B_0 correction, a water saturation shift referencing (WASSR) technique was used.[23] A linearly spaced 37-point WASSR CEST spectrum with saturation frequencies from -0.6

to 0.6 ppm was acquired using the same pulse sequence except preceded by a shorter duration RF saturation pulse (100 ms) with low amplitude (0.2 μ T). Each WASSR spectrum and CEST spectrum was interpolated to achieve 1-Hz resolution. Each CEST spectrum was then frequency shifted, using the corresponding WASSR spectrum, to account for B_0 variation. B_0 variations were corrected on a pixel-by-pixel basis. The three CEST spectra were summed for each pixel following B_0 corrections to increase signal to noise ratio. A B_1 field map was generated using a flip-angle imaging (FAI) pulse sequence (TR = 20 ms, TE = 3.47 ms, echoes = 2, flip-angle = 700, FOV = 38.4 \times 38.4 mm², matrix size = 64 \times 64). Observed B_1 variations in the CEST slice were less than 5%, and no B_1 correction was applied.

4.2.6 Hyperpolarized ¹³C Bicarbonate MRSI for Extracellular pH

A switch-tuned ¹H - ¹³C RF coil was used to acquire inherently co-registered proton images and ¹³C MRSI data of the rat models.[24] Tumours were identified using a T_2 -weighted anatomical ¹H scan of the rat brain using a FSE sequence with the following parameters: 80.0 \times 80.0 mm FOV, 0.3-mm isotropic in-plane resolution, 3-mm slice thickness, TR = 4000 ms, TE = 85 ms, bandwidth = 10.42 kHz, ETL = 16, and number of averages = 4. Prior to hyperpolarized ¹³C imaging, rats were injected with 3 ml of buffered hyperpolarized ¹³C bicarbonate solution in a single twelve-second bolus through a tail vein catheter. Dynamic ¹³C maps of bicarbonate and carbon dioxide were collected using a spectral-spatial excitation chemical shift imaging sequence (FIDALL[25]) with the following parameters: two frequency excitations (bicarbonate and CO₂, 35.5 ppm difference), 60.0 \times 60.0 mm FOV, 3.5 mm isotropic in-plane resolution, slice thickness ~12 mm, TR = 350 ms, and 5°/90° flip angle for bicarbonate/CO₂ excitation.

4.2.7 Data analysis

Data analysis of the CEST and hyperpolarized ¹³C bicarbonate MRSI was performed using MATLAB (Mathworks, Natick, MA, USA). Using B_0 -corrected and smoothed CEST spectra, AACID values were measured on a voxel-by-voxel basis. AACID data represent the ratio of the CEST effects of amine protons resonating at 2.75 ppm and amide protons at 3.50 ppm, normalized by magnetization transfer effects measured after

saturation at 6.0 ppm and are calculated using the following equation from McVicar *et al.*: [15]

$$\text{AACID} = \frac{M_z(3.50 \text{ ppm}) \times (M_z(6.00 \text{ ppm}) - M_z(2.75 \text{ ppm}))}{M_z(2.75 \text{ ppm}) \times (M_z(6.00 \text{ ppm}) - M_z(3.50 \text{ ppm}))} \quad \text{Equation 4-1}$$

Here, $M_z(f)$ is the magnitude of the CEST signal at a specific frequency, f . AACID is linearly-dependent on pH_i and is insensitive to change in T_1 relaxation time, temperature, and macromolecule concentration. [15] We calibrated the relationship between AACID and pH in both tumour and contralateral brain ROIs. For hyperpolarized ^{13}C bicarbonate MRSI, non-Cartesian k -space data were reconstructed into maps of ^{13}C -bicarbonate and ^{13}C -carbon dioxide. [26] Regional pH was calculated using the Henderson-Hasselbalch equation: [27]

$$\text{pH}_e = \text{p}k_a + \log_{10} \frac{[\text{HCO}_3^-]}{[\text{CO}_2]} \quad \text{Equation 4-2}$$

Here, pH_e is the extracellular pH, $\text{p}k_a$ (6.17) [27] is the base-10 logarithm of the acid dissociation constant of carbonic acid and $[\text{HCO}_3^-]$ and $[\text{CO}_2]$ are the concentrations of bicarbonate and carbon dioxide respectively. The concentration ratio of bicarbonate to carbon dioxide is determined as the ratio of MRSI signal amplitudes of ^{13}C -bicarbonate and ^{13}C -carbon dioxide after corrections for individual flip angle excitations.

4.2.8 Statistics

The region of interest (ROI) for tumour and contralateral brain tissues were manually segmented on both 3T and 9.4T T_2 -weighted images using ITK-Snap (www.itksnap.org, [28]) prior to any image registration. From ROIs, tumour volumes were measured and inter-observer variability was used for the volume error. For each animal and time point, the mean and standard deviation for pH_i and pH_e were calculated from these ROIs (SPSS, IBM Corp., Armonk, NY USA). All pH errors represent one standard deviation of the weighted mean value. The statistical significant across pH_i & pH_e and each day were tested using an analysis of variance (ANOVA) with Tukey's *post hoc* test and weighted data using the standard deviation of pH measurements. The correlation between pH gradient and tumour volume was tested using Pearson correlation.

4.2.9 Histology

At the experimental endpoint, animals were sacrificed and perfused with 4% paraformaldehyde (Sigma Aldrich, Miamisburg OH, U.S.A). Perfused rat brains were paraffin embedded and sectioned to 5- μ m-thick slices. Then rat brain slices containing tumour were stained with hematoxylin & eosin (H&E), Ki67 and HIF1 α . These slices were scanned with an AxioImager Z1 Upright Microscope (Carl Zeiss Canada, North York, ON, Canada). Those images were subsequently co-registered with the T_2 -weighted MR images acquired at 3T using Slicer (Version 4.31, Surgical Planning Laboratory, Brigham & Women's Hospital Boston MA, U.S.A.) with a custom software plugin.[29]

4.3 Results

Seven Wistar rats were used in this study; five animals survived to the last imaging time point. The other two animals were sacrificed before the final imaging time point because of neurological impairment related to tumour volume. All animals showed aggressive tumour growth throughout the study, which is an expected feature of the C6 glioma model.[17]

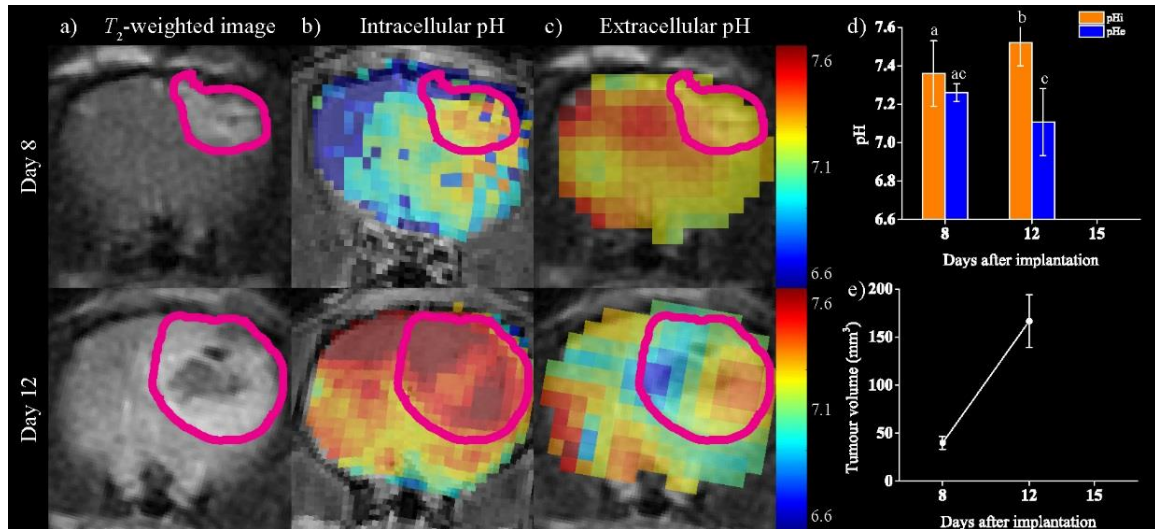


Figure 4-2 The progression of intra- and extracellular pH of a representative C6 glioma. Panels a) b) and c) present the T_2 -weighted images, and intra- and extracellular pH maps of the rat brain at days 8 and 12. Tumours are contoured in magenta. d) Quantification of changes of intra- and extracellular tumour pH. Statistical significance is annotated with letters (measurements with different letters are significant at $p < 0.05$). e) Longitudinal tumour volume measurements. Inter-observer variability was used for the error bar. A large region of necrosis within the tumour is evident on day 12 in panel a). This animal was sacrificed prior to the final imaging time point on day 15 due to neurological impairment.

Two animals from the cohort were chosen to demonstrate the observed changes in pH gradient of tumour cells. The first representative animal is shown in Figure 4-2. This animal did not survive to the final imaging time point but was scanned on days 8 and 12. Rapid tumour growth is evident by inspection of Figure 4-2a and quantified in Figure 4-2e. At day 12, the dark region within the tumour boundary on the T_2 -weighted image was indicative of extensive necrosis. Maps of pH_i and pH_e at both imaging time points are provided for comparison in Figures 4-2b and 4-2c and the average pH_i and pH_e for the tumour is provided in Figure 4-2d. There was a statistically significant difference ($p < 0.05$) between pH_i and pH_e of the tumour at day 12. There was also a significant increase in pH_i of the tumour ($p < 0.05$) between days 8 and 12. However, there was no significant change in pH_e of the tumour ($p \sim 0.11$). A second representative case is shown in Figure

4-3. This animal was scanned on days 8, 12 and 15 prior to sacrifice. This animal also exhibited a rapidly growing tumour as shown in Figure 4-3a and quantified in Figure 4-3e. Again, pH_i and pH_e maps of the rat brain are shown in Figure 4-3b and c and average pH_i and pH_e of the tumour are graphed in Figure 4-3d. Only at day 12 and 15, there was a statistically significant difference ($p < 0.05$) between pH_i and pH_e within the tumour. Tumour necrosis was not evident with T_2 -weighted MRI. Increased pH_i within the tumour was only significant ($p < 0.05$) at day 15. The pH_e of the tumour was significantly decreased ($p < 0.05$) at day 12 compared to day 8 but increased again by day 15.

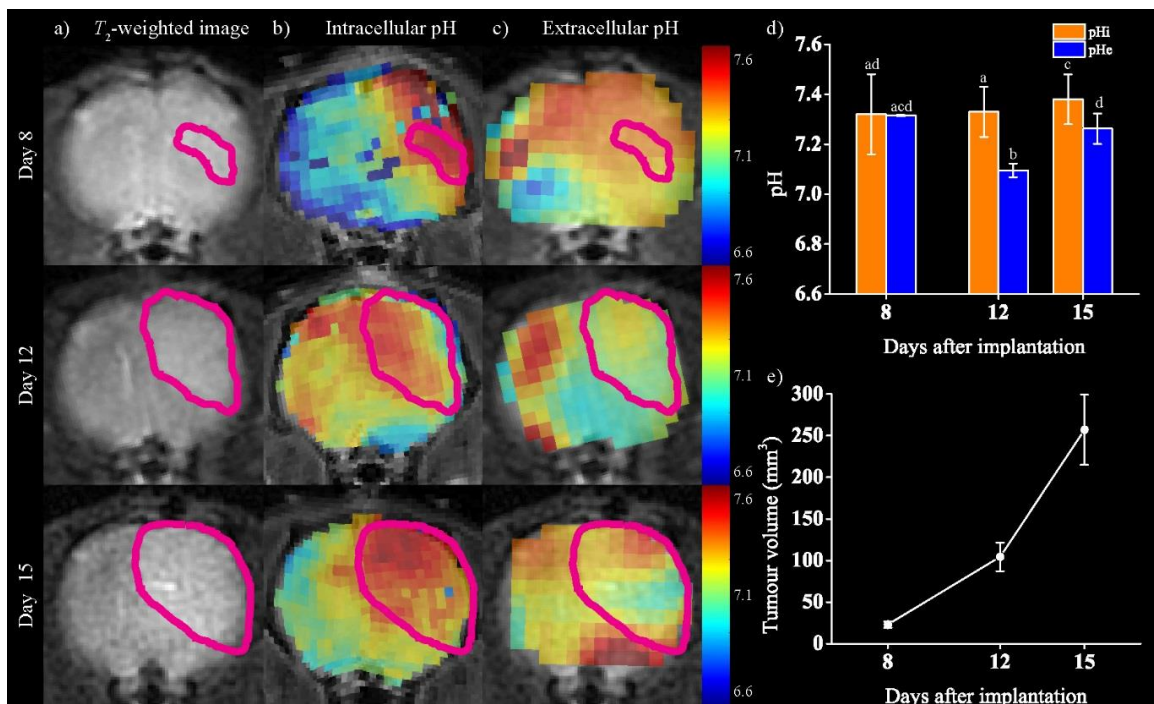


Figure 4-3 The progression of intra- and extracellular pH of a representative C6 glioma. Panels a) b) and c) present the T_2 -weighted images, and intra- and extracellular pH maps of the rat brain at days 8, 12 and 15. Tumours are contoured in magenta. d) Quantification of changes of intra- and extracellular tumour pH. Statistical significance is annotated with letters. e) Longitudinal tumour volume measurements. Inter-observer variability was used for the error bar.

Longitudinal changes in average pH gradient and tumour volume of all animals are shown in Figure 4-4. Figure 4-4a shows the average pH_i of tumours and contralateral

brain on days 8, 12 and 15. Between days, there was no significant difference for measured pH_i within either tumour or contralateral brain tissue; however, tumour pH_i was significantly larger ($p < 0.05$) than contralateral brain at all days. Similarly, Figure 4-4b shows the average pH_e of tumours and contralateral brain on days 8, 12 and 15. There was no significant difference detected on day 8 between tumour and contralateral tissue. However, there were significant reductions ($p < 0.05$) in tumour pH_e on day 12 and 15 and a significant increase ($p < 0.05$) in contralateral brain pH_e on day 15. Significant differences between tumour and contralateral brain pH_e were observed on day 12 and 15. Figure 4-4c illustrates the comparison between pH gradients in tumours and contralateral brain tissue on days 8, 12 and 15. The pH gradient within tumours increased significantly over the three imaging time points ($p < 0.05$). The pH gradient for contralateral brain regions did not change significantly over this period but was consistently less than that observed within the tumours. Lastly, figure 4d shows the average tumour volume for days 8, 12 and 15. Tumour volumes significantly increased ($p < 0.05$) between imaging time points.

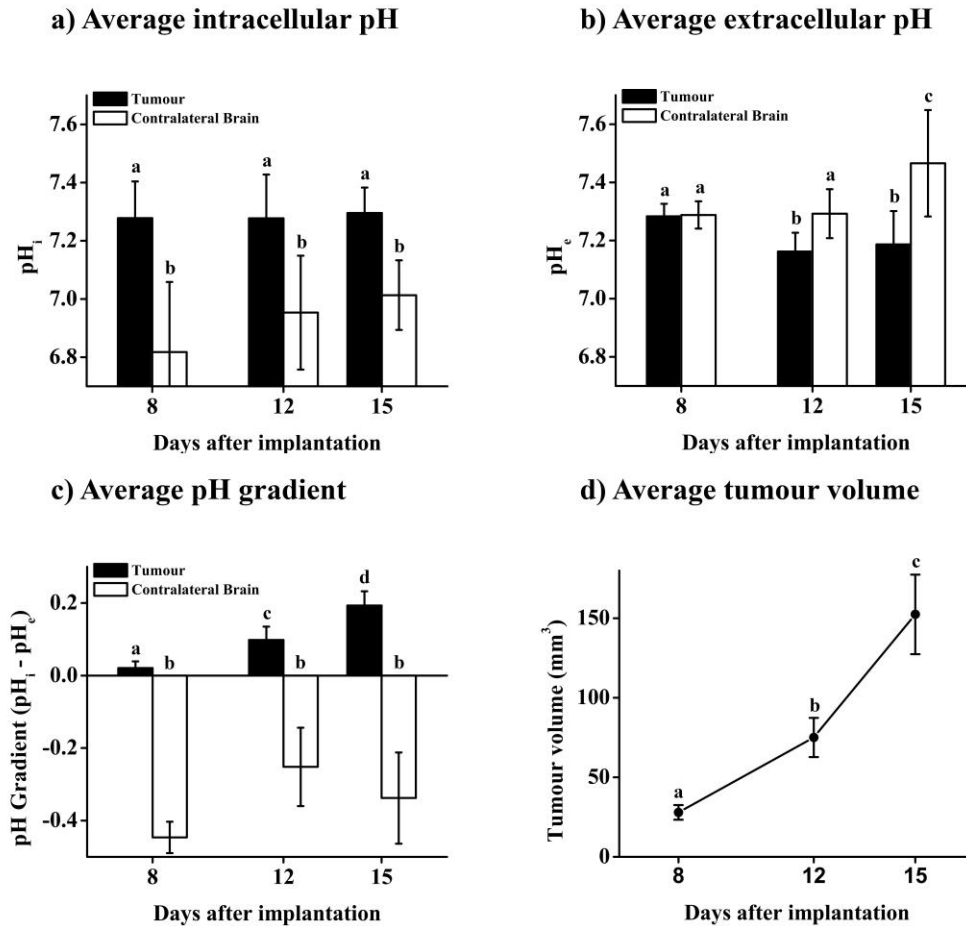


Figure 4-4 Longitudinal changes in cohort-averaged pH measurements. Panel a) & b) shows intra- and extracellular pH in tumour and contralateral brain measured on days 8, 12 and 15. Panel c) compares cellular pH gradient between tumour and contralateral brain at those same days. d) Average gross tumour volume measured from T_2 -weighted imaging data. Inter-observer variability was used for the error bar. All statistical significances ($p < 0.05$) are annotated with letters.

The association between tumour volume and pH gradient is plotted in Figure 4-5. Averaging over all animals and time points, there was no significant correlation ($p \sim 0.26$). However, when tumours with extensive necrosis were excluded, tumour volume was correlated with pH gradient ($p < 0.05$) with a 0.715 Pearson coefficient.

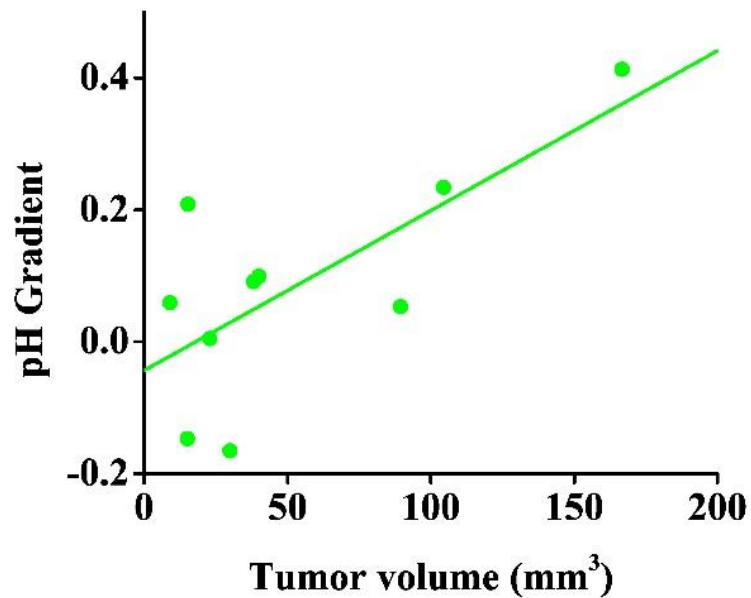


Figure 4-5 Correlation plot comparing pH gradient and tumour volume. Tumours that did not exhibit necrosis show a significant correlation (green line) between pH gradient and tumour volume ($p < 0.05$, Pearson correlation = 0.72).

Histology for the second representative animal case is shown in Figure 4-6 with corresponding pH and imaging data. The T_2 -weighted image showed no clear sign of necrosis; however, necrotic parts of tumour were clearly distinguished from non-necrotic parts by histology. The whole tumour region showed a relatively high pH_i and low pH_e compared to contralateral brain tissue. H&E staining revealed an extremely high density of cells within the tumour compare to normal brain. Further, necrosis was formed within the core of the tumour. HIF-1 showed a higher expression in tumour compared to brain tissue except within the necrotic region of brain. Similarly, Ki-67 staining showed greater cellular proliferation in the tumour and no proliferation within the necrotic core and the brain tissue surrounding the tumour.

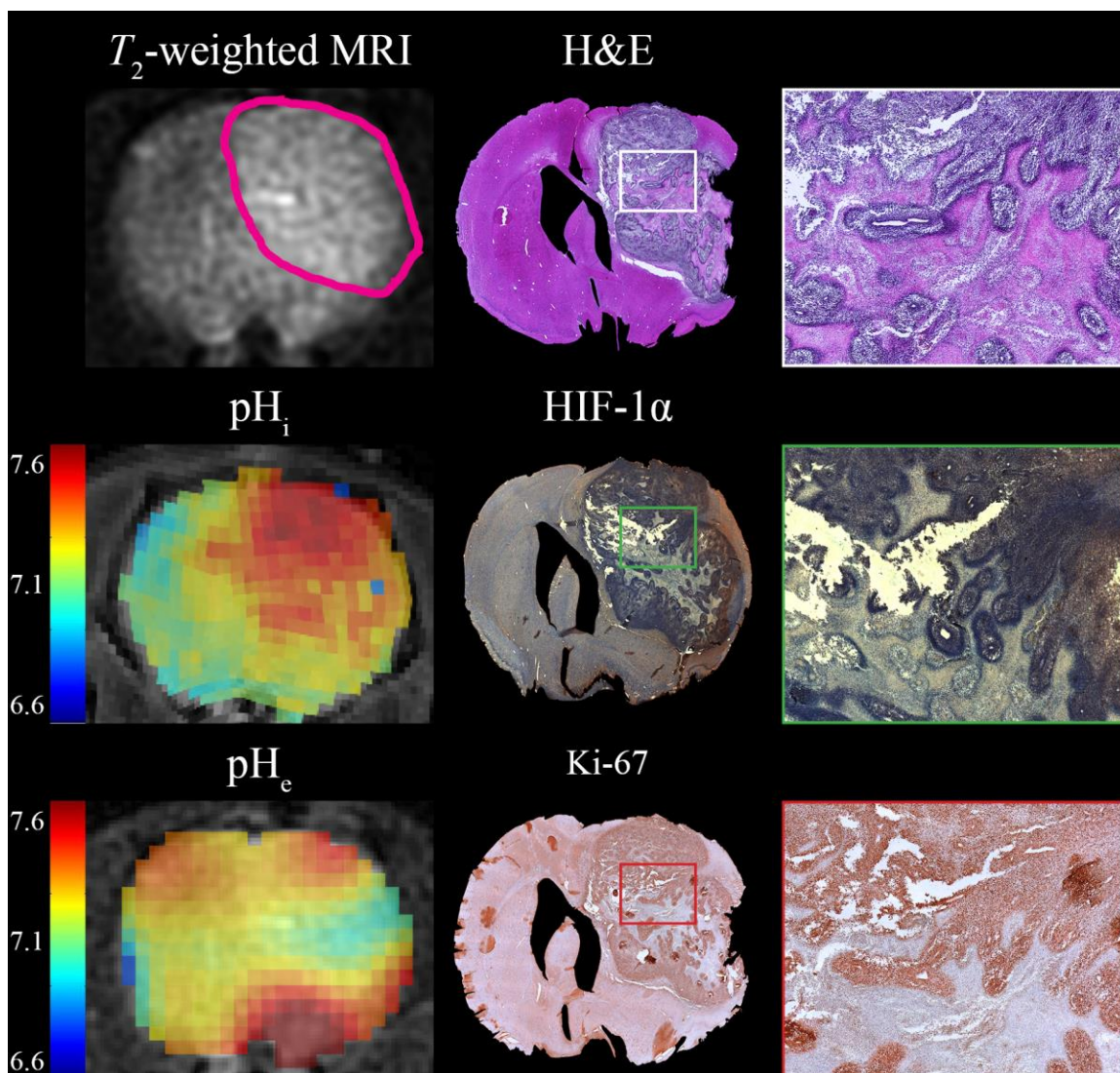


Figure 4-6 Histology of the 2nd representative animal shown in Figure 4-3. The first column presents the tumour extent, pH_i and pH_e within the rodent brain. The tumour margin is outlined in magenta. The second column contains histology including H&E, HIF-1 α and Ki-67 staining of tumour and brain tissue. The third column of images contains magnified histology of the regions outlined by respective boxes in column 2.

4.4 Discussion

The purpose of this longitudinal study was to map and quantify the change in tumour pH gradient using a rodent model of glioma. To the best of our knowledge, this is the first study to sequentially measure both pH_i and pH_e at multiple time points during tumour

progression in an *in vivo* model. This enabled a direct calculation of the cellular pH gradient within the tumour and surrounding tissue. Knowledge of changes in cellular pH gradient in tumours may be important for understanding biological changes in tumours (metabolism, vascularization and proliferation) and informing on possible treatment strategies (chemo- and radiotherapies).[8, 11]

The C6 rat glioma is a highly proliferating and aggressive solid tumour.[17] Tumour volumes increase rapidly as seen in Figures 4-2, 4-3 and 4-4. Tumour imaging in some animals suggested necrotic cores as shown in Figure 4-2a, which were confirmed by histology (see Figure 4-6). Changes in tumour volume have been correlated to alterations in tumour pH.[30] Hence, dynamic changes in tumour pH were expected commensurate with tumour growth. Due to rapidly increasing tumour volumes, some animals did not survive to the study endpoint. For animals with rapidly growing tumours, a reversal of pH was expected as well as a correlation between tumour growth rate and change in tumour pH.

In general, pH_i and pH_e within tumours and contralateral brain tissue were observed to largely match what has been previously reported in literature. As shown in Figure 4-4a, at day 15, tumour pH_i (7.30 ± 0.09) and tumour pH_e (7.19 ± 0.11) were similar to previously reported values ($\text{pH}_i \sim 7.4$ and $\text{pH}_e \sim 6.9$)[7, 8, 10-12]. Similarly, measurements in contralateral brain tissue, ($\text{pH}_i = 7.01 \pm 0.12$ and $\text{pH}_e = 7.46 \pm 0.18$) were also comparable to previously reported values ($\text{pH}_i \sim 7.2$ and $\text{pH}_e \sim 7.4$)[7-9]. In addition, these *in vivo* measurements confirmed the change in pH gradient direction for tumour cells compared to those in contralateral brain tissue. However, it should be noted that the contralateral brain does not represent ideal normal tissue. Elevated intracranial pressure due to the large tumour burden would likely have an impact on brain tissue pH.[31] Although the contralateral brain region did exhibit a consistently negative pH gradient, this region of brain would likely have been influenced by intracranial hypertension and inflammation.[32] Measurements of the pH gradient ($\text{pH}_i - \text{pH}_e$) were observed to change sign as early as day 8 in tumours. This was approximately the earliest time point where tumour detection by MRI was reliable for this model.

For each animal, longitudinal measurements of pH_e and pH gradient within the tumour showed a significant decreasing and increasing trend (respectively) as illustrated in Figures 4-2d, 4-3d. However, the averaged pH_i for all tumours did not show any significant trend in time. The trend in tumour pH_e suggests acidification of extracellular space while the pH_i of tumour cells remains constant during tumour progression. These pH changes are a likely reason for the increase in tumour invasion and proliferation. Conversely contralateral brain tissue showed no significant change until day 15 when tumours had invaded the other hemisphere of the brain. At this last time point, contralateral brain tissue was able to maintain pH_i , but pH_e homeostasis was no longer balanced perhaps as a result of increased edema and reduced perfusion.

These tumours exhibited a large heterogeneity in pH_i and pH_e as demonstrated in Figures 4-2 and 4-3. These variations could be due to several biological factors. During tumour progression, tumour metabolism undergoes extensive modification, but these metabolic changes are often not homogenous.[33] Furthermore, the decrease in tumour pH_e induces inefficient and non-uniform vascularization[34] leading to further regional variation of pH_i and pH_e . [35] Secondly, at the final time point, some tumours possessed necrotic cores as shown in the histology of Figure 4-6. This can occur since C6 gliomas often form a necrotic core as a result of rapid tumour growth and limited supply of nutrients.[17] After the tumour cell undergoes necrosis, the integrity of the cellular membrane is jeopardized and there is no longer a valid distinction between intracellular and extracellular space.[36] Therefore, pH_i and pH_e measurements in regions of necrosis would not properly represent tumour pH gradient. In this study, tumour necrosis could not be reliably defined with T_2 -weighted images. Furthermore, with limited imaging resolution and contrast, it was often difficult to identify necrotic regions prior to experimental endpoint with histology. Never-the-less, the reversal of pH gradient was observed at all time points when measurements were averaged over the entire tumour volume identified by T_2 -weighted imaging even though pH measurements were not statistically significant changing across time points.

For individual animals, the change in cellular pH gradient within the tumour was readily apparent. Figure 4-2 presents a representative animal that died prior to the final imaging

time point. For this case, the tumour grew exceptionally fast such that the animal suffered significant weight loss and dehydration. Furthermore, rapid tumour growth led to necrosis, which was observed as a hypo-intense region within the tumour boundary on the T_2 -weighted image (Figure 4-2a). This was later confirmed as necrosis by histology. For tumour regions where increasing pH_i and decreasing pH_e was observed, this was likely a consequence of the tumour cells adapting to their microenvironment.[13] This tumour also showed heterogeneous pH_i and pH_e throughout the tumour at day 12, particularly in regions where necrosis was suspected compared to the non-necrotic portion of the tumour. This emphasizes the dynamic changes in both tumour pH_i and pH_e . Figure 4-3 showed another representative case in which the animal survived to the last imaging time point. Unlike the previous case, longitudinal changes in tumour volume, pH_i and pH_e were less substantial. In this case, pH_e was significantly decreased for day 12 compare to day 8 but significantly increased at day 15. Importantly, this tumour was later confirmed to have a substantial necrotic region by histology (see Figure 4-6), which is likely a factor for the larger range of regional pH measurements. Using only T_2 -weighted image data, it would be difficult to appreciate the full extent of the heterogeneity of the tumour and its environment. Regional maps of pH_i and pH_e facilitate the visualization of molecular and cellular changes linked to tumour progression in an individual animal.

A modest but significant correlation between tumour volume and pH gradient was observed for this cohort (Figure 4-5). This correlation was only significant ($p < 0.05$) when necrotic tumours were excluded. This correlation between tumour volume and pH has been previously reported and that studies suggested a similar conclusion.[30, 37] This correlation may explain increased tumour proliferation and invasion due to changes in tumour microenvironment linked to pH.

The histology in Figure 4-6, further illustrates the effects of regional tumour pH. Regional differences in pH_i and pH_e compared to contralateral brain corresponded well to the distribution of HIF-1 α and Ki-67 measured by histology. In glioma, HIF-1 α is upregulated and further induces metabolic remodeling.[38] Ki-67 is a marker for cellular proliferation. Thus, this histology finding demonstrates a potential link between tumour pH gradient, hypoxia and proliferation. Tumour heterogeneity is also speculated in both

the pH maps and histology. The ability to detect and measure tumour proliferation is important for the prognosis of these tumours. In addition, *a priori* knowledge of tumour pH may be valuable for choice of appropriate chemotherapy.

In conclusion, this paper has demonstrated longitudinal mapping of pH_i and pH_e in a rodent model of glioma. This is the first demonstration of non-invasive consecutive *in-vivo* measurement of pH_i and pH_e at multiple time points during tumour progression. This study has shown that within a single tumour, there is a significant regional variation of both pH_i and pH_e within tumour at a single time point. When these measurements were averaged for all animals at each time point, there was no statistically significant difference across time points. A statistical correlation between tumour volume and pH gradient was observed for non-necrotic tumours. Highly proliferative regions of the tumour can be observed by histology were associated with positive pH gradient. Regional molecular information such as pH_i and pH_e provide important information about longitudinal changes in the tumour environment. Knowledge of these changes may ultimately be useful to guide therapeutic choice for treatment of GBM or to assess treatment efficacy.

4.5 Acknowledgements

The authors would like to also recognize the contributions of Yuanxin Chen (histology), Alex Li (acquisition of 9.4 T CEST data) and Miranda Bellyou (animal preparation and handling) to this research.

References for Chapter 4

1. Hanahan, D. and R.A. Weinberg, *Hallmarks of Cancer: The Next Generation*. Cell, 2011. **144**(5): p. 646-674.
2. Vaupel, P., F. Kallinowski, and P. Okunieff, *Blood flow, oxygen and nutrient supply, and metabolic microenvironment of human tumors: a review*. Cancer Res, 1989. **49**(23): p. 6449-65.
3. Svastova, E., et al., *Hypoxia activates the capacity of tumor-associated carbonic anhydrase IX to acidify extracellular pH*. FEBS Lett, 2004. **577**(3): p. 439-45.
4. Kroemer, G. and J. Pouyssegur, *Tumor cell metabolism: cancer's Achilles' heel*. Cancer Cell, 2008. **13**(6): p. 472-82.
5. Kato, Y., et al., *Acidic extracellular microenvironment and cancer*. Cancer Cell Int, 2013. **13**(1): p. 89.
6. Tannock, I.F. and D. Rotin, *Acid pH in tumors and its potential for therapeutic exploitation*. Cancer Res, 1989. **49**(16): p. 4373-84.
7. Webb, B.A., et al., *Dysregulated pH: a perfect storm for cancer progression*. Nat Rev Cancer, 2011. **11**(9): p. 671-7.
8. Gerweck, L.E. and K. Seetharaman, *Cellular pH gradient in tumor versus normal tissue: potential exploitation for the treatment of cancer*. Cancer Res, 1996. **56**(6): p. 1194-8.
9. Swietach, P., R.D. Vaughan-Jones, and A.L. Harris, *Regulation of tumor pH and the role of carbonic anhydrase 9*. Cancer Metastasis Rev, 2007. **26**(2): p. 299-310.
10. Hashim, A.I., et al., *Imaging pH and metastasis*. NMR Biomed, 2011. **24**(6): p. 582-91.
11. Stubbs, M., et al., *Metabolic consequences of a reversed pH gradient in rat tumors*. Cancer Res, 1994. **54**(15): p. 4011-6.
12. Sonveaux, P., et al., *Targeting lactate-fueled respiration selectively kills hypoxic tumor cells in mice*. J Clin Invest, 2008. **118**(12): p. 3930-42.
13. Swietach, P., et al., *The chemistry, physiology and pathology of pH in cancer*. Philos Trans R Soc Lond B Biol Sci, 2014. **369**(1638): p. 20130099.
14. Semenza, G.L., *Hypoxia-inducible factors: mediators of cancer progression and targets for cancer therapy*. Trends Pharmacol Sci, 2012. **33**(4): p. 207-14.

15. McVicar, N., et al., *Quantitative tissue pH measurement during cerebral ischemia using amine and amide concentration-independent detection (AACID) with MRI*. J Cereb Blood Flow Metab, 2014. **34**(4): p. 690-8.
16. Gallagher, F.A., et al., *Magnetic resonance imaging of pH in vivo using hyperpolarized (13)C-labelled bicarbonate*. Nature, 2008. **453**(7197): p. 940-U73.
17. Grobben, B., P.P. De Deyn, and H. Slegers, *Rat C6 glioma as experimental model system for the study of glioblastoma growth and invasion*. Cell and Tissue Research, 2002. **310**(3): p. 257-270.
18. Zoula, S., et al., *Pimonidazole binding in C6 rat brain glioma: relation with lipid droplet detection*. Br J Cancer, 2003. **88**(9): p. 1439-44.
19. Ward, K.M. and R.S. Balaban, *Determination of pH using water protons and chemical exchange dependent saturation transfer (CEST)*. Magn Reson Med, 2000. **44**(5): p. 799-802.
20. Zhou, J., et al., *Practical data acquisition method for human brain tumor amide proton transfer (APT) imaging*. Magn Reson Med, 2008. **60**(4): p. 842-9.
21. Scholz, D.J., et al., *Quantified pH imaging with hyperpolarized (13) C-bicarbonate*. Magn Reson Med, 2015. **73**(6): p. 2274-82.
22. Martinez-Santesteban, F.M., et al., *T1 nuclear magnetic relaxation dispersion of hyperpolarized sodium and cesium hydrogencarbonate-13 C*. NMR Biomed, 2017.
23. Kim, M., et al., *Water saturation shift referencing (WASSR) for chemical exchange saturation transfer (CEST) experiments*. Magn Reson Med, 2009. **61**(6): p. 1441-50.
24. Lim, H., et al., *Construction and evaluation of a switch-tuned (13) C - (1) H birdcage radiofrequency coil for imaging the metabolism of hyperpolarized (13) C-enriched compounds*. J Magn Reson Imaging, 2014. **40**(5): p. 1082-90.
25. Schulte, R.F., et al., *Saturation-recovery metabolic-exchange rate imaging with hyperpolarized [1-13C] pyruvate using spectral-spatial excitation*. Magn Reson Med, 2013. **69**(5): p. 1209-16.
26. Beatty, P.J., D.G. Nishimura, and J.M. Pauly, *Rapid gridding reconstruction with a minimal oversampling ratio*. IEEE Trans Med Imaging, 2005. **24**(6): p. 799-808.
27. Stabenau, E.K. and T.A. Heming, *DETERMINATION OF THE CONSTANTS OF THE HENDERSON-HASSELBALCH EQUATION, (alpha)CO2 AND pKa, IN SEA TURTLE PLASMA*. The Journal of Experimental Biology, 1993. **180**(1): p. 311-314.

28. Yushkevich, P.A., et al., *User-guided 3D active contour segmentation of anatomical structures: significantly improved efficiency and reliability*. Neuroimage, 2006. **31**(3): p. 1116-28.
29. Gibson, E., et al., *Registration of prostate histology images to ex vivo MR images via strand-shaped fiducials*. J Magn Reson Imaging, 2012. **36**(6): p. 1402-12.
30. Engin, K., et al., *Extracellular pH distribution in human tumours*. Int J Hyperthermia, 1995. **11**(2): p. 211-6.
31. Stocchetti, N. and A.I. Maas, *Traumatic intracranial hypertension*. N Engl J Med, 2014. **370**(22): p. 2121-30.
32. Kaal, E.C. and C.J. Vecht, *The management of brain edema in brain tumors*. Curr Opin Oncol, 2004. **16**(6): p. 593-600.
33. Phan, L.M., S.C. Yeung, and M.H. Lee, *Cancer metabolic reprogramming: importance, main features, and potentials for precise targeted anti-cancer therapies*. Cancer Biol Med, 2014. **11**(1): p. 1-19.
34. Marusyk, A., V. Almendro, and K. Polyak, *Intra-tumour heterogeneity: a looking glass for cancer?* Nat Rev Cancer, 2012. **12**(5): p. 323-34.
35. Wike-Hooley, J.L., J. Haveman, and H.S. Reinhold, *The relevance of tumour pH to the treatment of malignant disease*. Radiother Oncol, 1984. **2**(4): p. 343-66.
36. Raza, S.M., et al., *Necrosis and glioblastoma: a friend or a foe? A review and a hypothesis*. Neurosurgery, 2002. **51**(1): p. 2-12; discussion 12-3.
37. Estrella, V., et al., *Acidity generated by the tumor microenvironment drives local invasion*. Cancer Res, 2013. **73**(5): p. 1524-35.
38. Strickland, M. and E.A. Stoll, *Metabolic Reprogramming in Glioma*. Front Cell Dev Biol, 2017. **5**: p. 43.

Chapter 5

5 Summary and Future work

This thesis investigated the molecular imaging of tumour metabolism using hyperpolarized ^{13}C magnetic resonance spectroscopic imaging (MRSI). Two important aspects of tumour metabolism were assessed: pyruvate conversion to lactate and the cellular pH gradient. The conversion of pyruvate to lactate is the final process of anaerobic glycolysis. As described by the Warburg effect, solid tumours often prefer energy production by glycolysis in the cytoplasm rather than more efficient oxidative phosphorylation within the Krebs cycle of mitochondria. [1, 2] Since tumour progression is correlated with lactate production, [3] the ability to measure this conversion can be used to quantify tumour progression and early therapeutic effects. The cellular pH gradient plays an important role in tumour proliferation and invasion. [4] Unlike healthy tissue, tumours often exhibit a reversed pH gradient such that extracellular pH (pH_e) is lower than the intracellular pH (pH_i). [5] Longitudinal measurements of changes in the pH gradient within tumours could also be useful to understand tumour progression.

These aspects of tumour metabolism can be measured using hyperpolarized ^{13}C magnetic spectroscopy imaging. $[1-^{13}\text{C}]\text{Pyruvate}$ can be used to non-invasively determine the lactate-to-pyruvate (Lac/Pyr) ratio in order to directly probe the conversion between pyruvate and lactate in tumours. ^{13}C bicarbonate can be used to directly measure pH_e by mapping the ratio of $\text{H}^{13}\text{CO}_3^-$ and $^{13}\text{CO}_2$ concentrations after its injection and application of the Henderson-Hasselbalch equation. Prior to injection into animals, $[1-^{13}\text{C}]\text{pyruvate}$ and ^{13}C bicarbonate were hyperpolarized, which can produce a greater than 10,000-fold signal increase for detection of metabolism with MRSI. [6] It is impractical to image these probes without hyperpolarization, due to their low sensitivity with MRI and limited concentration in tissue. In addition, specialized MRI pulse sequences are necessary to image these probes with a short acquisition time, which is dictated by the limited spin-relaxation time of hyperpolarized probes.

Furthermore, it was necessary to develop custom-made radiofrequency (RF) hardware for hyperpolarized ^{13}C MRSI. ^{13}C MRSI produces regional molecular information while ^1H

MRI provides valuable anatomical context. As a result, sensitive dual-frequency RF hardware was required to gather co-registered molecular and morphological imaging data with high sensitivity for signal detection. Thus a switch-tuned strategy for ^{13}C - ^1H RF hardware was designed and constructed. For optimum sensitivity and image homogeneity, a TORO mode was included to improve signal detection.

In this thesis, a rat model of glioma was used to study tumour metabolism. This rodent is an excellent model for preclinical imaging studies. It is relatively small and easy to handle but it is also large enough for imaging with a clinical MRI system without requiring higher-strength gradients to improve voxel size. Compared with mouse models, intravenous injections through the tail vein are considerably easier. Moreover, rats better tolerate the injected hyperpolarized imaging probes at larger volumes than smaller mice. In this study the brains of rats were stereotactically implanted with glioma. A longitudinal study was undertaken to assess the resulting tumour response to therapy. This tumour model recapitulates clinical progression and is an excellent system to study the assessment of therapeutic response using hyperpolarized endogenous probes. These animal experiments were performed in accordance with relevant guidelines and regulations stipulated by an animal use protocol approved by the University Council on Animal Care, Animal Use Subcommittee at Western University.

Glioma is a highly aggressive and proliferating brain tumour. [7] It is an ideal model to study tumour metabolism. As a highly proliferating tumour, glioma is very metabolically active, specifically through glycolysis. Brain tissue, although also metabolically active, prefers metabolism of pyruvate in the Krebs cycle, whereas in glioma pyruvate is converted predominantly to lactate. This difference was exploited to detect and quantify tumour response or progression after treatment. Increased glycolysis in the cytoplasm of glioma cells leads to greater intracellular hydrogen ion and acid production and increased ion transport to transfer these protons and metabolic acids to the extracellular space. This maintains an alkaline pH_i , at the expense of highly acidic pH_e . While the brain is well vascularized and perfused, this is not necessarily the case in the cores of brain tumours where necrosis is often present due to hypoxia. [8] The combination of an acidic

interstitial space and lack of perfusion gives tumour cells a proliferative advantage compared to other cells, which aids in proliferation.

Clinical treatment of glioma involves surgical resection of the tumour, if possible and radiotherapy followed by administration of chemotherapy to the patient. [9] In this study, stereotactic surgery was omitted which is extremely difficult to perform on rodents. Radiotherapy comprised of two fractions of 20 Gy, were administered to only the hemisphere of the brain containing the tumour with a modified μ CT system. For chemotherapy, 40 mg/kg of temozolomide (TMZ) was administered intraperitoneally for 5 days to mimic clinical practice. These therapies and their combination were chosen to duplicate the clinical setting as much as possible so that the some of the imaging methods and results learned through this longitudinal imaging study might eventually become clinically relevant.

5.1 Construction and evaluation of a switch-tuned ^{13}C – ^1H RF coil

Chapter 2 describes the construction a switch-tuned ^{13}C – ^1H birdcage RF coil system that is capable of metabolic imaging of hyperpolarized ^{13}C -enriched metabolic probes for co-registration with ^1H MRI morphology. In addition, the imaging performance of the RF coil was evaluated through comparison with identical single-tuned, ^1H and ^{13}C birdcage RF coils, which were constructed for that purpose. To further enhance RF receive sensitivity, a ^{13}C receive-only surface RF coil with active decoupling was also integrated with the switch-tuned ^{13}C – ^1H RF system to produce a transmit-only, receive-only RF system for ^{13}C operation. The performance of the individual RF coils and the TORO system were tested with specialized imaging phantoms at both ^1H and ^{13}C frequencies. A fast gradient-recalled echo (FGRE) sequence was used for proton imaging of phantoms and ^{13}C spectra were acquired using a FID-CSI sequence. B_1 homogeneity was also mapped using the Look-Locker method. The signal-to-noise ratio (SNR) achieved with the switch-tuned coil in transmit/receive mode was 87% that of the single-tuned ^1H coil. For ^{13}C imaging, the SNR for the switch-tuned ^{13}C coil was 55% that of the single-tuned coil. TORO operation of the switch-tuned coil with the surface coil increased SNR for by a factor of 4.2 over transmit/receive operation of the switch-tuned coil alone. As figure 2-

5 illustrates, the B_1 map is homogenous over the entire coil volume except near its ends. Finally the TORO RF and animal support systems were evaluated with animal imaging. This system provided co-registered imaging data for both nuclei with sufficient SNR for *in vivo* imaging experiments. Due to the additional circuit elements, the switch-tuned ^{13}C – ^1H RF coil had inferior SNR compared to that of individual frequency RF coils. However, the use of a surface coil with TORO operation greatly improved the observed SNR. *In vivo* metabolic imaging of injected $[1-^{13}\text{C}]$ pyruvate in a rat model of glioma was demonstrated using TORO operation. Two-dimensional ^{13}C spectral maps of pyruvate metabolism were measured, which were inherently co-registered with ^1H anatomical images.

5.2 Quantifying early therapeutic response using hyperpolarized $[1-^{13}\text{C}]$ pyruvate MRSI

Chapter 3 demonstrates the use of hyperpolarized ^{13}C MRSI to assess therapeutic efficacy in a preclinical tumour model. $[1-^{13}\text{C}]$ pyruvate was used to monitor early changes in tumour metabolism based on the Warburg Effect. High grade malignant tumours exhibit increased glycolytic activity and lactate production to promote proliferation. [10] A rat glioma model was used to explore altered lactate production after therapy as an early imaging biomarker for therapeutic response. Rats were surgically implanted with C6 glioma cells and separated into four groups: no therapy, radiotherapy, chemotherapy and combined therapy. Animals were imaged serially at 6 different time points (days 7, 12, 15, 18, 21, 24 after the surgery) using hyperpolarized $[1-^{13}\text{C}]$ pyruvate MRSI and conventional ^1H imaging. Using hyperpolarized $[1-^{13}\text{C}]$ pyruvate MRSI, alterations in tumour metabolism were detected as changes in the conversion of lactate to pyruvate (measured as the Lac/Pyr ratio) and compared to the conventional method of detecting therapeutic response using anatomical tumour volume measurement. In addition, the Lac/Pyr ratio was correlated with tumour growth rate. Hypoxia staining was performed at experimental endpoint and compared with the Lac/Pyr ratio map. Each therapy group expressed different characteristic changes in tumour metabolism. The group that received no therapy showed a gradual increase of the Lac/Pyr ratio within the tumour. The radiotherapy group showed large variations in tumour Lac/Pyr ratio. The chemo- and

combined therapy groups showed a statistically significant reduction in tumour Lac/Pyr ratio, however only the combined therapy was capable of suppressing tumour growth, which resulted in low endpoint mortality. A prompt reduction in the Lac/Pyr ratio was very apparent after therapy. However, measurements of tumour volume were not useful for establishment of therapeutic response until a much later time point. The Lac/Pyr ratio showed a significant correlation with tumour growth rate; however, it was not significantly correlated with tumour volume. Thus, Lac/Pyr ratio is potentially related to the growth of tumour rather than tumour volume. Regional differences in the Lac/Pyr ratio were consistent with hypoxia histology. Hyperpolarized magnetic resonance spectroscopic imaging of the metabolism of [1-¹³C]pyruvate was able to detect a reduction in the Lac/Pyr ratio as early as two days post combined chemo- and radiotherapies. In conclusion, metabolism of hyperpolarized [1-¹³C]pyruvate has been demonstrated as a non-invasive biomarker for assessment of therapeutic response.

5.3 Longitudinal Measurement of pH gradient

Chapter 4 reports the first longitudinal measurement of intracellular/extracellular pH gradient using non-invasive magnetic resonance imaging in a C6 rat glioma model. The acid-base balance in the brain is tightly controlled by endogenous buffers such as bicarbonate and phosphate. Tumours often express a positive pH gradient ($\text{pH}_i - \text{pH}_e$) in contrast to a negative gradient in normal tissue. [8] An alkaline pH_i in tumour cells increases the activity of several metabolic enzymes that drive cellular proliferation. [4] In contrast, an acidic pH_e is established due to increased lactic acid production and the subsequent active transport of protons out of the cell. [11] The pH_i was mapped with chemical exchange saturation transfer (CEST) and hyperpolarized ¹³C bicarbonate MRSI was used to determine regional pH_e . Rats were surgically implanted with C6 glioma cells in the brain. pH_i and pH_e were mapped in the tumour tissue and contralateral brain tissue at days 8, 12 and 15 post implantations. After sacrifice, rat brains were stained for histology including haematoxylin and eosin, HIF-1 α and Ki-67. Compared to contralateral brain tissue, the pH_e in tumours was more acidic, whereas the pH_i within tumour cells was more alkaline leading to an increase in the pH gradient compared to contralateral. Longitudinal measurements of the average pH gradient for all rats is shown

in Figure 4-4. Overall, the averaged pH gradient in the tumour changed from 0.02 ± 0.11 to 0.10 ± 0.21 then 0.19 ± 0.16 . Conversely the pH gradient of contralateral brain tissue changed from -0.44 ± 0.16 to -0.25 ± 0.21 then -0.33 ± 0.25 . The observed pH gradient was consistently larger in tumour than contralateral tissue. The pH gradient of tumours increased during tumour growth and also the heterogeneity of tumour pH was apparent at later time points. These regional measurements may be useful to assess therapeutic response and predict local areas of treatment resistance. Overall, the intracellular/extracellular pH gradients in this rat glioma model were non-invasively measured to a precision of ~ 0.1 pH units at three time points. Since most therapeutic agents are weak acids or bases, *a priori* knowledge of the pH gradient may help guide choice of therapeutic agent.

5.4 Future work

A TORO RF system was developed to provide a sensitive detection system for ^{13}C MRSI. RF sensitivity could be extended over a larger volume than that provided by the single surface receive coil by development of an RF receive array. Although an individual surface RF coil has high sensitivity, this is only the case over a limited region. In theory, the SNR of a coil array is increased by \sqrt{N} where N is the number of surface coils. Furthermore, imaging can be accelerated using parallel imaging techniques. If there is a sufficient coverage of the imaging volume by the array coil, spatial information of the signal can be deduced by the weighting of signals from multiple surface coils. The drawback of a coil array is that design and construction of the array coil is far more complicated than for a single surface coil. Moreover, multiple receive channels are required. Currently the multi-nuclear receive hardware at the GE Discovery MR750 3.0 T is limited to eight channels. Receive arrays are typically operated in TORO mode with a volume transmit coil.

In chapter 3, rat glioma was imaged for up to 24 days after tumour implantation. For radiotherapy and combined therapy, survival outcomes of these groups were inconclusive. Tumour volume was not significantly altered by therapy. Since glioma is known to recur despite therapy [12], it is possible that a subsequent increase in the

Lac/Pyr ratio might be observed in a treated tumour in a longer longitudinal study. This would be an important finding, demonstrating a potential prognostic capability of this imaging method. Other hyperpolarized ^{13}C probes can be used to quantify more aspects of tumour metabolism. For instance, $[1, 4\text{-}^{13}\text{C}_2]\text{fumarate}$ can be used to detect apoptosis. Increased $[1,4\text{-}^{13}\text{C}_2]\text{malate}$ production from $[1,4\text{-}^{13}\text{C}_2]\text{fumarate}$ has been observed in treated lymphoma cells after injection of hyperpolarized fumarate. This is likely a result of cellular necrosis suggesting that formation of malate from fumarate may be an *in vivo* biomarker for tumour cell death and response of tumours to treatment. [13] However, it may be difficult to determine if and when an optimum time exists for *in vivo* imaging of this process due to the nature of apoptosis.

In chapter 4, MRI techniques were used to quantify the cellular pH gradient in tumours. Using these combined methods, a reversal of the pH gradient was observed in tumours compared to healthy brain tissue. Some chemotherapy drugs are effective only within a limited pH range. It would be informative to know in advance, how different therapies might be affected by the tumour microenvironment including intracellular and extracellular pH.

At this juncture, almost all hyperpolarized ^{13}C imaging research has been demonstrated using cell cultures or animal models. [14, 15] [14, 15] [14, 15] [14, 15] [14, 15] [14, 15] [14, 15] [14, 15] [14, 15] [14, 15] [14, 15] As basic research continues to develop the foundation for eventual clinical translation, manufacturers have developed hyperpolarization apparatus compatible with human use. A small number of these systems are currently being used for first-in-kind experiments and early clinical trials. [14, 15] The use of ^{13}C -enriched endogenous substrates does not pose any significant toxicity or radiation exposure. No dose-related problems are expected for human imaging. With the advent of next-generation polarization technology, successful adoption in the clinic will require pre-clinical research such as that presented in this thesis. This will provide important information such as data to guide human dose, well-characterized biomarkers for non-invasive detection and assessment of disease and a proven ability to guide therapy.

References for Chapter 5

1. Brahim-Horn, M.C., J. Chiche, and J. Pouyssegur, *Hypoxia signalling controls metabolic demand*. *Curr Opin Cell Biol*, 2007. **19**(2): p. 223-9.
2. Gatenby, R.A. and R.J. Gillies, *Why do cancers have high aerobic glycolysis?* *Nature Reviews Cancer*, 2004. **4**(11): p. 891-899.
3. Romero-Garcia, S., et al., *Lactate Contribution to the Tumor Microenvironment: Mechanisms, Effects on Immune Cells and Therapeutic Relevance*. *Front Immunol*, 2016. **7**: p. 52.
4. Webb, B.A., et al., *Dysregulated pH: a perfect storm for cancer progression*. *Nat Rev Cancer*, 2011. **11**(9): p. 671-7.
5. Gerweck, L.E. and K. Seetharaman, *Cellular pH gradient in tumor versus normal tissue: potential exploitation for the treatment of cancer*. *Cancer Res*, 1996. **56**(6): p. 1194-8.
6. Ardenkjaer-Larsen, J.H., et al., *Increase in signal-to-noise ratio of > 10,000 times in liquid-state NMR*. *Proc Natl Acad Sci U S A*, 2003. **100**(18): p. 10158-63.
7. Omuro, A. and L.M. DeAngelis, *Glioblastoma and other malignant gliomas: a clinical review*. *JAMA*, 2013. **310**(17): p. 1842-50.
8. Graif, M., et al., *Contrast-enhanced MR imaging of malignant brain tumors*. *AJNR Am J Neuroradiol*, 1985. **6**(6): p. 855-62.
9. Mason, W.P., et al., *Canadian recommendations for the treatment of glioblastoma multiforme*. *Curr Oncol*, 2007. **14**(3): p. 110-7.
10. Strickland, M. and E.A. Stoll, *Metabolic Reprogramming in Glioma*. *Front Cell Dev Biol*, 2017. **5**: p. 43.
11. Swietach, P., et al., *The chemistry, physiology and pathology of pH in cancer*. *Philos Trans R Soc Lond B Biol Sci*, 2014. **369**(1638): p. 20130099.
12. Davis, M.E., *Glioblastoma: Overview of Disease and Treatment*. *Clin J Oncol Nurs*, 2016. **20**(5): p. S2-8.
13. Gallagher, F.A., et al., *Production of hyperpolarized [1,4-C-13(2)]malate from [1,4-C-13(2)]fumarate is a marker of cell necrosis and treatment response in tumors*. *Proceedings of the National Academy of Sciences of the United States of America*, 2009. **106**(47): p. 19801-19806.
14. Kurhanewicz, J., et al., *Analysis of cancer metabolism by imaging hyperpolarized nuclei: prospects for translation to clinical research*. *Neoplasia*, 2011. **13**(2): p. 81-97.

15. Kurhanewicz, J., et al., *Current and potential applications of clinical ^{13}C MR spectroscopy*. *Journal of Nuclear Medicine*, 2008. **49**(3): p. 341-4.

Appendices A- 1: Permission for reproduction of Scientific articles

JOHN WILEY AND SONS LICENSE TERMS AND CONDITIONS

Aug 28, 2017

This Agreement between The University of Western Ontario -- Timothy Scholl ("You") and John Wiley and Sons ("John Wiley and Sons") consists of your license details and the terms and conditions provided by John Wiley and Sons and Copyright Clearance Center.

License Number	4167790511177
License date	Aug 14, 2017
Licensed Content Publisher	John Wiley and Sons
Licensed Content Publication	Journal of Magnetic Resonance Imaging
Licensed Content Title	Construction and evaluation of a switch-tuned ^{13}C - ^1H birdcage radiofrequency coil for imaging the metabolism of hyperpolarized ^{13}C -enriched compounds
Licensed Content Author	Heeseung Lim,Kundan Thind,Francisco M. Martinez-Santiesteban,Timothy James Scholl
Licensed Content Date	Jan 17, 2014
Licensed Content Pages	9
Type of use	Dissertation/Thesis

Requestor type	Author of this Wiley article
Format	Print and electronic
Portion	Full article
Will you be translating?	No
Title of your thesis / dissertation	Study of C6 Rat Glioma Using Hyperpolarized ¹³ C Magnetic Resonance Spectroscopic Imaging
Expected completion date	Aug 2017
Requestor Location	The University of Western Ontario University of Western Ontario Robarts Research Institute London, ON N6A5B7 Canada Attn: T. Scholl
Publisher Tax ID	EU826007151
Billing Type	Invoice
Billing Address	The University of Western Ontario University of Western Ontario Robarts Research Institute London, ON N6A5B7 Canada Attn: T. Scholl
Total	0.00 USD

Appendices A- 2: Animal use protocol

PI : Scholl, Timothy

Protocol # 2014-040

Status : Approved (w/o Stipulation)

Approved : 01/23/2015

Expires : 01/01/2019

Title : Development of Hyperpolarized Metabolic Probes for Magnetic Resonance Imaging of Disease in Animal Models

Animal Use Protocol Overview

Animal Use Protocol Title

Development of Hyperpolarized Metabolic Probes for Magnetic Resonance Imaging of Disease in Animal Models

Application Type. If this is a post-pilot project, please attach the Pilot Report to this section, below.

Post-Pilot Full Protocol

Provide Associated Previous Protocol Number

2010-273

Please provide a report detailing the previous AUP's use of Animals

Post Pilot Update.

The pilot AUP (2010-273) helped establish our hyperpolarized metabolic probes research and answer some important associated questions. Within the four years of the pilot protocol:

- 1) We were able to develop novel dual-frequency RF hardware and compatible animal support hardware for hyperpolarized magnetic resonance imaging using healthy animals. This early research established that the RF hardware had sufficient sensitivity for *in vivo* experiments. It also established our ability to hyperpolarize endogenous compounds for injection as contrast agents and safely inject them into the tail veins of rats and rapidly image metabolism. We were also able to gauge imaging signal-to-noise ratio which determines the spatial resolution of our metabolic imaging experiments. Our imaging hardware is being used for all hyperpolarized preclinical imaging experiments at Robarts.
- 2) From early experiments we were able to determine the change in lactate conversion from pyruvate in response to radio- and chemotherapies. This information allows us to calculate accurate cohort numbers for our longitudinal studies.
- 3) We have observed significant changes in tumour hypoxia using metabolic imaging of hyperpolarized pyruvate as early as two days post therapy. This provides a much earlier assessment than changes in tumour volume measured from MRI or CT.

4) Early experiments using hyperpolarized ^{13}C bicarbonate have demonstrated our ability to measure pH in solid tumours. These experiments have provided useful data for 7 research articles, the renewal of a research grant from the Ontario Institute for Cancer Research, two research grants from Cancer Care Ontario and a funding application to the Canadian Institutes for Health Research, which is still pending.

The 3Rs

Reduction: Our preliminary research has allowed us to refine our surgical techniques and animal care to reduce animal mortality. We also have established animal numbers to power our statistical comparisons between animal cohorts. Our experiments require cohort numbers of approximately eight animals per treatment group to establish significance between groups. We are requesting an additional four animals based on our experiences to date to replace those animals that do not survive to the experimental endpoint (if necessary).

Replacement: We are studying the response of solid tumours to realistic clinical treatment as a first step to eventual clinical translation and as such, we require a realistic tumour model. The C6 rat glioblastoma is an excellent experimental model for our research. The tumours are precisely located through stereotactic intracranial implantation and grow with relative speed and predictability from animal to animal. These tumours have good contrast compared with healthy brain tissue with magnetic resonance imaging. Their location within the skull provides improved tumour location and reduced image artefact from animal motion.

Refinement: We are constantly improving our experimental apparatus and imaging methods with an aim to improved imaging results. This will decrease the number of animals required for our studies. We are also developing new formulations for hyperpolarized probes, which will produce improved imaging results with decreased injected dose.

Using non-scientific language, please describe the project's purpose, expected benefit, and a brief summary of your work with the animal model(s).

Please be aware that in the event of communications with Western Media Relations and the PI is not available, this summary will be sent to Western Media Relations.

Molecular imaging is a rapidly developing field, which non-invasively visualizes cellular function such as metabolism. Our research has focused on development of novel molecular imaging probes for magnetic resonance imaging (MRI) with a specific emphasis on application to cancer imaging. Therapeutic choice for an individual cancer patient relies on invasive tumour sampling. For many targeted agents, molecular assessment is particularly important to both apply these agents to cancers that are most likely to respond and avoid treatments that are unlikely to be effective. Sadly, predictive biomarkers are not perfect prognosticators of therapeutic response or failure for a given agent in a particular patient and treatment assessment often relies on longitudinal measurements of changes in tumour size. Significant changes in tumour size can take months to become apparent if at all. Molecular imaging has the potential to non-

invasively assess subtle changes in disease. For cancer, it can assess the evolution of the tumour microenvironment, determine the potential for tumour proliferation and, perhaps most importantly, provide prompt evidence for early responses versus non-responses during ongoing treatment.

Since MRI is a valuable diagnostic imaging tool capable of morphological and functional imaging with high spatial resolution and is the standard of care for assessment of most solid tumours, the added capability to assess molecular function is an important development, particularly for cancer research. For example, our preclinical research is demonstrating the ability to measure metabolic changes in the tumour such as hypoxia as soon as one day after initiation of therapy. This research using hyperpolarized metabolic imaging of hyperpolarized ^{13}C -enriched compounds has produced seven peer-reviewed research articles and 17 conference abstracts over the past four years. In addition, a recent oral presentation of one of my PhD student's thesis entitled "Molecular imaging of tumor metabolism: a longitudinal study of tumour response to therapies using hyperpolarized ^{13}C pyruvate" received a Magna Cum Laude Merit Award (top 5%) at the 2014 Scientific Meeting of the International Society for Magnetic Resonance in Medicine in Milan, Italy.

The next steps for our hyperpolarized imaging research is to investigate additional probes of the tumour microenvironment. Our initial experiments have focused on pyruvate metabolism and its role in assessing hypoxia. We are currently interesting in assessing changes in pH, which tumours exploit for proliferative advantage. Using hyperpolarized ^{13}C bicarbonate, we plan to non-invasively measure extracellular pH and compare that with the intracellular pH assessed through chemical exchange saturation transfer (CEST) magnetic resonance imaging in tumour cells. Cellular necrosis in response to therapy can also be measured through conversion of hyperpolarized fumarate to malate as cellular walls break down. These three important biomarkers of the tumour microenvironment (hypoxia, pH and cellular necrosis) will be studied simultaneously in a rat model of glioma to look at their prognostic potential for early assessment of treatment response and longer term treatment outcome in extended longitudinal studies.

We are working with John Ronald to modify our brain cancer cell line for *in vivo* animal experiments. We have engineered these cells so that they produce a fluorescent green protein which makes the viable tumour cells much more visible under histology. In addition, the cells produce an enzyme known as luciferase, which can be used for bioluminescence imaging (BLI). Our animals are injected with a small amount of a compound known as luciferin. The luciferase produced by living tumour cells cause a chemical reaction with the luciferin that produces light. The amount of light that we measure with BLI is proportional to the number of living tumour cells. This allows us to non-invasively measure tumour burden in longitudinal studies of therapy. This is our gold-standard against which we can compare our other methods such as metabolic imaging of pyruvate, measurements of pH and cellular necrosis.

GLOSSARY OF TERMS - Identify each individual scientific term and abbreviation using CAPITAL LETTERS, and then briefly define each term to be referenced in any section of this protocol.

e.g. ALLELE - The genetic variant of a gene responsible for the different traits of certain characteristics and genetic diseases.

MRI - Magnetic Resonance Imaging.

¹³C - A naturally occurring non-radioactive isotope of carbon (1.11% natural abundance).

HYPERPOLARIZATION - A technique for enhancing MRI signal strength by factors of up to 100,000.

PYRUVATE - An endogenous intermediate in carbohydrate metabolism.

BICARBONATE - An endogenous compound used to measure *in vivo* pH with hyperpolarized imaging.

CEST - Chemical exchange saturation transfer. This a magnetic resonance imaging technique that is used to measure intracellular pH. This is a non-invasive imaging method that does not require injection of a contrast agent.

GLIOBLASTOMA or GLIOMA - A glioma is a type of tumor that starts in the brain or spine, more specifically the definition of glioma is a primary brain tumor that originates from the supportive cells of the brain, called glial cells. Glial cells are the most common cellular component of the brain There are five to ten times more glial cells than neurons. A Glioblastoma is a particular type of Glioma (Astrocytoma).

FUMARATE - An endogenous intermediate in the citric acid cycle (krebs cycle).

MOLECULAR IMAGING - a non-invasive means to visualize cellular function such as metabolism.

BLI - Bioluminescence imaging is a means of measuring the biodistribution of cells that have been engineered to produce light after injection of a contrast agent.

Luciferin -is a light-emitting compound which is injected into animals to generate bioluminescence. Cells in these animals, which produce the enzyme luciferase cause a chemical reaction with luciferin producing light that can be imaged by BLI.

Here is the link to CCAC's Policy on Scientific Merit and Ethical Review of Animal-based Research:

http://www.ccac.ca/Documents/Standards/Policies/Scientific_merit_and_ethical_review_of_animal-based_research.pdf

(http://www.ccac.ca/Documents/Standards/Policies/Scientific_merit_and_ethical_review_of_animalbased_research.pdf)

Has the work outlined in this AUP received favourable scientific peer review?

Yes

Do you wish to provide a funding peer review assessment, which may be considered in lieu of internal scientific peer review? If 'YES', please attach the funding assessment.

No

If this is a RESEARCH AUP, please provide a list of one to three publications relevant to the work outlined in this AUP.

If this is a research AUP, attach an OUTLINE for scientific merit reviewers that provides sufficient information that another scientist working in the same field of study could effectively review this AUP's scientific merit, below. PIs may utilize

whichever format best describes its scientific merit, e.g. background, rationale, hypothesis, objectives, experimental procedures

Using only key words, specify the animal models and procedures described within this AUP.

Research/ Anaesthesia/ Imaging/ Stereotaxic Surgery/ Tumour Cell Injections/ Analgesia/ Chemotherapy/ Injection IP/ Radiotherapy/ Euthanasia

Curriculum Vitae

Education

- Ph.D. Medical Biophysics, **2010 Sept ~ Present**, University of Western Ontario, London, ON. Concentration: Hyperpolarized ^{13}C metabolic imaging
- B.Sc. Specialist in Biophysics, **2006 Sept ~ 2010 Apr**, University of Toronto, Toronto, ON.

Publications (1st Author)

1. Heeseung Lim, Thind K, Alejski A, Martínez F, Scholl TJ, *Construction and Evaluation of a Switch-Tuned ^{13}C - ^1H Birdcage Radiofrequency Coil for Imaging the Metabolism of Hyperpolarized ^{13}C -Enriched Compounds*. Journal of Magnetic Resonance Imaging, 2014. **40**(5): p. 1082-1090.
2. Heeseung Lim, Martinez-Santiesteban F, Jensen M, Chen A, Wong E, Scholl TJ, *Monitoring changes in tumour metabolism in response to therapy using hyperpolarized ^{13}C MRSI in a preclinical model of glioma*. Scientific Reports (in revision).
3. Heeseung Lim, Albatany M, Bartha R, Scholl TJ. “*Longitudinal Monitoring of Tumour pH Gradient with MRI*” NMR in Biomedicine (in preparation).

Publications (Other)

1. Martinez-Santiesteban FM, Dang TP, Heeseung Lim, Chen AP, Scholl TJ, *T_1 Nuclear Magnetic Relaxation Dispersion of the Sodium and Cesium Salts of Hyperpolarized ^{13}C -Bicarbonate*. NMR in Biomedicine (accepted).
2. Thind K, Jensen MD, Hegarty E, Chen AP, Heeseung Lim, Martínez F, Van Dyk J, Wong E, Scholl TJ, Santyr GE, *Mapping metabolic changes associated with early Radiation Induced Lung Injury post conformal radiotherapy using hyperpolarized ^{13}C -pyruvate Magnetic Resonance Spectroscopic Imaging*. Radiotherapy and Oncology, 2014. **110**(2): p. 317-322.
3. Mallett CL, Heeseung Lim, Thind K, Chen Y, Ribot EJ, Martínez F, Scholl TJ, Foster PJ, *Longitudinal anatomical and metabolic MRI characterization of orthotopic xenograft prostate tumors in nude mice*. Journal of Magnetic Resonance Imaging, 2014. **40**(4): p. 848-856.

Presentations

- Heeseung Lim, Mohammed Albatany, Francisco M. Martínez, Robert Bartha and Timothy J. Scholl. (2017). “*Longitudinal Monitoring of Tumour pH Gradient with MRI*” 17th Annual Imaging Network Ontario Symposium London. Canada
- Heeseung Lim, Mohammed Albatany, Francisco M. Martinez-Santiesteban, Robert Bartha and Timothy J. Scholl. (2015) “*Magnetic Resonance Imaging of the Intracellular/Extracellular pH Gradient in Glioma*” 2015 World Molecular Imaging Congress Honolulu. USA

- Heeseung Lim, Kundan Thind, Timothy Pok Chi Yeung, Francisco M. Martinez-Santibesteban, Eugene Wong, Paula J Foster and Timothy J. Scholl. (2014). “*Studying tumour metabolism; using hyperpolarized ^{13}C pyruvate magnetic resonance imaging.*” 2nd Biennial Cancer Research Conference Windsor, Canada
- Heeseung Lim, Kundan Thind, Timothy Pok Chi Yeung, Francisco M. Martinez-Santibesteban, Eugene Wong, Paula J Foster and Timothy J. Scholl. (2014). “*Imaging of tumor metabolism: a longitudinal study of tumor response to therapies using hyperpolarized $[1-^{13}\text{C}]$ pyruvate.*” Talk presented at ISMRM 22st Annual Meeting & Exhibition Milano. Italy

Posters

- Heeseung Lim, Mohammed Albatany, Francisco M. Martínez, Robert Bartha and Timothy J. Scholl. (2017). “*Longitudinal pH Gradient in Tumour with MRI*” Poster presented at London Health Research Day 2017 London. Canada
- Heeseung Lim, Mohammed Albatany, Francisco M. Martínez, Robert Bartha and Timothy J. Scholl. (2016). “*MEASURING INTRA- and EXTRACELLULAR pH in TUMOURS USING MRI*” Poster presented at 16th Annual Imaging Network Ontario Symposium Toronto. Canada
- Heeseung Lim, Nevin McVicar, Francisco M Martinez-Santiesteban, Robert Bartha and Timothy J Scholl. (2014). “*Non-invasive measurement of cellular membrane pH gradient in brain tumors using hyperpolarized ^{13}C -bicarbonate MSRI and CEST imaging*” Poster presented at ISMRM 22st Annual Meeting & Exhibition Milano. Italy
- Heeseung Lim, Kundan Thind, Timothy Pok Chi Yeung, Francisco M. Martinez-Santibesteban, Eugene Wong, Paula Foster and Timothy J. Scholl. (2014). “*Molecular imaging of tumor metabolism: a longitudinal study of tumor response to therapies using hyperpolarized $[1-^{13}\text{C}]$ pyruvate*” Poster presented at 14th Annual Imaging Network Ontario Symposium Toronto. Canada
- Heeseung Lim, Kundan Thind, Timothy Pok Chi Yeung, Francisco M. Martinez-Santibesteban, Eugene Wong, Paula Foster and Timothy J. Scholl. (2013). “*Monitoring Therapeutic Response in a Rat Model of Glioma with Hyperpolarized $[1-^{13}\text{C}]$ Pyruvate*” Poster presented at 4th International DNP Symposium Copenhagen. Denmark
- Heeseung Lim, Kundan Thind, Francisco Martínez and Timothy J. Scholl. (2013) “*Transmit-only receive-only operation of a switch-tuned ^{13}C - ^1H radiofrequency coil for improved in vivo ^{13}C spectroscopy*” Electric Poster presented at ISMRM 21st Annual Meeting & Exhibition Salt Lake City. USA
- Heeseung Lim, Kundan Thind, Timothy Yeung, Francisco Martinez and Timothy J. Scholl. (2013). “*Detecting and characterizing therapeutic response to radio- & chemotherapies with hyperpolarized $[1-^{13}\text{C}]$ pyruvate in rat glioma model*” Electric Poster presented at ISMRM 21st Annual Meeting & Exhibition Salt Lake City. USA

- Heeseung Lim, Kundan Thind, Timothy Yeung, Francisco Martinez and Timothy J. Scholl. (2013). “*Monitoring Therapeutic Response in a Rat Model of Glioblastoma Multiforme with hyperpolarized [1-¹³C]Pyruvate.*” Poster presented at 13th Annual Imaging Network Ontario Symposium Toronto. Canada
- Heeseung Lim, Kundan Thind, Francisco Martínez and Timothy J. Scholl. (2012). “*Transmit-only receive-only operation of a switch-tuned ¹³C - ¹H radiofrequency coil with a ¹³C surface receive-only coil for enhanced in vivo ¹³C spectroscopy*” Poster presented at The Third International Workshop on Hyperpolarized Carbon-13 and Its Application in Metabolic Imaging Philadelphia. USA
- Heeseung Lim, Kundan Thind, Jian-xiong wang, Andrew Alejski, Francisco Martinez and Timothy J. Scholl. (2012). “*Switch-tunable ¹³C & ¹H frequency RF coil for Hyperpolarized ¹³C imaging of Rodents*” Electric Poster presented at ISMRM 20th Annual Meeting & Exhibition Melbourne. Australia
- Heeseung Lim, Francisco Martínez and Timothy J. Scholl. (2012). “*Dual-Frequency RF Solenoid Coil for Combined ¹³C and ¹H Imaging.*” Poster presented at 12th Annual Imaging Network Ontario Symposium Toronto. Canada

Awards and Scholarships

- IMNO presentation award: Honourable Mention **2017**
15th Imaging Network Ontario Symposium
Description: Top 5 of presentations in the field
- ISMRM Merit award: Magna Cum Laude **2014**
International Society for Magnetic Resonance in Medicine
Description: Top 15% of abstracts in the field
- Molecular Imaging Travel Award (\$700) **2014**
Molecular imaging journal club, University of Western Ontario, London, Canada
Description: Students who presents molecular imaging work at international conferences.
- Molecular Imaging Travel Award (\$700) **2013**
Molecular imaging journal club, University of Western Ontario, London, Canada
Description: Students who presents molecular imaging work at international conferences.
- Molecular Imaging Travel Award (\$700) **2012**
Molecular imaging journal club, University of Western Ontario, London, Canada
Description: Students who presents molecular imaging work at international conferences.
- Schulich Graduate Scholarship (\$6700) **2010** University of Western Ontario, London, Canada
Description: Domestic students with average 80% or greater, Internal multi-year scholarship that covers tuition and ancillary fees
- Recognition of Excellent in CHM326 **2009** University of Toronto, Toronto, Canada
Description: In recognition of attaining an excellent mark in CHM326 course.
- Certificate of Appreciation **2010** University Health Network, Toronto, Canada
Description: In recognition of outstanding contribution to the Toronto General

Hospital community, patients, staff and families.

- University of Toronto In Course Scholarship (\$1000) **2009** University of Toronto, Toronto, Canada Description: Outstanding students who excel in their university academic work .
- Queen Elizabeth II aiming for the top Scholarship (\$3500) **2006** OSAP Canada Description: Ontario students who have shown academic excellence at the high school level.

Teaching experience

- Teaching Assistant **2006 Sept ~ 2010 July** Toronto Korean Methodist Church Korean Language School, North York, ON Duties: assignment and exam development, evaluation and grading student performance, meeting during office hours for tutoring.

Other experience

- Senior Volunteer **2008 Oct ~ 2010 Aug** Toronto General Hospital, Toronto, ON Responsibility: patient care, administration, info desk, organize mailing list.